

# Magnetic Resonance Imaging Guidance for Histotripsy Therapy

By

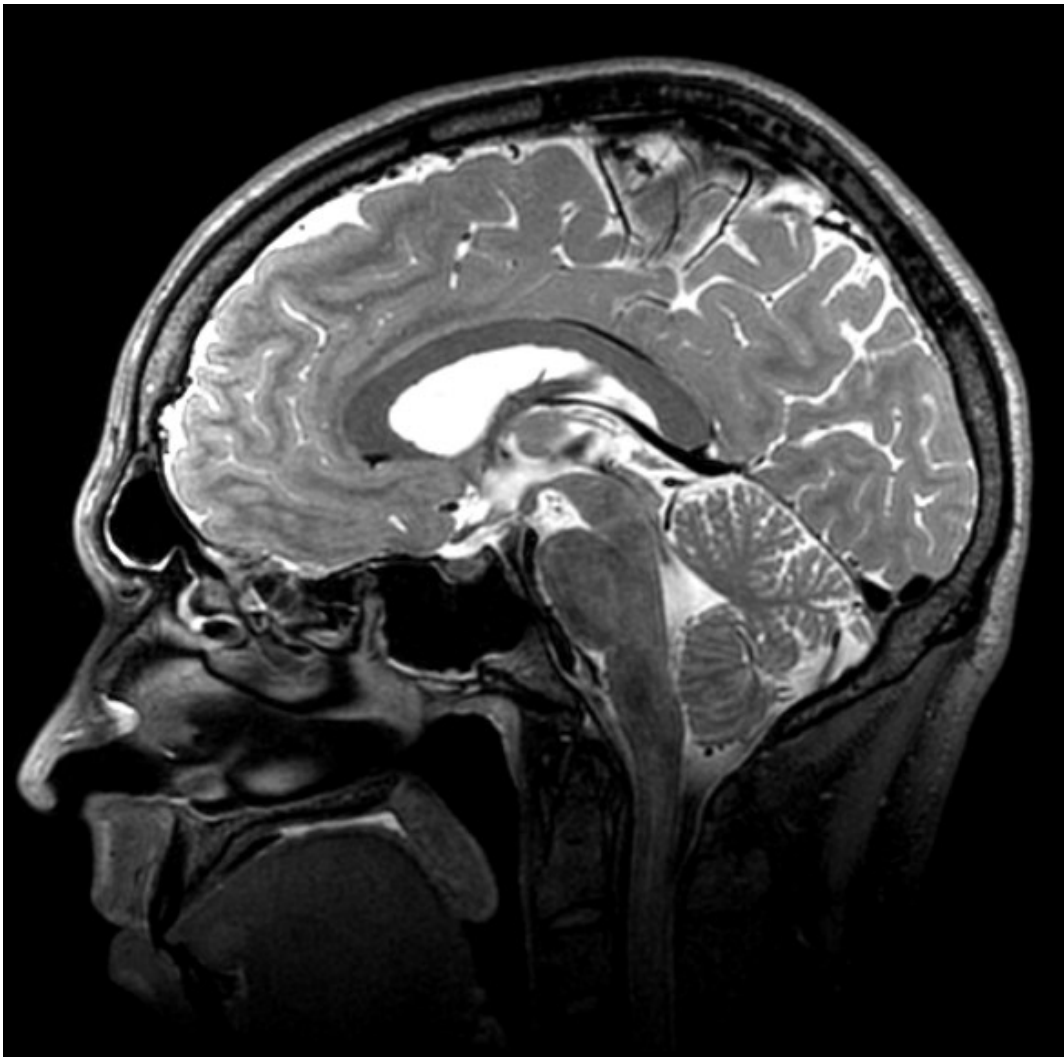
Steven P. Allen

A dissertation submitted in partial fulfillment  
of the requirements for the degree of  
Doctor of Philosophy  
(Biomedical Engineering)  
in the University of Michigan  
2016

Doctoral Committee:

Associate Research Scientist Timothy L. Hall, Co-Chair  
Professor Charles A. Cain, Co-chair  
Research Associate Professor Luis Hernandez-Garcia  
Research Assistant Professor Scott D. Swanson

A Portrait of the Author as a Middle-Aged Man



© Steven P. Allen 2016

# Dedication

To My Family

## Acknowledgements

I would first like to thank my advisor, Dr. Tim Hall. He has been a source of excellent research advice, support as I have juggled several responsibilities, and a great sounding board for new ideas. Dr. Hall has also taught me careful experiment design and the value of clean data. He has given excellent writing advice and has been very supportive as I have pursued teaching opportunities. Lastly, during my time at Michigan, my family has tripled in size. Dr. Hall has been extremely supportive through these changes, for which I am profoundly grateful.

I hold a great deal of gratitude toward my dissertation committee: Drs. Luis Hernandez-Garcia, Charles Cain, and Scott Swanson. Dr. Hernandez-Garcia has been extremely helpful with research ideas and has been a tremendous resource to me as I learned how to operate a MRI scanner and understand MRI concepts. He has also been a great example to me of mentorship, collaboration, and collegiality.

Dr. Charles Cain has had many inventive and useful ideas that have pushed me to think more deeply and creatively about the mechanisms and methods presented in this dissertation. I am grateful for his enthusiasm and the time he has taken to counsel me about my research. Additionally, Dr. Scott Swanson has been an excellent resource to help me understand the physical mechanisms behind NMR relaxation. He has helped me overcome several hurdles in measuring MR relaxation parameters.

I owe thanks to many other members of our research group: Dr. Zhen Xu for her career and life advice, which was perfectly timed and always correct; Dr. Joan Greve, for her support and enthusiasm which exceeded beyond expectation; Dr. Will Roberts who allowed me to conduct my first experiments on his animals; Dr. Kim Ives, without whom, to put it frankly, I could not have done very much effective work.

I would like to thank Maria Steele who has been very helpful getting all the underlying academic and administrative business taken care while Kathleen McCrumb has

been extremely helpful in navigating the university's complex purchasing procedures. I would also like to extend a big thank you to the entire BME staff in the Gerstacker building, who would, if I brought my baby daughter by, boisterously coo and fawn over her. It made me feel like a million dollars.

I would like to thank the students, post-docs, and former students of the histotripsy lab. Alex Duryea taught me how to design and build transducers. Yohan Kim taught me about electronics. Adam Maxwell and Eli Vlasisavljevich were excellent consultants on both experimental design and acoustic physics. Kuang-Wei Lin helped me a great deal when I was getting started. Hedieh Tammadoni's discussion on philosophy and life were extremely invigorating and, she, at least once, gave me a ride to pick my daughter up from day care after I had locked my keys in my car. I would like to thank Ryan Miller, Tzu-Yin Wang, Simone Park, Xi Zhang, Jonathan Sukovich, Jonathan Lundt, Jonathon Macoskey, Yige Li, and Tyler Gerhardson. They have been excellent collaborators and friends. I should also mention the members of Doug Noll's lab, who permitted me to use their equipment without reservation and have been helpful in all their discussions. I would also like to thank the undergraduates and graduate students with whom I had the pleasure of teaching as a graduate student instructor and substitute lecturer.

Lastly, I would like to my wife, Christie, and my daughter, Evelyn, who I both found during my time at Michigan. They have been wonderful sources of strength to me.

*Ann Arbor, Michigan*

*April 2016*

# Table of Contents

Dedication .....	ii
Acknowledgements .....	iii
List of Figures .....	x
List of Tables .....	xvii
List of Equations .....	xviii
List of Appendices .....	xix
Abstract.....	xx
Chapter 1: Introduction.....	1
1.1    Histotripsy .....	1
1.2    MRI Signal Phase.....	2
1.2.1    T2 Relaxation.....	3
1.2.2    The Bipolar Gradient.....	4
1.3    Outline of Chapters.....	5
1.4    References.....	6
Chapter 2: Sensitizing MR Imaging to Water Motion Caused by the Bubble Cloud.....	9
2.1    Introduction .....	9
2.2    Histotripsy .....	10
2.3    Flow at Cavitation .....	10
2.4    IVIM Imaging .....	10
2.5    Histotripsy and IVIM Imaging.....	12
2.6    Methods .....	13

2.6.1	Cavitation Generation .....	14
2.6.2	MR Images .....	15
2.6.3	Experiment A: Dependence on Ultrasound Pulse Amplitude .....	16
2.6.4	Experiment B: Dependence on the IVIM Gradient Waveform .....	17
2.6.5	Experiment C: Directional Dependence.....	17
2.6.6	Experiment D: Dependence on Timing .....	18
2.6.7	Experiment E: <i>Ex Vivo</i> Tissue Sample.....	18
2.6.8	Control Images .....	19
2.6.9	Data processing .....	19
2.7	Results .....	19
2.7.1	A: Dependence on Ultrasound Pulse Amplitude .....	20
2.7.2	B: Dependence on the IVIM Waveform .....	21
2.7.3	C: Dependence on Direction.....	21
2.7.4	D: Dependence on Cavitation and IVIM Gradient Timing .....	22
2.7.5	E: <i>Ex Vivo</i> Tissue Sample.....	23
2.8	Discussion.....	24
2.8.1	Cavitation.....	24
2.8.2	Effect of Susceptibility Gradients.....	24
2.8.3	The Effects of Fluid Motion .....	25
2.8.4	Therapy Feedback in Tissue .....	26
2.9	Conclusion.....	27
2.10	References.....	27
Chapter 3: MR Imaging of Individual Histotripsy Bubble Clouds .....		31
3.1	Introduction .....	31
3.2	Methods .....	33
3.2.1	Transducer.....	33



3.2.2	MRI Sequence.....	34
3.2.3	Experiment A: Determining the Cavitation Threshold.....	37
3.2.4	Experiment B: Tissue Treatment.....	38
3.3	Results .....	39
3.3.1	Experiment A: Cavitation Detection in Gel.....	39
3.3.2	Experiment B: Tissue Treatment.....	40
3.3.3	2D Imaging .....	41
3.4	Discussion.....	42
3.4.1	Cavitation Detection without a Gel Matrix.....	42
3.4.2	Detecting the First Bubble Cloud in Tissue .....	42
3.4.3	Lesion Monitoring Through Cloud Detection .....	43
3.4.4	Lesion Monitoring Through T2-Weighted Imaging.....	43
3.4.5	Real Time 2D Targeting and Monitoring .....	44
3.5	Conclusion.....	45
3.6	References.....	45
Chapter 4: Response of MR Contrast Parameters to Treatment by Histotripsy in Various Ex Vivo Tissues and Tissue Mimicking Materials .....		49
4.1	Introduction .....	49
4.2	Materials and Methods.....	50
4.2.1	Transducer Design and Lesion Formation in Ex Vivo Tissues .....	50
4.2.2	Ex Vivo Tissue and Phantom Preparation.....	51
4.2.3	MRI Imaging.....	53
4.3	Longitudinal Relaxation (R1) .....	56
4.3.1	Mechanism .....	56
4.3.2	Results.....	58
4.3.3	Discussion .....	59

4.4	Transverse Relaxation (R2)	60
4.4.1	Mechanism	60
4.4.2	Results	60
4.4.3	Discussion	61
4.5	Diffusion (ADC)	63
4.5.1	Mechanism	63
4.5.2	Results	63
4.5.3	Discussion	64
4.6	In Vivo Lesion	64
4.6.1	Introduction	64
4.6.2	Methods	65
4.6.3	Results	66
4.6.4	Discussion	67
4.7	Study Limitations	68
4.8	Conclusion	69
4.9	References	70
Chapter 5: On The Origin of T2 Contrast in Histotripsy Lesions		74
5.1	Introduction	74
5.1.1	Tissue T2 Shortening by Iron	75
5.1.2	Disruption by Histotripsy	77
5.2	Methods	78
5.2.1	Sample preparation	78
5.2.2	Transducer and Ablation	78
5.2.3	MR Measurement and Analysis	79
5.3	Results	81
5.4	Discussion	82

5.4.1	Removal of the Outer Sphere Mechanism .....	82
5.4.2	Theoretical Models.....	83
5.4.3	Histotripsy and the LM and JC Models .....	84
5.4.4	Future Work.....	85
5.5	Conclusion.....	85
5.6	References.....	85
Chapter 6: Summary and Future Work.....		90
6.1	Summary .....	90
6.2	Future Work .....	92
6.2.1	Cavitation Imaging.....	92
6.2.2	Lesion Feedback Mechanisms .....	95
6.3	Adaptation for Clinical Applications .....	96
6.3.1	In Vivo Contrast.....	96
6.3.2	Non-Destructive Targeting.....	98
6.4	Conclusions .....	98
6.5	References.....	98
Appendices.....		100

## List of Figures

Figure 2.1: Experimental setup. (A) The acoustic pulses emitted from the piezoelectric elements (\*) converge at the focus (yellow lines). The imaging plane transects the focus and the transducer (blue surface). Two different water baths can be attached to the transducer to keep the beam path submerged in water. A spin-echo image of the larger water bath is shown in (B). The smaller-necked water bath is shown in (C). A trigger pulse can be sent from the MR pulse controller to the US amplifier at various times during an imaging sequence as chosen by the operator. (D) The acoustic waveform at the focus generated with maximum driving voltage as estimated by summing together the outputs of the individual elements. ....14

Figure 2.2: Schematic of pulse sequences used: (A) GRE, spin-warp, IVIM sequence used in experiments A , B.1, and C. The cavitation event occurs just after the first IVIM gradient lobe (red arrow) while separation time is incremented. (B) GRE, spin-warp, IVIM sequence used in experiment B.2. The separation time between the IVIM gradients is held constant while the amplitude is incremented. (C) GRE, spin-warp pulse sequence used in experiment D. The ultrasound pulse is fired at different times before signal acquisition (red arrows). (D) GRE EPI sequence used in experiment E. Ultrasound pulses are either fired 10 ms before RF acquisition to desensitize the sequence to cavitation IVIM, or fired between the slice-select and slice-rewind gradient lobes to sensitize the sequence to cavitation IVIM. Each instance/increment is shown as a dotted line for clarity. Amplitudes and time gaps are not to scale. Abbreviations are: RF=radio frequency, SS=slice select, RO=readout, PE=phase encode, US=ultrasound. ....16

Figure 2.3: (A) Gradient echo image acquired with the sequence shown in Fig. (2.A) and with the voltage across the US amplifier set below the cavitation threshold. (B) Image acquired by the same sequence but with the voltage across the US amplifier set above the cavitation threshold. Attenuation factor: 0.25; bvalue: 0.47 smm<sup>-2</sup>. The cavitation event causes localized attenuation of signal magnitude (block arrow). Additionally, the cavitation

event causes signal enhancement due to through-plane motion (solid arrow) as well as ghosting (dotted arrow) along the phase-encode direction (up/down). (C) The same image as in (B) but with the ROI used for calculations highlighted as bright pixels.....19

Figure 2.4: Results corresponding to experiment A. The attenuation factors found at the cavitation site for various applied acoustic pulses are plotted vs. the peak negative pressure of those acoustic pulses. The attenuation factor remains near unity until the peak negative pressure of the ultrasound pulse approaches 24 MPa, where it decreases dramatically with increased peak negative pressure. This threshold pressure matches up with previous studies of cavitation in unfiltered tap water. ....20

Figure 2.5: Results corresponding to experiments B-C. (A) The attenuation factor at the cavitation site estimated from experiment B is plotted vs. the **b** value of the IVIM-encoding gradients. MR signal attenuation is greater when motion is sensitized by separating the gradient lobes (X) than by increasing the gradient strength (O) even for experiments with equivalent b-values. (B) The attenuation factors found at the cavitation site for experiment C are plotted vs. the **b** value of the IVIM-encoding gradients. The IVIM-encoding gradients were played along the readout (X), phase-encode (O), and slice-select ( $\Delta$ ) directions. The **b** value was increased by incrementing the mixing time between IVIM gradient lobes. The behavior of the attenuation factor is isotropic with gradient direction. Note that these b-values are extremely small, which suggests a very large amount of IVIM compared to thermal diffusion and tissue perfusion processes. ....21

Figure 2.6: Example (A) magnitude and (B) phase image from the results of experiment C. For this image, separation time=3.5 ms; b value = 0.53  $\text{mm}^2$ ; attenuation factor=0.32. The IVIM gradients are applied along the phase encode direction (up/down). Water above and below the cavitation site accrue opposite phases and may be due to coherent flow patterns induced by cavitation. ....22

Figure 2.7: Results corresponding to experiment D. The attenuation factor is plotted as a function of the time (in ms) between the US pulse and the RF excitation pulse. The small sinc shape represents the time taken up by the RF pulse. The MR signal is most attenuated when the cavitation event occurs just before either the slice-select or the readout gradient pulses. ....23

Figure 2.8: Results corresponding to experiment D. EPI images acquired during therapy with (A) ultrasound pulses fired 10 ms before the start of the slice select gradient

and (B) ultrasound pulses fired between the slice-select and slice-rewind gradients. A  $T_2^*$  enhanced lesion is apparent in (A) at the therapy focus. Localized attenuation from a cavitation cloud is shown in (B). The pixel-wise subtraction image between (A) and (B) is shown in (C). In this manner, the attenuation caused by cavitation can be isolated from other image features and incoherent motion processes. ....23

Figure 3.1: Experimental setup used in this paper. A histotripsy transducer was placed in the bore of an MR scanner. A tissue sample (red, vertical rectangle) was placed at the transducer focus (ellipse). A surface coil was placed about the sample and used to monitor therapy by imaging a plane transecting the focus (blue, horizontal rectangle). The cavity between the elements of the transducer and the cap was filled with degassed saline solution. ....34

Figure 3.2: Diagrams of histotripsy sensitized MR pulse sequences used in this study. A) 1-D, spin-echo, line-scan sequence. B). 2-D EPI sequence. Both sequences are sensitized to histotripsy by synchronizing a bipolar gradient waveform with a single, 5  $\mu$ s histotripsy acoustic pulse (red arrow). Experiments were conducted by using these sequences to repeatedly image the transducer focus. Each new instance of the sequence would simultaneously apply and monitor an additional acoustic pulse to the target. Abbreviations: RF: Radio Frequency, SS: Slice Select, PE: Phase Encode, RO: Readout, US: Ultrasound....34

Figure 3.3: Slice planning for the orthogonal excitation pulse. A) A sacrificial sample is placed in the transducer focus. B) A cavitation-sensitized 2D sequence was used to locate the focus and plan the orthogonal refocusing plane (green lines). C) The refocusing slice is rotated to excite a column that transects the transducer focus. D) Resulting 1D line scans. The histotripsy bubble cloud creates localized signal loss that is easily detected when compared to the control case. ....35

Figure 3.4: Probability–pressure data and fitted curves obtained using the cavitation sensitized line-scan sequence and the passive cavitation detection (PCD) system. The PCD and MRI based methods show a 0.5 probability cavitation threshold at 26.4 and 26.6 MPa peak negative pressures respectively. These measurements were taken in a gel sample pre-treated with 1000 histotripsy pulses. Intact tissues, unlike the gel sample used here, may interfere with water motion and inhibit the performance of the MR sequence. ....39

Figure 3.5: The mean (dark line) and standard deviation (light envelope) of the motion weighted and T2-weighted signal (T2W) at the cavitation site vs the number of

acoustic pulses applied to the sample. For images acquired at low spatial frequencies, signal loss caused by cavitation is not immediately differentiable from the T2-weighted signal, where cavitation-based motion is not present. However, this signal does become differentiable after several acoustic pulses are applied to the tissue target. At high spatial frequencies, cavitation specific contrast is immediately apparent and remains differentiable over the course of treatment. The T2-weighted signal in liver increases with treatment pulse number, but remains constant in brain. ....40

Figure 3.6: Echo-planar images (EPI) of a sample of brain tissue taken (A) prior to therapy, and (B) over the first two acoustic pulses applied to the sample. The sensitizing gradient extends to a k-space frequency of  $300 \text{ cm}^{-1}$ . The bubble clouds applied in (B) cause localized signal attenuation as indicated by the arrow. Dividing the image in (B) by the image in (A) isolates cavitation specific contrast and the result is shown in (C). The EPI sequence is able to detect and localize the first two histotripsy pulses applied to the tissue sample. ....42

Figure 4.1: Example acoustic pulse (left), transducer setup (center) and acoustic pulse deposition patterns (right) used to form lesions in ex vivo tissues. Six lesions, each made by depositing different numbers of acoustic pulses per point (pls/pt) are made on a single plane perpendicular to the propagation axis. The target was translated such at 4 planes of lesions were formed in each sample. ....51

Figure 4.2: Top Row: Examples of the signal decay curves and their least squares fits obtained while computing the ADC (Left), R1 (Center), and R2 (Right) of clot. The fits with the highest and lowest squared correlation coefficient ( $R^2$ ) are both displayed. In these plots, X's correspond to the MR signal of the lesion that produced the lowest  $R^2$  value as a function of either b value,  $T_i$ , or  $T_e$ . The circles correspond to the signal of the lesion that produced the largest squared correlation coefficient as a function of either b value,  $t_i$ , or  $t_e$ . Bottom row: The  $R^2$  values for all fits produced in this study. Clot produced the largest number of poor fits due to low image signal in regions where it was not ablated. However, most of the fits performed in this study match the acquired data rather well. ....56

Figure 4.3: Means and standard deviations of the estimated R1 rates of lesions made in the materials tested in this study. Materials are separated by color and are labeled on the x-axis. The number of acoustic pulses deposited per grid point in each lesion is labeled in white on each bar. The estimated R1 rates of liver, kidney, muscle and brain appear be invariant to ablation by histotripsy. However, the R1 rates of clot and all three red blood cell

phantoms display sensitivity to ablation, possibly because of the release of methemoglobin when the blood cells are lysed. ....59

Figure 4.4: Means and standard deviations of the estimated R2 rates of lesions made in the materials tested in this study. Materials are separated by color and are labeled on the x-axis. The number of acoustic pulses deposited per grid point in each lesion is labeled in white on each bar. With the exception of brain, the estimated R2 rates of all materials tested here decrease with ablation. The magnitude to change in R2 rates varies dramatically between tissue type, with the R2 rate of clot responding particularly strongly. The R2 rate of brain appears to increase, which is likely due to partial volume effects and poor discrimination between white and grey matter. ....61

Figure 4.5: Dark Bars: Mean and standard deviation of iron concentration found in the literature (Refs 35-42) in porcine liver, kidney, muscle. White Bars: Mean and standard deviation of the change in R2 rate between nominal and maximally treated porcine liver, kidney, muscle and brain tissues. There is a correlation between iron content and the magnitude of change in R2 rate that accompanys histotripsy ablation in liver, kidney, and muscle. The poor correlation between the change in R2 rate and iron concentration in brain tissue may be caused by, 1, a bias in iron concentration estimation that represents older, more iron laden brains, and, 2, partial volume effects that have skewed the measured R2 in lesions in brain to include both white and grey matter. ....62

Figure 4.6: Means and standard deviations of the estimated ADC values of lesions made in the materials tested in this study. Materials are separated by color and are labeled on the x-axis. The number of acoustic pulses deposited per grid point in each lesion is labeled in white on each bar. The ADC value of all materials tested here increase in response to ablation by histotripsy. This is likely because histotripsy breaks apart cellular membranes, allowing water to more freely diffuse through the material. ....64

Figure 4.7: Setup of in vivo ablation of porcine liver. Ultrasound was delivered trans-abdominally for 15 minutes with a PRF of 50 Hz. A water bolus was used to couple the therapy transducer to the target. During treatment the transducer was mechanically scanned through a grid pattern, depositing 3000 pulses per point. After treatment, the liver was excised and imaged. ....66

Figure 4.8: An R2-weighted image (R2W) and corresponding R2, ADC, and R1 maps of the lesion formed in in vivo porcine liver. The lesion displays a large change in R2 and



ADC and a much less well defined change in R1. These features match well to the results in ex vivo tissue displayed above. However, some in vivo effects can be seen in the image: a small rim of hemorrhage can be observed surrounding the lesion, followed by another faint rim of edema, and the R2 and ADC contrast within the lesion is not uniform.....67

Figure 5.1: Experimental setup: Histotripsy bubble clouds are formed in vacuum packed liver using a hemispherical, 500 kHz, electronically steered ultrasound array. ....78

Figure 5.2: Example T2 signal decay curves from a scan taken with an echo spacing of 5 ms. In (A) unconstrained fits to Eq 5.1 are made the full data set (solid line) and to a subsample of points at 45, 70, 95, and 120 ms (dashed line). The subsampled fit demonstrates the instability of Eq 1 and underestimates the maximum signal amplitude and the T2 time. In (B) the subsampled fit is constrained to have the same initial amplitude as the unconstrained fit using the full data set. This fit converges to the same values and the fully sampled set and corrects for the sub sampling error. Constrained fits were used to correct this error for all echo times used in this study. ....80

Figure 5.3: T2 weighted images of the liver sample, each taken at an echo that occurs at 40 ms after the initial excitation pulse. The histotripsy lesion appears as a bright rectangle with sharp borders. The sequence that acquired the left hand image image was taken with an echo spacing,  $2\tau$ , of 5 ms, while the right hand image was taken with an echo spacing of 20 ms. Both images have identical grayscale windows. Though the two images are of identical samples and were taken at the same echo time, the right hand image exhibits a shorter T2 time, which results in a darker appearing liver. ....81

Figure 5.4: The  $1/T_2$  rate estimated in both nominal liver and the histotripsy lesion as a function of the echo spacing used to acquired the measurement. The  $1/T_2$  rate in nominal liver displays a characteristic dependence on the echo spacing. The  $1/T_2$  rate in the ablated lesion is invariant to the echo spacing used to make the measurement. The solid and dashed lines are least squares fits of the date to the Jensen-Chandra model (solid line) and the Luz-Meiboom model (dashed line). See refs 27, 46, 47. These models suggest that the independence of the  $1/T_2$  rate of the histotripsy lesion stems from the erosion of the paramagnetic nodules that drive the outer sphere mechanism. ....82

Figure 6.1: Cavitation sensitized images of a red blood cell phantom that has been treated by depositing thousands of histotripsy pulses to a single location. Lysed red blood cells appear as a bright teardrop shape while surrounding the intact red blood cells are dark.

Cavitation sensitized images with a sensitivity of (A) 1 and (B) 256 cm<sup>-1</sup> display varying distributions of motion induced signal loss. The image loss in neither (A) or (B) fully matches the teardrop shape. Future work can investigate the accuracy of MR cavitation imaging at predicting the extent of an ablated volume. ....94

Figure 6.2: An MR shearwave image of a gel phantom. Shearwaves propagate through the rectangular gel phantom in the direction indicated by the black arrow. A small inclusion was placed in the gel to simulate a histotripsy lesion (asterisk). The inclusion can be identified as the location where the shear waves are disrupted. MR shearwave imaging is part of MR elastography and may be a useful way to identify and measure histotripsy lesions. ....96

Figure 6.3: A block M shaped lesion formed in an in vivo porcine brain model. Much of the M shaped lesion has been infiltrated by deoxygenated blood, which appears dark in the MR image. However, one leg of the M was retreated several minutes after the original ablation. This leg appears quite bright, likely because the second pass lysed the red blood cells in this region. Future work can investigate the relationships between bleeding, treatment history and the appearance of lesions made in vivo.....97

## List of Tables

Table 4.1: MR acquisition parameters used to acquire R1, R2 and ADC weighted images of histotripsy lesions made in several ex vivo tissues and tissue mimicking phantoms. Abbreviations are FOV = field of view, TR = repetition time, TE = echo time, TI = inversion recovery time, b value = diffusion weighting constant. ....	54
Table 5.1: Estimated fit terms from the Luz-Meiboom (LM) and Jensen-Chandra (JC) models of outer-sphere driven relaxation. The models were fit to the $1/T_2$ rates estimated in both nominal liver and the histotripsy lesion. The term $1/T_{2_0}$ refers to the base relaxation of the tissue without the outer sphere mechanism. The terms K and G reflect the magnetic properties of the microscopic environment as well as the populations of water molecules in each environment. The term <b>T</b> refers to the average time a water molecule can diffuse along the radius of a paramagnetic protein aggregate.....	84

## List of Equations

Eq: 1.1 .....	3
Eq: 1.2 .....	4
Eq: 2.1 .....	11
Eq: 2.2 .....	11
Eq: 2.3 .....	12
Eq: 4.1 .....	55
Eq: 4.2 .....	55
Eq: 4.3 .....	55
Eq: 5.1 .....	80
Eq: 5.2 .....	83
Eq: 5.3 .....	83
Eq: 5.4 .....	83
Eq: 6.1 .....	92
Eq: 6.2 .....	93
Eq: 6.3 .....	93
Eq: 6.4 .....	93

## **List of Appendices**

Appendix A: Programming Code for 7T Agilent Magnetic Resonance Scanner.....	100
Appendix B: Spiral Sequences on the Agilent 7T Scanner .....	110

## Abstract

Histotripsy is a cavitation based surgical therapy that transmits high amplitude acoustic pulses into a tissue target to stimulate the formation of energetic clouds of microbubbles. These microbubble clouds then exert a mechanical load on the surrounding cellular and extracellular structure, and, eventually, render a precise volume of tissue into a liquid homogenate devoid of any visible cellular structure. This technology has many potential applications including the erosion of intracranial blood clots, deep vein thrombi, liver tumors, and kidney stones.

Histotripsy is a non-invasive surgery and cannot ensure the accurate ablation of the target without an accompanying image-based guidance system. The objective of this dissertation is to explore and develop magnetic resonance imaging (MRI) based tools to 1) visualize and monitor the cavitation process within the ablation target and 2) assess the state of the target after ablation.

To this end, this dissertation proposes and characterizes a novel cavitation imaging scheme to visualize the histotripsy process. The technique employs synchronized bipolar gradients as a simultaneous temporal and magnitude filter that selectively sensitizes the resulting image to incoherent water flow generated by the histotripsy bubble cloud. It is shown to be easily integrated into various image acquisition schemes. When used with single-shot, fast imaging schemes, the technique can simultaneously localize individual bubble clouds and provide feedback on the ablated state of the target.

The dissertation then examines the response of several basic MR signal evolution processes as tissues are ablated by histotripsy. These processes are related to the diffusion and interaction of water molecules within a tissue and are characterized by the time constants  $T_1$ , and  $T_2$ , as well as a diffusion coefficient. The work presented here demonstrates that the magnitude of response of these processes is specific to both the tissue target and the treatment history. Further, the response of the process characterized by  $T_2$  is

shown to depend the ability of the bubble cloud to erode and disperse aggregations of paramagnetic proteins such as hemoglobin and ferritin.

Together, this dissertation provides useful magnetic resonance imaging tools for the visualization and assessment of histotripsy therapy.

# Chapter 1:

## Introduction

The purpose of this dissertation is to investigate magnetic resonance imaging (MRI) based methods to guide histotripsy therapy. More specifically, this work strives to accomplish two tasks:

1. Visualize the histotripsy bubble cloud relative to the surrounding tissue material.
2. Assess the extent of damage induced by a given histotripsy treatment.

Chapters 2 and 3 of this work will address question one by devising a novel method to sensitize MR imaging sequences to histotripsy bubble clouds. Chapters 4, 5, and a portion of chapter 3 will address question two by characterizing the response of different MR signal processes in biologic tissues to exposure by histotripsy. Appendices A and B will present various specialized MR pulse sequences that have been used throughout this dissertation to answer questions one and two.

The following chapter will present a brief introduction to histotripsy followed by another discussion of the relevant MR physics that are referenced in this work. It will then conclude with an overview of each chapter within this dissertation.

### 1.1 Histotripsy

Histotripsy is a non-invasive surgical procedure that uses acoustic pulses to stimulate the formation of dense clouds of microbubbles within a malignant biologic tissue. The formation, collapse and dissolution of these microbubble clouds exert a mechanical load on their surrounding soft tissues. Repeated exposure to these bubble clouds renders nominally cellular tissue into a homogenous slurry [1]–[4] which can then be absorbed by the body, leaving a fluid filled cavity [5]. The physics behind histotripsy allow a great deal of control over the volume of tissue that can be liquefied [6], [7], even in locations within the skull or behind the ribs where bone will partially disrupt the propagation of ultrasound [8], [9]. In



particular, the threshold mechanism that governs the stimulation of histotripsy bubble clouds allows the location and frequency of cloud formation to be highly controlled by the acoustic pulsing scheme [6], [7], [10], [11]. Histotripsy has shown potential to treat malignancies in several tissues such as brain [12], [13], liver [8], [9], kidney [14], and the femoral vein [15], [16].

There are two particularly salient features of histotripsy. The first is that, during histotripsy, the bubble cloud is the effective mechanism by which tissue is destroyed [1], [17]. Homogenization occurs when repeated cycles of histotripsy cavitation erode and break down the mechanical structure of tissue. Though spatially confined, these bubble clouds are extremely violent and are known to produce powerful water flows in a fluid [18], [19]. These bubbles expand and collapse over a lifespan on the order of hundreds of microseconds [20]. Their associated water motion can persist for a much longer time [21].

The second feature is related to the first: the cavitation cloud is the only mechanism that exerts an observable influence on the tissue. The acoustic pulses used to stimulate histotripsy have very high amplitudes and deposit a great deal of energy into the target tissue. However, these pulses are emitted at such small duty cycles that tissue dissipates this energy prior to the arrival of the next pulse. Thus, there is no accompanying rise in tissue temperature during histotripsy sonication [22]. This is in sharp contrast to thermal focused ultrasound therapies, where low amplitude, high duty cycle pulses induce cell necrosis through heat deposition and thermal buildup [23].

Ultrasound thermal therapies can be visualized using MR-thermometry, which takes advantage of the temperature sensitivity of several MR processes to measure the thermal build-up process [24]. Histotripsy cannot be visualized using these methods.

With no associated temperature build-up, the only observable mechanisms that occur during histotripsy therapy are the bubble clouds themselves and their effects on the tissue. The work here will develop new MR imaging methods that will be sensitive to mechanisms associated with the bubble cloud: water flow and tissue homogenization. For this purpose, it will be necessary to visit some of the mechanisms that drive MR signal evolution and image contrast.

## **1.2 MRI Signal Phase**

This section will address some of the physics behind MR signal phase and its effects on image contrast. Much of the work in this dissertation relies on these physics and will be referenced often. A complete review of MR physics, including the material here, can be found in reference [25].

The MR signal originates from the precession of the magnetic moment of hydrogen protons about a large applied magnetic field. Each moment has its own accompanying magnitude and phase. This phase is measured relative to the other moments that coexist within a volume. The signal strength of any given image volume element (voxel) is proportional to the vector summation of these magnetic moments. Since these moments are very small and a very large number of them exist within any practical image voxel, this summation can be well approximated by the integral.

$$S(t) \propto \int \rho e^{-i\phi(t)} dv \quad \text{E q: 1.1}$$

Where  $S(t)$  is the time dependant strength of the voxel signal,  $\rho$  is the density of moments,  $dv$  is an infinitesimally small volume, and  $\phi(t)$  is the time dependent phase of each moment in the volume.

The phase term  $\phi(t)$  is time dependent because each magnetic moment precesses at a rate proportional to the magnetic field that it experiences. When the magnetic field is non uniform, the moments exposed to different field strengths will accrue phase relative to each other. As the distribution of the phases within a voxel broadens from a single value to a span of values, the moments within the integral in Eq. 1.1 begin to add destructively. If the phase distribution spans beyond  $\pi/2$  radians,  $S(t)$  can decrease dramatically. For example,  $S(t)$  is obliterated when the phase distribution spans evenly across  $2\pi$  radians.

### 1.2.1 T2 Relaxation

The phase distribution caused by inhomogeneous magnetic fields plays a very fundamental role in MR signal evolution. The magnetic moments of the two hydrogen atoms on a water molecule are each exposed to the magnetic field generated by the other atom. Further, the two atoms naturally tumble about the much heavier oxygen atom in a random manner, causing the magnetic fields experienced by the two hydrogen atoms to fluctuate randomly. This random motion, along with the fluctuating fields, introduces a relative phase between the two moments that varies randomly with time. Though these variations are random, their probability distribution is predictable and broadens with time. A

voxel filled with an Avogadro's number's worth of hydrogen protons effectively samples the entire probability distribution, allowing one to write

$$S(t) \propto \int \rho P_\phi(t) e^{-i\phi} d\phi \quad \text{E} \quad \text{q: 1.2}$$

Where  $P_\phi(t)$  is the time dependant probability distribution of the phase between any two magnetic moments.

In pure water and other simple systems, the term  $\int P_\phi(t) e^{-i\phi} d\phi$  can be shown to be proportional to an exponential decay and is often characterized by the time constant T2:  $e^{-t/T2}$ . This process is fundamental to the MR signal and is often called transverse relaxation, or T2 decay [26]–[28].

Aside from the tumbling of hydrogen atoms, other natural and artificial mechanisms can introduce additional phase decoherence which further attenuate the MR signal. These mechanisms include the introduction of paramagnetic ions to the voxel, the bonding of water to large molecules with slow tumbling rates, magnetic field perturbations caused by paramagnetic bodies, and static field gradients produced by the scanner equipment. Whether caused on purpose or by accident, these processes manipulate the relative phase of the hydrogen magnetic moments within an image voxel. They account for image contrast in the majority of clinical MR images. In fact, the bulk of the following dissertation will concern itself with the sensitivity of such processes to histotripsy. In this light, it is important to introduce a mechanism by which a scanner operator can selectively introduce phase to non-stationary magnetic moments.

### 1.2.2 The Bipolar Gradient

Modern MR scanners are equipped to produce a magnetic field that varies linearly with space. The strength and direction of the gradient of this magnetic field can be controlled at will and pulsed with respect to time. A particularly useful set of gradient pulses is called the bipolar gradient waveform. When the scanner plays out this waveform, the magnetic field is made to increase in strength along one direction for a period of time. The polarity of this gradient is then reversed but kept at equal magnitude for an equal duration. During the first half of the sequence, magnetic moments oriented along the direction of the gradient of the field accrue relative phase proportional to their location. During the second half of the sequence, these moments accrue negative relative phase proportional to their

location. If the moments do not change locations, then the accrued phase from each half of the waveform negate each other. However, magnetic moments that do change location during the sequence end up with some net relative phase. If these location changes are random, then the resulting phase is also random and the net phase distribution within a voxel broadens.

The bipolar gradient waveform is especially useful for sensitizing an MR imaging sequence to incoherent motion processes such as diffusion [29], [30]. Regions with enhanced incoherent motion present enhanced signal loss in their corresponding images. This technique is quite general and can be extended beyond diffusion to any form of incoherent motion. In chapters 2 and 3 we will demonstrate that it can be extended to visualizing histotripsy.

### 1.3 Outline of Chapters

This dissertation examines MR based techniques for visualizing and assessing histotripsy therapy. It is organized into six chapters

**Chapter 1** describes the objective of this dissertation. It introduces both histotripsy and some relevant MR physics. Additionally, it gives an outline of the dissertation.

**Chapter 2** examines using bipolar gradients to sensitize an MR imaging sequence to the histotripsy cavitation cloud. In particular, it investigates the dependence of the observed signal loss on acoustic pressure, gradient amplitude and separation time, and the relative timing between the occurrence of the cavitation cloud and the sensitizing gradient waveform.

**Chapter 3** explores using these sensitizing gradients as a means to visualize individual instances of a bubble cloud. It examines a relationship between signal output, treatment history, and gradient sensitivity.

**Chapter 4** examines the response of the observed  $T_1$  and  $T_2$  relaxation constants as well as the apparent diffusion coefficient in various ex vivo tissues and phantoms to ablation by histotripsy. Additionally, it performs a histological analysis on histotripsy lesions and correlates some of these findings to changes in  $T_1$ ,  $T_2$ , and the diffusion coefficient.

**Chapter 5** proposes that  $T_2$  weighted image contrast of histotripsy lesions is driven by the organization of paramagnetic iron bearing proteins within different tissue types. It

examines how such structure makes the observed T2 time of tissue depend on the parameters used to make the measurement. It then explores how ablation by histotripsy disrupts this dependence in liver tissue.

**Chapter 6** summarizes the work presented here and discusses future research and applications for MRI guided histotripsy therapy.

In addition to the above chapters, this dissertation contains two appendices.

**Appendix A** contains instructions for generating the appropriate computer code to drive the experiments contained in chapters 2 and 3 using an Agilent MR scanner. **Appendix B** contains instructions for generating the appropriate computer code to implement single-shot, fast spiral imaging on the same scanner.

## 1.4 References

- [1] V. A. Khokhlova, J. B. Fowlkes, W. W. Roberts, G. R. Schade, Z. Xu, T. D. Khokhlova, T. L. Hall, A. D. Maxwell, Y.-N. Wang, and C. A. Cain, "Histotripsy methods in mechanical disintegration of tissue: Towards clinical applications," *Int. J. Hyperth.*, vol. 31, no. 2, pp. 145–162, Mar. 2015.
- [2] Z. Xu, A. Ludomirsky, L. Y. Eun, T. L. Hall, B. C. Tran, J. B. Fowlkes, and C. a Cain, "Controlled ultrasound tissue erosion," *IEEE Trans. Ultrason. Ferroelectr. Freq. Control*, vol. 51, no. 6, pp. 726–736, Jun. 2004.
- [3] J. E. Parsons, C. a Cain, G. D. Abrams, and J. B. Fowlkes, "Pulsed cavitation ultrasound therapy for controlled tissue homogenization," *Ultrasound Med. Biol.*, vol. 32, no. 1, pp. 115–129, Jan. 2006.
- [4] Z. Xu, Z. Fan, T. L. Hall, F. Winterroth, J. B. Fowlkes, and C. a. Cain, "Size Measurement of Tissue Debris Particles Generated from Pulsed Ultrasound Cavitation Therapy – Histotripsy," *Ultrasound Med. Biol.*, vol. 35, no. 2, pp. 245–255, Feb. 2009.
- [5] T. L. Hall, K. Kieran, K. Ives, J. B. Fowlkes, C. A. Cain, and W. W. Roberts, "Histotripsy of rabbit renal tissue in vivo: temporal histologic trends.," *J. Endourol.*, vol. 21, no. 10, pp. 1159–1166, 2007.
- [6] K. W. Lin, Y. Kim, A. D. Maxwell, T. Y. Wang, T. L. Hall, Z. Xu, J. B. Fowlkes, and C. A. Cain, "Histotripsy beyond the intrinsic cavitation threshold using very short ultrasound pulses: microtriopsy," *IEEE Trans. Ultrason. Ferroelectr. Freq. Control*, vol. 61, no. 2, pp. 251–265, 2014.
- [7] K.-W. Lin, A. P. Duryea, Y. Kim, T. L. Hall, Z. Xu, and C. A. Cain, "Dual-beam histotripsy: a low-frequency pump enabling a high-frequency probe for precise lesion formation," *IEEE Trans. Ultrason. Ferroelectr. Freq. Control*, vol. 61, no. 2, pp. 325–340, Feb. 2014.
- [8] E. Vlaisavljevich, Y. Kim, S. P. Allen, G. Owens, S. Pelletier, C. A. Cain, K. Ives, and Z. Xu, "Image-guided non-invasive ultrasound liver ablation using histotripsy:

- feasibility study in an in vivo porcine model,” *Ultrasound Med. Biol.*, vol. 39, no. 8, pp. 1398–1409, 2013.
- [9] Y. Kim, T. Y. Wang, X. Zhen, and C. A. Cain, “Lesion generation through ribs using histotripsy therapy without aberration correction,” *IEEE Trans. Ultrason. Ferroelectr. Freq. Control*, vol. 58, no. 11, pp. 2334–2343, 2011.
- [10] K.-W. Lin, T. L. Hall, Z. Xu, and C. A. Cain, “Histotripsy Lesion Formation Using an Ultrasound Imaging Probe Enabled by a Low-Frequency Pump Transducer,” *Ultrasound Med. Biol.*, vol. 41, no. 8, pp. 2148–60, Aug. 2015.
- [11] K. W. Lin, T. Hall, R. McGough, Z. Xu, and C. Cain, “Synthesis of monopolar ultrasound pulses for therapy: The frequency-compounding transducer,” *IEEE Trans. Ultrason. Ferroelectr. Freq. Control*, vol. 61, no. 7, pp. 1123–1136, 2014.
- [12] Y. Kim, T. L. Hall, Z. Xu, and C. A. Cain, “Transcranial histotripsy therapy: A feasibility study,” *IEEE Trans. Ultrason. Ferroelectr. Freq. Control*, vol. 61, no. 4, pp. 582–593, 2014.
- [13] J. Sukovich, Z. Xu, Y. Kim, H. Cao, T.-S. Nguyen, A. Pandey, T. Hall, and C. Cain, “Targeted Lesion Generation Through the Skull Without Aberration Correction Using Histotripsy,” *IEEE Trans. Ultrason. Ferroelectr. Freq. Control*, vol. 3010, no. c, pp. 1–1, 2016.
- [14] A. P. Duryea, A. D. Maxwell, W. W. Roberts, Z. Xu, T. L. Hall, and C. A. Cain, “In vitro comminution of model renal calculi using histotripsy,” *IEEE Trans. Ultrason. Ferroelectr. Freq. Control*, vol. 58, no. 5, pp. 971–80, May 2011.
- [15] A. D. Maxwell, G. Owens, H. S. Gurm, K. Ives, D. D. Myers, Z. Xu, D. D. Myers Jr, and Z. Xu, “Noninvasive Treatment of Deep Venous Thrombosis Using Pulsed Ultrasound Cavitation Therapy (Histotripsy) in a Porcine Model,” *J. Vasc. Interv. Radiol.*, vol. 22, no. 3, pp. 369–377, 2011.
- [16] X. Zhang, G. E. Owens, H. S. Gurm, Y. Ding, C. A. Cain, A. Arbor, C. Diseases, A. Arbor, and A. Arbor, “Non-invasive Thrombolysis using Histotripsy beyond the ‘Intrinsic’ Threshold (Microtripsy),” *IEEE Trans Ultrason Ferroelectr Freq Control*, vol. 62, no. 734, pp. 1342–1355, 2015.
- [17] M. Hoogenboom, D. Eikelenboom, M. H. den Brok, A. Heerschap, J. J. Fütterer, and G. J. Adema, “Mechanical High-Intensity Focused Ultrasound Destruction of Soft Tissue: Working Mechanisms and Physiologic Effects,” *Ultrasound Med. Biol.*, Mar. 2015.
- [18] A. D. Maxwell, C. A. Cain, A. P. Duryea, L. Yuan, H. S. Gurm, and Z. Xu, “Noninvasive thrombolysis using pulsed ultrasound cavitation therapy - histotripsy,” *Ultrasound Med. Biol.*, vol. 35, no. 12, pp. 1982–94, Dec. 2009.
- [19] S. Park, A. D. Maxwell, G. E. Owens, H. S. Gurm, C. A. Cain, and Z. Xu, “Non-Invasive Embolus Trap Using Histotripsy—An Acoustic Parameter Study,” *Ultrasound Med. Biol.*, vol. 39, no. 4, pp. 611–619, 2013.
- [20] Zhen Xu, M. Raghavan, T. L. T. L. Hall, Ching-Wei Chang, M.-A. A. Mycek, J. B. B. Fowlkes, C. A. Cain, Z. Xu, M. Raghavan, T. L. T. L. Hall, C. W. Chang, M.-A. A. Mycek, J. B. B. Fowlkes, C. A. Cain, C. Ching-Wei, M.-A. A. Mycek, J. B. B. Fowlkes, C. A. Cain, C. W. Chang, M.-A. A. Mycek, J. B. B. Fowlkes, and C. A. Cain, “High speed imaging of bubble clouds generated in pulsed ultrasound cavitation therapy-

- histotripsy,” *IEEE Trans. Ultrason. Ferroelectr. Freq. Control*, vol. 54, no. 10, p. 2091, Oct. 2007.
- [21] X. Zhang, R. M. Miller, K.-W. Lin, A. M. Levin, G. E. Owens, H. S. Gurm, C. A. Cain, and Z. Xu, “Real-time feedback of histotripsy thrombolysis using bubble-induced color Doppler,” *Ultrasound Med. Biol.*, vol. 41, no. 5, pp. 1386–401, May 2015.
- [22] Y. Kim, E. Vlaisavljevich, G. E. Owens, S. P. Allen, C. A. Cain, and Z. Xu, “In vivo transcostal histotripsy therapy without aberration correction,” *Phys. Med. Biol.*, vol. 59, no. 11, pp. 2553–2568, Jun. 2014.
- [23] J. E. Kennedy, G. R. Ter Haar, and D. Cranston, “High intensity focused ultrasound: surgery of the future?,” *Br. J. Radiol.*, vol. 76, no. 909, pp. 590–599, 2003.
- [24] V. Rieke and K. Butts Pauly, “MR thermometry,” *J. Magn. Reson. Imaging*, vol. 27, no. 2, pp. 376–90, Feb. 2008.
- [25] E. M. Haacke, R. W. Brown, M. R. Thompson, and R. Venkatesan, *Magnetic Resonance Imaging: Physical Principles and Sequence Design*, vol. 1st. 1999.
- [26] N. Bloembergen, E. M. Purcell, and R. V. Pound, “Relaxation Effects in Nuclear Magnetic Resonance Absorption,” *Phys. Rev.*, vol. 73, no. 7, pp. 679–712, Apr. 1948.
- [27] I. Solomon, “Relaxation Processes in a System of Two Spins,” *Phys. Rev.*, vol. 99, no. 2, pp. 559–565, Jul. 1955.
- [28] N. Bloembergen, “Spin Relaxation Processes in a Two-Proton System,” *Phys. Rev.*, vol. 104, no. 6, pp. 1542–1547, Dec. 1956.
- [29] E. O. Stejskal and J. E. Tanner, “Spin diffusion measurements: spin echoes in the presence of a time-dependent field gradient,” *J. Chem. Phys.*, vol. 42, no. 1, pp. 288–292, 1965.
- [30] D. Le Bihan, E. Breton, D. Lallemand, P. Grenier, E. Cabanis, and M. Laval-Jeantet, “MR imaging of intravoxel incoherent motions: application to diffusion and perfusion in neurologic disorders,” *Radiology*, vol. 161, no. 2, pp. 401–407, 1986.

## **Chapter 2:**

# **Sensitizing MR Imaging to Water Motion Caused by the Bubble Cloud.**

A majority component of this chapter has been published in *Magnetic Resonance in Medicine* © 2014 Wiley Periodicals Inc. Reprinted, with permission, from [1].

### **2.1 Introduction**

As discussed in Chapter 1, Magnetic Resonance Imaging (MRI) is a promising candidate for non-invasive, image-based guidance of histotripsy therapy. MR image contrast is sensitive to a wide array of different physical processes, some of which can be influenced by histotripsy. Using fast-imaging methods that can emphasize contrast by these processes over that caused by others, MRI may provide real-time observations of the target during therapy. This chapter introduces a novel method to visualize the histotripsy bubble cloud using MRI.

Previous work has suggested that MR imaging may be made sensitive to cavitating micro-bubbles using gradient-echo [2] and spin-echo [3] images. It is possible that these effects will interfere with MR-guided therapy. For example, signal attenuation caused by the cavitation cloud may mask contrast enhancement generated by tissue homogenization. Conversely, this signal attenuation may be useful for targeting or cavitation verification, and thus be a desirable part of the image. Controlling a sequence's sensitivity to cavitation can help in both these situations.

The use of microbubbles in MRI has been an area of active research. For example, microbubbles have been studied as a potential susceptibility contrast agent [4]–[8]. They have also been used in focused ultrasound therapies to temporarily open the blood brain barrier [9]–[11]. In both of these applications, the microbubbles involved are made of lipid or



protein shells and are injected into the subject's vasculature. In contrast, the study of MR guided histotripsy is unique because the microbubbles involved are thought to originate from small gas nuclei that are native to the target tissue and have much shorter lifetimes than their manufactured counterparts.

Our general hypothesis is that cavitation causes intra-voxel incoherent motion (IVIM) of water molecules. Pulse sequences with high sensitivity to IVIM will show strong contrast at the therapy site, whereas pulse sequences with reduced sensitivity to IVIM will only show the underlying tissue. A combination of these images should provide a precise image of the cavitation process.

## **2.2 Histotripsy**

During histotripsy therapy, microbubbles are generated when an incoming ultrasound pulse with a large peak negative pressure impinges upon small gas nuclei present in the target [12], [13]. These nuclei expand over just a few microseconds into a dense cloud of bubbles, which then collapses over the course of hundreds of microseconds [14], [15]. After collapse, a distribution of bubbles, with diameters on the order of 5  $\mu\text{m}$ , remain present in the fluid for up to several seconds before dissolving [16]. In unpublished work, using high speed camera imaging, we have estimated this residual cloud to have a volume fraction well below 1%.

## **2.3 Flow at Cavitation**

The collapse phase of the cavitation cycle begins when water rushes in at high velocity toward the center of the bubble cloud. During this process, the bubble cloud fragments into many smaller bubbles. The flow patterns within the cavitation region become very complex and can no longer be described as conducted along radial lines toward the center of the cloud. Instead, when observed with high-speed camera imaging, these patterns are incoherent in nature, occur at very high speeds, and rarely repeat from cavitation event to cavitation event. After collapse, the flow patterns gradually return to those of thermal diffusion.

## **2.4 IVIM Imaging**

In intravoxel incoherent motion (IVIM) imaging, the magnitude of the MR signal is attenuated if the water molecules within a voxel travel along random or pseudo-random trajectories while in the presence of balanced field gradients. The technique is an extension of the pulsed-gradient method for diffusion coefficient measurement [17].

Standard pulse sequences such as gradient recalled echo (GRE) and spin-echo sequences can be converted into an IVIM sequence by inserting a bipolar gradient pulse between the RF excitation pulse and signal acquisition [18]. In the presence of these gradient lobes, random motions of water molecules cause a random distribution of phase across a voxel. When these phases are summed together, they add destructively. In an IVIM image, regions of enhanced random motion exhibit reduced signal intensity when compared to regions with restricted perfusion.

It has also been demonstrated that the flow of the water molecules need not be entirely incoherent to observe IVIM contrast, since coherent flow distributed across several velocities will also produce signal attenuation [18]. However, the coherent motion will also introduce some net gain of phase to a voxel. Changes in image phase due to coherent motion play an integral role behind shear-wave [19]–[21], acoustic radiation force [22], [23], and acoustic streaming imaging [24].

During an IVIM imaging experiment, the signal observed at the echo time (TE) can be expressed by

$$A = FA_o \tag{q: 2.1} \quad \text{E}$$

Where  $A_o$  is the magnitude of the MR signal observed at TE if the encoding gradients are disabled. The attenuation factor,  $F$ , depends on both the motions of the water molecules and the encoding gradient waveforms and is also subject to the constraint  $F \leq 1$ .

A simple model for IVIM imaging consists of a voxel where populations of water undergo different forms of isotropic movement. Molecular exchange between populations occurs more slowly than the duration of the imaging sequence. In this case,  $F$  can be calculated using the equation

$$F = \sum_i f_i e^{-bD_i} \tag{q: 2.2} \quad \text{E}$$

Where  $f_i$  is the fraction of water molecules in the  $i^{\text{th}}$  population and  $\sum f_i = 1$ . The term  $D_i$  is the apparent diffusion coefficient of the  $i^{\text{th}}$  population. The term  $b$  takes the form

$$b = \gamma^2 \int_0^{TE} \left[ \int_0^t G(\tau) d\tau \right]^2 dt \quad \mathbf{q: 2.3} \quad \mathbf{E}$$

Where  $\gamma$  is the gyromagnetic ratio and  $G(\tau)$  is the time-dependent vector of the gradient pulses used in the imaging experiment [25].

The work in [26] has shown that contributions to signal attenuation from populations undergoing some sort of non-thermal motion are separable from the contributions caused by those undergoing thermal diffusion. This is because the populations of water undergoing the non-thermal motion often have a larger apparent diffusion coefficient than the populations undergoing solely thermal diffusion. Gradient waveforms can be found with values for  $b$  such that the majority of signal attenuation is caused by only the non-thermal motion. It may be possible to leverage this concept to isolate contrast generated by cavitation.

## 2.5 Histotripsy and IVIM Imaging

The collapse phase of the histotripsy therapy cloud may cause sufficient incoherent motion of the water molecules that the MR signal will be attenuated in an IVIM image. This attenuation may be separable from attenuation caused by diffusion and perfusion by using motion-encoding gradient waveforms with small values for  $b$ .

Further, the incoherent motions of water molecules induced by cavitation may be different from the motions that characterize thermal diffusion. Therefore, IVIM images of a cavitation event with gradient waveforms that have identical  $b$  values but vary in shape and amplitude may yield different signal attenuation factors.

IVIM at the therapy site may also be caused by the mechanisms of acoustic streaming and acoustic radiation forces. Their contributions to IVIM may be separated from the contribution made by cavitation by repeatedly imaging the cavitation site while increasing the amplitude of the acoustic pulses. The signal attenuation caused by streaming and radiation forces should continuously increase with pulse amplitude. The signal attenuation caused by cavitation should only be observable when the peak negative pressure of the acoustic pulse exceeds the cavitation threshold pressure.

If, during an IVIM sequence, the motions of the water molecules have already returned to thermal equilibrium by the start of the first encoding gradient, the resulting image may not capture signal contrast specific to cavitation. Instead, it will only capture attenuation caused by other incoherent processes. It may be possible, by controlling the relative timing between a cavitation event and the IVIM gradients, to control the appearance of signal attenuation on the resulting image.

In the following, we investigate the dependence of the attenuation factor on the peak negative pressure of the acoustic pulses as well as the amplitudes and separation times of the IVIM gradient pairs. We also investigate the dependence of the attenuation factor on the timing between a cavitation event and the start of the IVIM gradients. We do so either by inserting bipolar gradient lobes into a standard GRE spin-warp sequence one direction at a time, or by placing the cavitation events some time before or after the spin-warp sequence's imaging gradients (which also act as IVIM-encoding gradients). We then construct an imaging sequence to alternately enhance or minimize IVIM attenuation during MR-guided therapy of an *ex vivo* liver sample.

We find that signal attenuation in water is observed only when the peak negative pressures of the acoustic pulses exceed 24 MPa and that the magnitude of attenuation depends upon the amplitudes and separation times of the IVIM-encoding gradients. The magnitude of attenuation is found to be isotropic with IVIM encoding direction and varies strongly with the relative timing between the cavitation event and a bipolar IVIM-encoding gradient waveform. Pulse sequences with b-values on the order of  $0.04 \text{ s/mm}^2$  have sufficient sensitivity to IVIM for cavitation to induce greater than 10% signal reduction. In the *ex vivo* tissue sample, images with varied sensitivity to cavitation can be combined to form a precise image of the cavitation site.

## 2.6 Methods

All experiments were conducted using an MR-compatible focused transducer attached to a water bath (Fig. 2.1). Experiments A-D were performed in tap water and experiment E was performed in excised porcine liver. The details of the ultrasound therapy and MR imaging are given below.

### 2.6.1 Cavitation Generation

Cavitation was stimulated using an MR-safe, spherically focused array of 7 circular, ceramic, piezoelectric elements with a diameter of 2 cm each and a resonant frequency of 1 MHz. The elements were arranged confocally along the portion of a spherical surface with a 4.5 cm radius that is subtended by 4.8 steradians. The overall circular aperture of the transducer is 8.5 cm. See Fig. (2.1A)

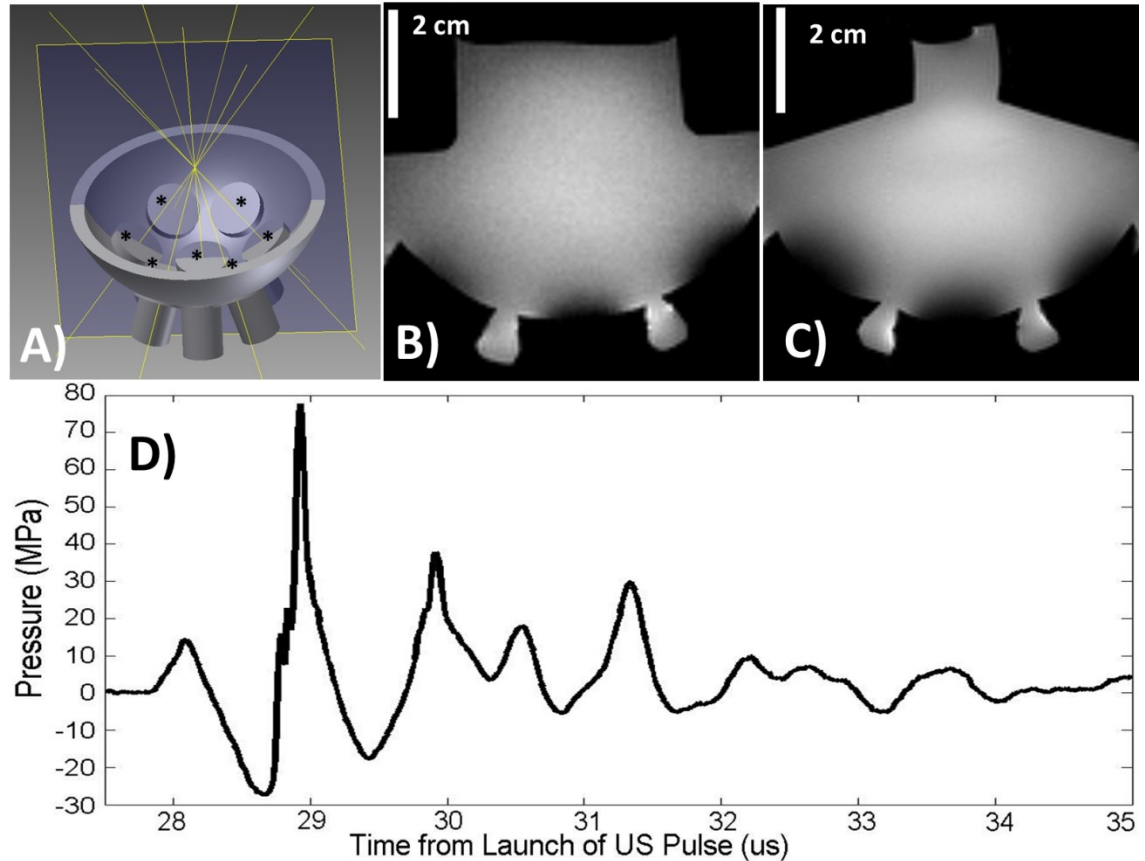


**Figure 2.1: Experimental setup. (A)** The acoustic pulses emitted from the piezoelectric elements (\*) converge at the focus (yellow lines). The imaging plane transects the focus and the transducer (blue surface). Two different water baths can be attached to the transducer to keep the beam path submerged in water. A spin-echo image of the larger water bath is shown in (B). The smaller-necked water bath is shown in (C). A trigger pulse can be sent from the MR pulse controller to the US amplifier at various times during an imaging sequence as chosen by the operator. (D) The acoustic waveform at the focus generated with maximum driving voltage as estimated by summing together the outputs of the individual elements.

The transducer was connected to an amplifier constructed by our lab that is able to deliver high-voltage, short duration pulses to the transducer elements. The amplifier was controlled by a programmable trigger pulse from the MR system console. Once triggered by the console, the amplifier and transducer setup launched a single acoustic ultrasound pulse,

which arrived at the transducer focus approximately 28  $\mu$ s later. Increasing the voltage across the amplifier resulted in increasing the peak negative pressure of the acoustic waveform.

Two water baths were constructed to keep the ultrasound beam path immersed. Each water bath had a different size neck in order to support different transmit/receive coils. The water bath was attached to the transducer housing in such a way that the transducer could be placed on the table of the MR scanner with the transmitting surface facing up. Once attached, the water-bath volume was filled with tap water. See Fig. (2.1 B-C).

The acoustic output at the transducer focus was estimated using a fiber-optic hydrophone [27] (33). Since cavitation disrupts the accuracy of the hydrophone, the amplifier excited each transducer element individually with incrementing driving voltage. The combined acoustic output of the transducer was then estimated by summing together the acoustic outputs of the individual elements. The estimated combined output of the transducer at the maximum driving voltage is shown in Fig. (2.1 D) and has a peak negative pressure of 27.5 MPa. This driving voltage was subsequently used for all experiments where cavitation was desired.

Prior to the start of the experiments, cavitation was confirmed to occur in both water and tissue using an ultrasound imaging probe. With the voltage across the amplifier set to maximum, trigger pulses sent to the amplifier caused a temporally-variable, hyperechoic region in the ultrasound images. Cavitation was assumed to continue to occur when ultrasound probe was removed and the water or tissue sample was placed inside the scanner.

For control experiments, where cavitation was not desired, the amplifier voltage was reduced by half and the estimated peak negative pressure of the resulting acoustic pulse was 15.2 MPa. At these pressures, a hyperechoic region on the ultrasound images was never observed for every trigger pulse sent to the amplifier.

### **2.6.2 MR Images**

Unless otherwise stated, all IVIM images were acquired on a 7T/310 small animal scanner (Agilent Technologies, Walnut Creek , CA) using a 14 cm diameter, dual-channel, birdcage coil. The following parameters were used: TE/TR = 10/2500 ms, FOV = 55x55x1 mm, Matrix = 128x128x1, Bandwidth = 50 kHz, flip angle = 90°, NEX = 1. Images were

acquired in the axial plane with the phase encode direction displayed as the up/down direction of the image. The therapy transducer was pulsed only once per TR. Thus, a 128-shot GRE imaging sequence delivered 128 ultrasound pulses to the target over the duration of the sequence. Long repetition times were used decouple any effects caused by concatenated pulses and reduce through-plane motion effects.

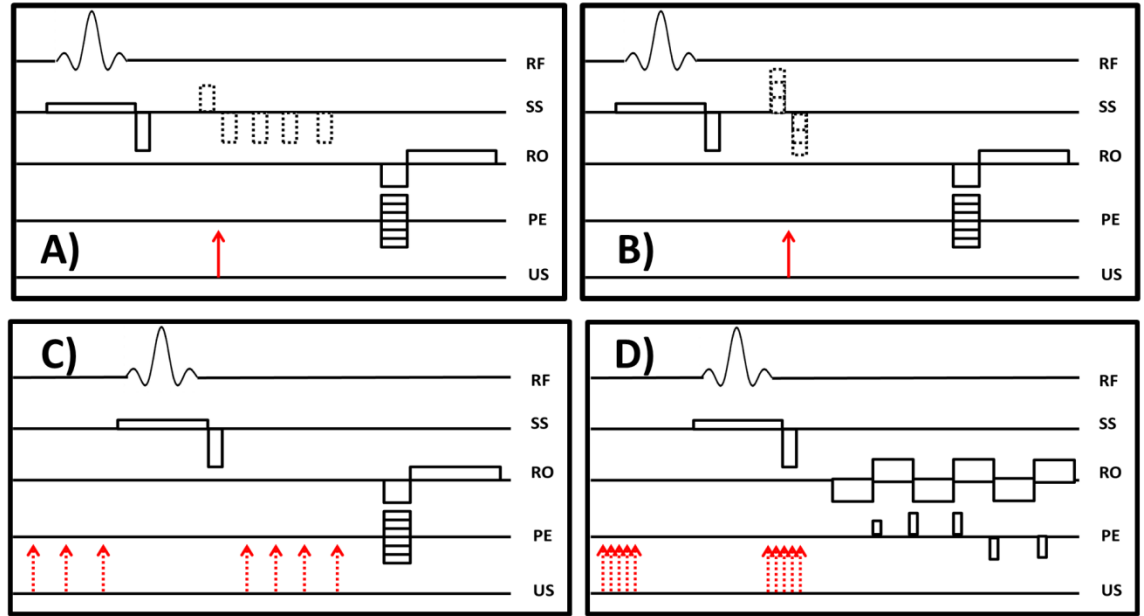


**Figure 2.2: Schematic of pulse sequences used: (A) GRE, spin-warp, IVIM sequence used in experiments A, B.1, and C. The cavitation event occurs just after the first IVIM gradient lobe (red arrow) while separation time is incremented. (B) GRE, spin-warp, IVIM sequence used in experiment B.2. The separation time between the IVIM gradients is held constant while the amplitude is incremented. (C) GRE, spin-warp pulse sequence used in experiment D. The ultrasound pulse is fired at different times before signal acquisition (red arrows). (D) GRE EPI sequence used in experiment E. Ultrasound pulses are either fired 10 ms before RF acquisition to desensitize the sequence to cavitation IVIM, or fired between the slice-select and slice-rewind gradient lobes to sensitize the sequence to cavitation IVIM. Each instance/increment is shown as a dotted line for clarity. Amplitudes and time gaps are not to scale. Abbreviations are: RF=radio frequency, SS=slice select, RO=readout, PE=phase encode, US=ultrasound.**

### 2.6.3 Experiment A: Dependence on Ultrasound Pulse Amplitude

An experiment was performed to determine the dependence of IVIM based signal attenuation on the amplitude of the ultrasound pulse. Tap water at the focus of the transducer was repeatedly imaged by identical IVIM sequences while the voltage across the transducer amplifier was incremented. The voltage increments corresponded to peak negative pressures of 9.0, 11.0, 14.0, 15.1, 16.3, 18.8, 21.3, 23.4, 24.6, 24.5, 25.2, 25.8, and 27.5 MPa. A control image was also acquired with the amplifier turned off.

The IVIM sequence consisted of a GRE spin warp sequence with a balanced, bipolar gradient pair inserted between RF excitation and the readout gradient and oriented along the slice-select direction. Immediately after completion of the first IVIM gradient lobe, a trigger pulse was sent from the MR console to the transducer amplifier. The duration of each IVIM gradient lobe was 1 ms. The amplitude of the IVIM gradient was  $3.5 \text{ Gcm}^{-1}$  and the separation time between the two lobes was 3.5 ms. Images were acquired with the smaller-necked cap and a 1.5 cm diameter surface coil centered about the cavitation site. FOV =  $30 \times 30 \times 1 \text{ mm}$ . See Fig. (2.2A).

#### **2.6.4 Experiment B: Dependence on the IVIM Gradient Waveform**

Two experiments were conducted to determine how signal attenuation at the cavitation site varies with the amplitudes and mixing time of an IVIM-encoding gradient waveform. For both experiments, a balanced, bipolar gradient pair was inserted between the RF excitation and readout portions of a GRE spin warp sequence. These IVIM gradients were oriented along the slice select direction. Immediately after completion of the first IVIM gradient lobe, a trigger pulse was sent from the MR console to the transducer amplifier. The duration of each IVIM gradient lobe was 1 ms.

The first experiment acquired 8 images of tap water at the transducer focus with the IVIM-encoding gradient amplitudes set to  $3.4 \text{ Gcm}^{-1}$ . The separation between the two IVIM gradient lobes was varied from 0 to 3.5 ms in 0.5 ms increments. See Fig. (2.2A).

The second experiment acquired 21 images with the IVIM-encoding gradient amplitudes varying from 0 to  $9.5 \text{ Gcm}^{-1}$  in  $0.47 \text{ Gcm}^{-1}$  increments. The separation between the IVIM gradient pulses was kept to 10  $\mu\text{s}$  for all instances—just long enough to transmit a trigger pulse from the MR console to the ultrasound amplifier. See Fig. (2.2B).

#### **2.6.5 Experiment C: Directional Dependence**

The dependence of the attenuation factor on gradient direction was explored. Here, the same sequence used in both experiment A and the first part of experiment B was repeated 3 times with the IVIM-encoding gradients directed alternately along the slice-select, readout, and phase-encode directions. For each run, a total of 8 images of tap water at the transducer focus were acquired with the IVIM-encoding gradient amplitude set to  $3.5 \text{ Gcm}^{-1}$  while the mixing time was varied from 0 to 3.5 ms in 0.5 ms increments. A trigger pulse was



sent from the MR console to the transducer amplifier immediately after completion of the first IVIM encoding lobe. See Fig (2.2A)

Imaging was carried out with a 1.5 cm diameter surface coil centered about the cavitation site in order to boost the SNR. Imaging parameters were FOV = 30x30x1 mm, Matrix = 64x64x1.

#### **2.6.6 Experiment D: Dependence on Timing Relative to IVIM-encoding Gradients**

In order to explore how the signal attenuation at the cavitation site depends upon the relative timing between a cavitation event and the imaging gradients, GRE spin warp images of tap water at the transducer focus were acquired while placing the cavitation event at different times relative to the RF pulse. See Fig. (2.2C).

The trigger timings used were composed of 12 one-millisecond increments ranging from 11.1 to 0.1 ms before the center of the RF excitation pulse, and 12 half-millisecond increments ranging from 2.3 to 7.8 ms after the center of the RF excitation pulse. Gradient parameters are: slice-select/rewind amplitude = 3.2/4.0 Gcm<sup>-1</sup>; slice select/rewind duration = 2.1/0.9 ms; readout/rewind amplitude = 2.1/4.0 Gcm<sup>-1</sup>; readout/rewind duration = 2.6/0.8 ms. The slice-select and readout gradient pairs had b-values of 0.06 and 0.05 smm<sup>-2</sup> respectively.

#### **2.6.7 Experiment E: *Ex Vivo* Tissue Sample**

The ability to control cavitation induced IVIM contrast in a therapy setting was examined by simultaneously scanning and treating an excised tissue sample. To demonstrate that fast imaging sequences can be used to detect cavitation-based IVIM contrast, a GR-EPI sequence was used instead of a spin-warp sequence.

A porcine liver sample was suspended in the smaller water bath. The 1.5 cm diameter surface coil was placed around the water bath neck and centered about the cavitation site. After applying 5000 ultrasound pulses to the liver tissue, the therapy site was scanned twice by the EPI sequence. During scanning, 10 cavitation pulses were triggered by the scanner console. These pulses were placed either 10 ms before the start of the slice-select gradient, or between the slice-select and slice-rewind gradient lobes. See Fig. (2.2D).

Each trigger pulse was spaced apart by 0.2 ms. The sequence imaged the same plane as experiments A-D. Imaging parameters: TE/TR: 7/1000 ms, FOV = 33x33x1mm, Matrix

= 96x96x1, Bandwidth = 208 kHz, flip angle = 70°, NEX = 1, Segments = 12. A reference echo for each segment was acquired for each image. This made for a total of 24 shots and 24 ultrasound pulses per image.

### 2.6.8 Control Images

The above experiments were repeated with the voltage across the US amplifier turned down to below the cavitation threshold (estimated peak negative pressure: 15.2 MPa).

### 2.6.9 Data processing

The attenuation factor,  $F$ , of each image was estimated by selecting a region of interest (ROI) within the area of attenuated signal and averaging the intensity of the pixels within this ROI. This result was then divided by the average signal intensity of the pixels within the same ROI when applied to the corresponding control image. An example ROI is shown in Fig. (2.3).

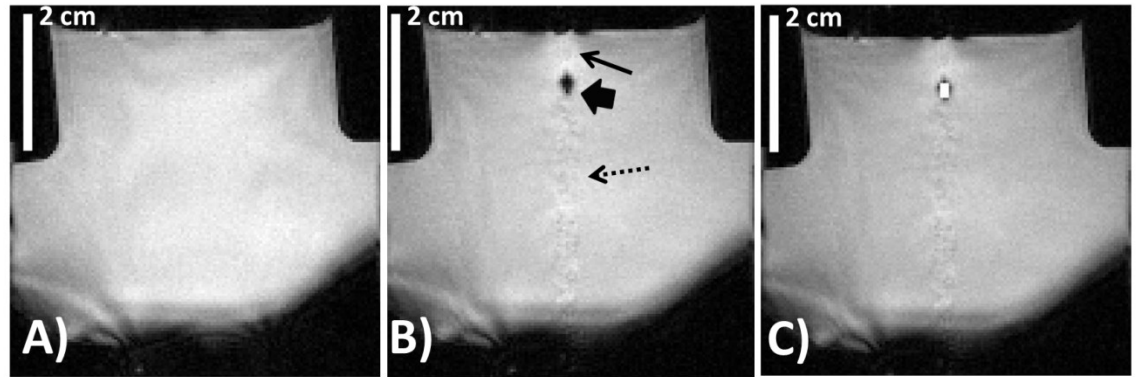


**Figure 2.3: (A) Gradient echo image acquired with the sequence shown in Fig. (2.A) and with the voltage across the US amplifier set below the cavitation threshold. (B) Image acquired by the same sequence but with the voltage across the US amplifier set above the cavitation threshold. Attenuation factor: 0.25; bvalue: 0.47  $\text{smm}^{-2}$ . The cavitation event causes localized attenuation of signal magnitude (block arrow). Additionally, the cavitation event causes signal enhancement due to through-plane motion (solid arrow) as well as ghosting (dotted arrow) along the phase-encode direction (up/down). (C) The same image as in (B) but with the ROI used for calculations highlighted as bright pixels.**

## 2.7 Results

An example of images of the transducer, water bath, cavitation-induced artifacts, and ROI selection are shown in Fig. (2.3). The image shown in Fig (2.3.B) indicates a signal void created by the presence of a cavitation bubble (thick solid arrow), has an attenuation factor

of 0.25, and is taken from the first part of experiment B with a gradient separation time of 3.5 ms.

The image in Fig. (2.3.B) also displays ghosting along the phase encoding direction (up/down) and some signal enhancement near the attenuation site (dotted and narrow, solid arrows, respectively). We observed that these artifacts remained consistent across all imaging experiments where the voltage across the US amplifier was above the cavitation threshold. The ghosting artifact is caused by random variations in the shape and evolution of the bubble cloud between shots. The signal enhancement artifact is thought to be caused by through-plane motion of the water molecules between shots. Its intensity was found to reduce with both increased slice thickness and increased TR. These artifacts were also not visible in any of the control images.

An example ROI used to calculate the attenuation factor is shown in Fig (2.3.C).

### 2.7.1 A: Dependence on Ultrasound Pulse Amplitude

The attenuation factors estimated while varying the amplitude of the ultrasound pulse are plotted as a function of peak negative pressure in Fig. (2.4). As the negative pressure phase of the ultrasound pulse increases in magnitude, the attenuation factor remains near unity until 24 MPa, where it quickly decreases with increasing peak negative pressure of the acoustic pulse.

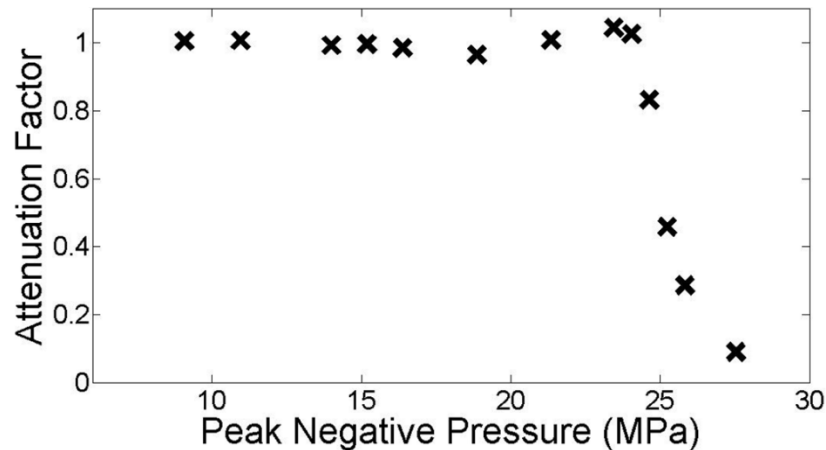


**Figure 2.4: Results corresponding to experiment A. The attenuation factors found at the cavitation site for various applied acoustic pulses are plotted vs. the peak negative pressure of those acoustic pulses. The attenuation factor remains near unity until the peak negative pressure of the ultrasound pulse approaches 24 MPa, where it decreases dramatically with increased peak negative**

pressure. This threshold pressure matches up with previous studies of cavitation in unfiltered tap water.

### 2.7.2 B: Dependence on the IVIM Waveform

The estimated attenuation factors measured from the experiments changing the IVIM gradient amplitudes and mixing time are plotted as a function of  $b$ -value in Fig. (2.5.A).

As shown in the figure, the amount of attenuation increases as the sequence is further sensitized to incoherent motion. However, the variation of the attenuation factor depends upon how the IVIM gradients were altered. Changes in the mixing time seem to cause a greater effect on the attenuation factor than changes in the gradient amplitudes. Both curves seem to follow an exponential decay pattern typical of pseudo-random flow in IVIM imaging, but with different decay rates. The jumps in the decay curve for the gradient amplitude varying experiment correspond to images with intrashot motion artifact.

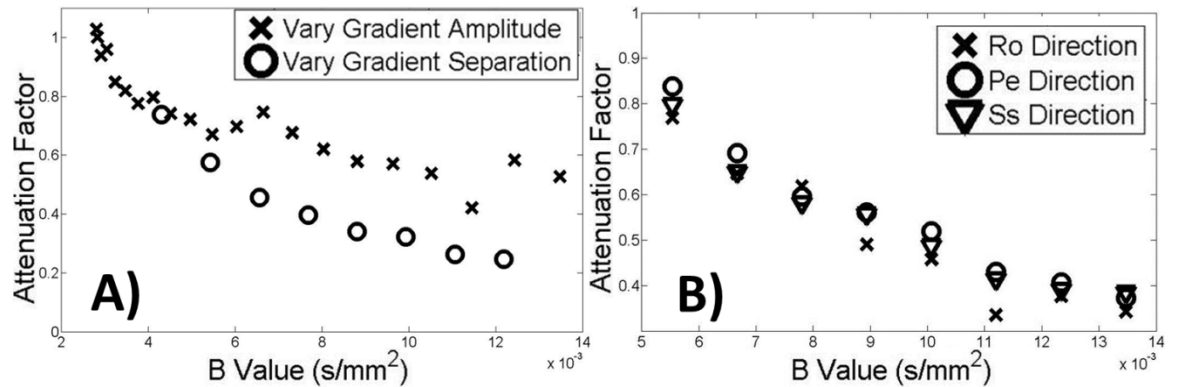


**Figure 2.5: Results corresponding to experiments B-C. (A) The attenuation factor at the cavitation site estimated from experiment B is plotted vs. the  $b$  value of the IVIM-encoding gradients. MR signal attenuation is greater when motion is sensitized by separating the gradient lobes (X) than by increasing the gradient strength (O) even for experiments with equivalent  $b$ -values. (B) The attenuation factors found at the cavitation site for experiment C are plotted vs. the  $b$  value of the IVIM-encoding gradients. The IVIM-encoding gradients were played along the readout (X), phase-encode (O), and slice-select ( $\Delta$ ) directions. The  $b$  value was increased by incrementing the mixing time between IVIM gradient lobes. The behavior of the attenuation factor is isotropic with gradient direction. Note that these  $b$ -values are extremely small, which suggests a very large amount of IVIM compared to thermal diffusion and tissue perfusion processes.**

### 2.7.3 C: Dependence on Direction.

The estimated attenuation factors measured in response to different directions of the encoding gradients are displayed in Fig. (2.5.B). As in the previous experiment, the attenuation factor decreases monotonically with increased  $b$  value of the gradient waveforms. Further, the signal attenuation has an isotropic response to gradient direction.

Example magnitude and phase images of the directionality experiment are displayed in Fig (2.6). These images were acquired with the IVIM gradients at maximum sensitivity to motion (3.5 ms separation time,  $0.53 \text{ smm}^{-2}$  b value) and generated along the phase encode direction (up/down). The IVIM motion causes noticeable attenuation at the focal zone (attenuation factor = 0.32) and a opposite changes in phase localized around the cavitation site. A large amount of phase also accrues at the top of the object due to an air bubble.

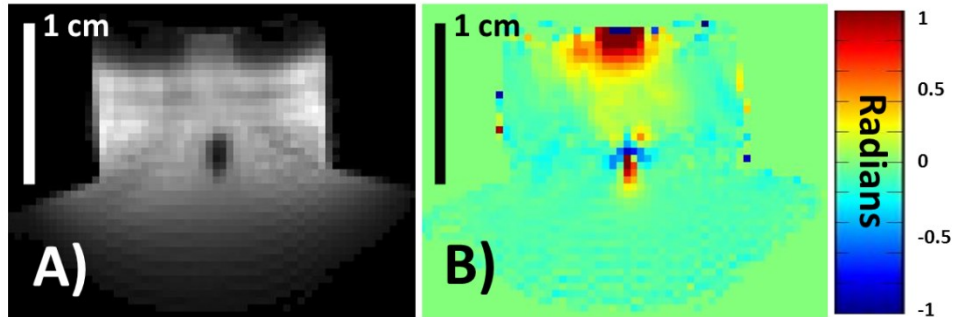


**Figure 2.6: Example (A) magnitude and (B) phase image from the results of experiment C. For this image, separation time=3.5 ms; b value =  $0.53 \text{ smm}^{-2}$ ; attenuation factor=0.32. The IVIM gradients are applied along the phase encode direction (up/down). Water above and below the cavitation site accrue opposite phases and may be due to coherent flow patterns induced by cavitation.**

#### 2.7.4 D: Dependence on Cavitation and IVIM Gradient Timing

The attenuation factors estimated while varying the timing of the trigger pulses are plotted in Fig. (2.7). In this figure, time relative to the center of the RF pulse (sinc shape) is plotted along the  $x$ -axis while the attenuation factor is plotted along the  $y$ -axis. Each asterisk marks the attenuation factor observed when an ultrasound pulse is programmed to occur at the corresponding time on the  $x$ -axis.

As shown in the figure, the estimated attenuation factor decreases as the cavitation event approaches either the slice select or readout gradient pairs. Further, cavitation events that occur immediately after the slice select pair do not display appreciable signal attenuation. The slice select and readout gradients appear to cause equal amounts of signal attenuation.

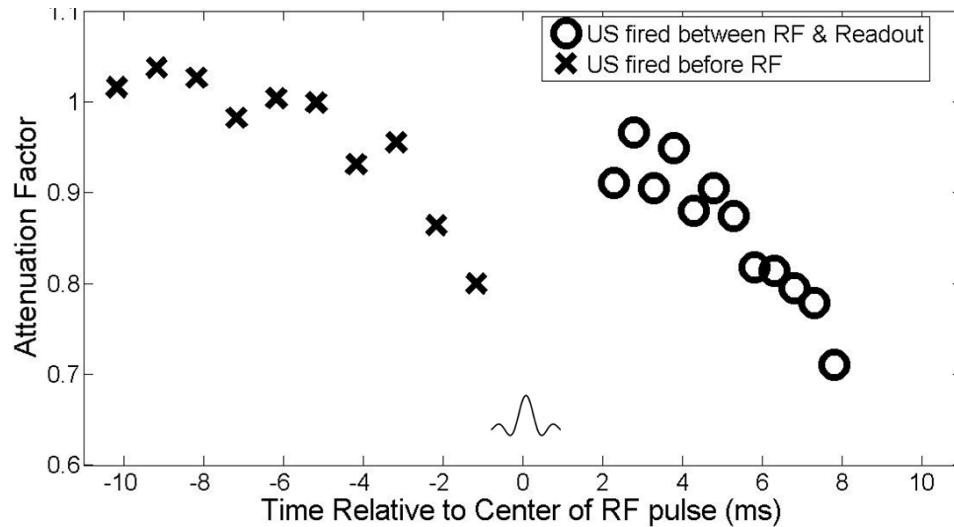


**Figure 2.7: Results corresponding to experiment D. The attenuation factor is plotted as a function of the time (in ms) between the US pulse and the RF excitation pulse. The small sinc shape represents the time taken up by the RF pulse. The MR signal is most attenuated when the cavitation event occurs just before either the slice-select or the readout gradient pulses.**

### 2.7.5 E: *Ex Vivo* Tissue Sample

The separability of cavitation based IVIM contrast is demonstrated in Fig (2.8). High-resolution GRE EPI images of the liver sample are shown in frames (A-B). In frame (A), ten ultrasound pulses are applied 10 ms before the start of the slice-select gradient. In frame (B), ten ultrasound pulses are applied between the slice-select and slice-rewind gradients. The region of  $T_2^*$  enhanced contrast indicated by the arrow in frame (A) specifies homogenized liver tissue. The localized signal attenuation indicated by the arrow in frame (B) specifies cavitation-induced IVIM contrast. The pixel-by-pixel subtraction of the two images is shown in frame (C). In this manner, cavitation induced contrast can be isolated from other image features.

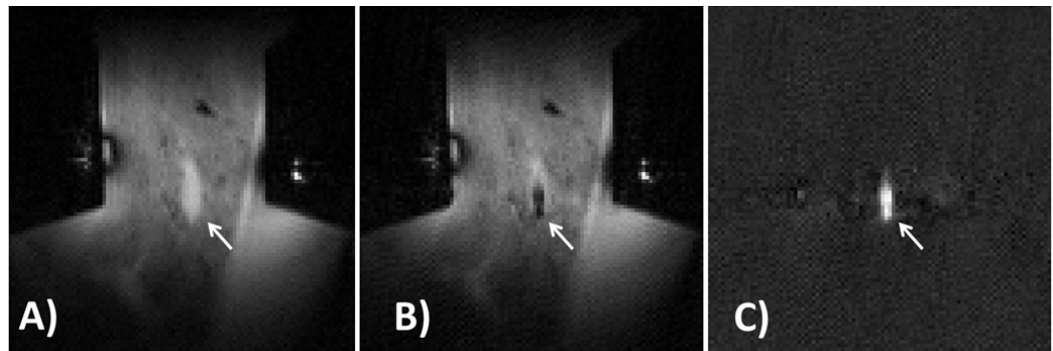


**Figure 2.8: Results corresponding to experiment D. EPI images acquired during therapy with (A) ultrasound pulses fired 10 ms before the start of the slice select gradient and (B) ultrasound pulses fired between the slice-select and slice-rewind gradients. A  $T_2^*$  enhanced lesion is apparent in**

**(A) at the therapy focus. Localized attenuation from a cavitation cloud is shown in (B). The pixel-wise subtraction image between (A) and (B) is shown in (C). In this manner, the attenuation caused by cavitation can be isolated from other image features and incoherent motion processes.**

## 2.8 Discussion

### 2.8.1 Cavitation

The results shown in Fig. (2.4) corroborate well with cavitation theory. In the figure, the attenuation factor decreases dramatically when the peak negative pressure of the acoustic pulse transitions from 24.6 to 27.5 MPa. Meanwhile, reference [13] reports that the probability of 5  $\mu$ s acoustic pulses in unfiltered water to successfully induce cavitation increases from 0 to 1 as the peak negative pressure of each pulse increases through a nearly identical range of 24 to 28 MPa. In contrast, acoustic streaming and acoustic radiation force are reported to increase smoothly with increasing acoustic power [22], [24]. The threshold behavior in Fig. (2.4), suggests that cavitation makes the primary contribution to the localized signal attenuation observed in these experiments.

### 2.8.2 Effect of Susceptibility Gradients

The sparse distributions of bubbles that linger after a cavitation event appear to have a very small effect on the attenuation factor at the cavitation site. In the literature, theoretical [6] and experimental work [5], [7], [8] has shown that the introduction of microbubbles to water reduces the transverse relaxation rate,  $R_2^*$ , of water proportionally to the volume fraction of the bubbles. At 7 Tesla, this proportionality constant ranges, for  $\sim 5 \mu$ m diameter microbubbles, from  $42.38 \text{ s}^{-1}$  [8] to  $58.52 \text{ s}^{-1}$  [5], depending on the composition of the bubbles. In the case of histotripsy, if the bubble distribution that persists after collapse of the cavitation cloud has a volume fraction of 1%, the attenuation factor in Fig. (2.7) should display a change in  $R_2^*$  decay rate of  $\sim 40\text{-}50 \text{ s}^{-1}$ . However, such large changes in the transverse relaxation rate are not apparent in Fig. (2.7). The attenuation factor does not decrease with increasing time separating the formation of the residual cloud and readout. Therefore, the volume fraction of this residual cloud should be much smaller than 1%.

It is possible, however, that the cavitation cloud itself may be sufficient to induce some susceptibility effect on the cavitation site. In this case, due to its short duration, a cavitation event should introduce some constant signal attenuation factor to the data points in Fig. (2.7). This constant attenuation, if present, appears to be buried in the noise.

### 2.8.3 The Effects of Fluid Motion

The attenuation factor at the therapy focus correlates strongly with changes made to the IVIM-encoding gradients. Further, the rate at which the attenuation factor changes depends on how the IVIM-encoding gradients are modified. Experiments where the mixing time between the gradient pairs was lengthened exhibit more signal attenuation than experiments where the amplitudes of the gradient lobes were increased. If flow induced by cavitation was similar to thermal diffusion, these attenuation factors should be identical for gradients with identical  $b$  values.

As shown in Fig. (2.5.B), the attenuation caused by cavitation is isotropic with gradient direction. This suggests that any gradient direction can be used to capture cavitation-based IVIM contrast.

The phase image displayed in Fig. (2.6) shows that water on opposite sides of the cavitation site accrue opposite phases. One possible explanation for this result is that the collapse phase of the cavitation cycle occurs more slowly than the expansion phase. Water molecules may have more time to generate excess phase during the collapse portion of the cavitation cycle than during the expansion portion. If the expansion and collapse portions occurred at equal rates, then the excess phases would negate each other. In future work, phase contrast MRI may be a useful tool to study cavitation-induced flows in opaque media.

The  $b$  values of the IVIM-encoding gradients used in experiments A-C are on the same order as those of standard imaging gradient pairs. This finding corroborates the results shown in Fig. (2.7). In this figure, the attenuation factor decreases as the cavitation event approaches the start of either imaging gradient pair. This suggests that standard imaging gradients can sensitize an image to cavitation.

Additionally, the results in Fig. (2.7) show that cavitation events that occur more than 5 ms before a gradient pair do not cause significant signal attenuation. We suspect a standard imaging sequence can be made either sensitive or insensitive to cavitation by controlling the proximity of the cavitation event to the imaging gradients.



#### 2.8.4 Therapy Feedback in Tissue

The images displayed in Fig. (2.8) demonstrate that sensitivity to cavitation can be controlled by changing the relative timing between the cavitation events and the imaging gradients. The images acquired where the ultrasound pulses are fired immediately after the slice select gradient display localized attenuation. Meanwhile, images acquired when the ultrasound pulses are fired 10 ms before the slice-select gradient do not display cavitation-specific contrast. A subtraction between these two images yields a precise image of the cavitation site.

Of note, more pulses (10 per TR) were needed to achieve this attenuation than needed in water (1 per TR). This is likely because the cavitation threshold in tissue is higher than in water. Reference [13] reports that the probability of cavitation in kidney begins to transition near 27 MPa.

Additionally, these images were acquired during the course of therapy (~5000 pulses) rather than at its onset. This is because it was difficult to obtain images with cavitation contrast at the beginning of therapy. Signal attenuation became observable only after many ultrasound pulses were applied to the tissue.

One explanation for this behavior is that, at the onset of therapy, neither cavitation nor acoustic streaming can mix about water that is bound up into intact tissue and cavitation-based contrast can only be observed in liquid or semi-liquid media. A second explanation is that the cavitation cloud produced at the onset of therapy is very small due to the higher cavitation threshold in intact tissue and the relatively weak negative pressure of our transducer. A more powerful transducer should then be able to produce IVIM contrast at the onset of therapy. Currently, we are unable to either increase the peak negative pressure of the transducer or independently measure the size of the cavitation cloud during therapy while performing MR imaging. Future work that accomplishes these tasks may be able to determine which explanation is accurate.

We note that signal attenuation caused by cavitation occurs when the peak negative pressure of the acoustic pulse surpasses 24 MPa. This attenuation increases with increased sensitivity of IVIM-encoding gradient pairs. Further, in order to capture IVIM-induced signal attenuation, the cavitation event must occur such that the water motion has not returned to thermal equilibrium by the beginning of the gradient sequence. Otherwise, the

sequence will be insensitive to cavitation-based IVIM. Cavitation-based signal attenuation has an isotropic response to the direction of the IVIM-encoding gradients. Lastly, we have shown that, in an *ex vivo* model, sequences can be made alternately sensitive and insensitive to the attenuation caused by cavitation by merely controlling the relative timing between the cavitation event and the imaging gradients.

## 2.9 Conclusion

In this study, we have examined the response of the MR signal of a GRE sequence to a cavitation event. Cavitation appears to cause a temporary increase in incoherent flow of the water molecules at the cavitation site. When scanned by a sequence with a motion-sensitizing, balanced, field gradient, cavitation events exhibit localized signal attenuation in MR images. This sensitivity can be controlled by determining the placement of the cavitation events while imaging.

## 2.10 References

- [1] S. P. Allen, T. L. Hall, C. a Cain, and L. Hernandez-Garcia, “Controlling cavitation-based image contrast in focused ultrasound histotripsy surgery.,” *Magn. Reson. Med.*, vol. 00, no. November 2013, pp. 1–10, Jan. 2014.
- [2] S. P. Allen, T. L. Hall, C. A. Cain, and L. Hernandez, “MR-based targeting of histotripsy therapy at 7T,” in *Proceedings of the 21st Annual Meeting of ISMRM*, 2013, p. 1831.
- [3] H.-H. Peng, C.-H. Wu, S.-T. Kang, J.-W. Zhang, H.-L. Liu, W.-S. Chen, C.-H. Wang, and C.-K. Yeh, “Real-time monitoring of inertial cavitation effects of microbubbles by using MRI: In vitro experiments,” *Magn. Reson. Med.*, vol. 00, no. August, p. n/a–n/a, 2015.
- [4] A. L. Alexander, T. T. McCreery, T. R. Barrette, A. F. Gmitro, and E. C. Unger, “Microbubbles as novel pressure-sensitive MR contrast agents,” *Magn. Reson. Med.*, vol. 35, no. 6, pp. 801–806, 1996.
- [5] J. S. Cheung, A. M. Chow, H. Guo, and E. X. Wu, “Microbubbles as a novel contrast agent for brain MRI,” *Neuroimage*, vol. 46, no. 3, pp. 658–664, 2009.
- [6] R. Dharmakumar, D. B. Plewes, and G. A. Wright, “On the parameters affecting the

- sensitivity of MR measures of pressure with microbubbles,” *Magn. Reson. Med.*, vol. 47, no. 2, pp. 264–273, 2002.
- [7] T. Ueguchi, Y. Tanaka, S. Hamada, R. Kawamoto, Y. Ogata, M. Matsumoto, H. Nakamura, and T. Johkoh, “Air microbubbles as MR susceptibility contrast agent at 1.5 tesla,” *Magn. Reson. Med. Sci.*, vol. 5, no. 3, pp. 147–150, 2006.
- [8] K. K. Wong, I. Huang, Y. R. Kim, H. Tang, E. S. Yang, K. K. Kwong, and E. X. Wu, “In vivo study of microbubbles as an MR susceptibility contrast agent,” *Magn. Reson. Med.*, vol. 52, no. 3, pp. 445–452, 2004.
- [9] K. Hynynen, N. McDannold, N. Vykhodtseva, and F. A. Jolesz, “Noninvasive MR imaging-guided focal opening of the blood-brain barrier in rabbits,” *Radiology*, vol. 220, pp. 640–646, 2001.
- [10] K. Hynynen, N. McDannold, N. A. Sheikov, F. A. Jolesz, and N. Vykhodtseva, “Local and reversible blood–brain barrier disruption by noninvasive focused ultrasound at frequencies suitable for trans-skull sonications,” *Neuroimage*, vol. 24, no. 1, pp. 12–20, 2005.
- [11] K. Hynynen, “MRIgHIFU: A tool for image-guided therapeutics,” *J. Magn. Reson. Imaging*, vol. 34, no. 3, pp. 482–493, 2011.
- [12] A. D. Maxwell, T. Y. Wang, C. A. Cain, J. B. Fowlkes, O. A. Sapozhnikov, M. R. Bailey, and Z. Xu, “Cavitation clouds created by shock scattering from bubbles during histotripsy,” *J. Acoust. Soc. Am.*, vol. 130, no. 4, pp. 1888–1898, 2011.
- [13] A. D. Maxwell, C. A. Cain, T. L. Hall, J. B. Fowlkes, and Z. Xu, “Probability of cavitation for single ultrasound pulses applied to tissues and tissue-mimicking materials,” *Ultrasound Med. Biol.*, vol. 39, no. 3, pp. 449–465, 2013.
- [14] Z. Xu, T. L. Hall, J. B. Fowlkes, and C. A. Cain, “Optical and acoustic monitoring of bubble cloud dynamics at a tissue-fluid interface in ultrasound tissue erosion,” *J. Acoust. Soc. Am.*, vol. 121, no. 4, pp. 2421–2430, 2007.
- [15] Z. Xu, M. Raghavan, T. L. Hall, M.-A. A. Mycek, J. B. Fowlkes, and C. A. Cain, “Evolution of bubble clouds induced by pulsed cavitation ultrasound therapy - Histotripsy,” *IEEE Trans. Ultrason. Ferroelectr. Freq. Control*, vol. 55, no. 5, pp. 1122–1132, 2008.

- [16] T. Y. Wang, Z. Xu, T. L. Hall, J. B. Fowlkes, and C. A. Cain, “An efficient treatment strategy for histotripsy by removing cavitation memory,” *Ultrasound Med. Biol.*, vol. 38, no. 5, pp. 753–766, 2012.
- [17] E. O. Stejskal and J. E. Tanner, “Spin diffusion measurements: spin echoes in the presence of a time-dependent field gradient,” *J. Chem. Phys.*, vol. 42, no. 1, pp. 288–292, 1965.
- [18] D. Le Bihan, E. Breton, D. Lallemand, P. Grenier, E. Cabanis, and M. Laval-Jeantet, “MR imaging of intravoxel incoherent motions: application to diffusion and perfusion in neurologic disorders,” *Radiology*, vol. 161, no. 2, pp. 401–407, 1986.
- [19] R. Muthupillai, P. J. Rossman, D. J. Lomas, J. F. Greenleaf, S. J. Riederer, and R. L. Ehman, “Magnetic resonance imaging of transverse acoustic strain waves,” *Magn. Reson. Med.*, vol. 36, no. 2, pp. 266–274, Aug. 1996.
- [20] T. Wu, J. P. Felmlee, J. F. Greenleaf, S. J. Riederer, and R. L. Ehman, “MR imaging of shear waves generated by focused ultrasound,” *Magn. Reson. Med.*, vol. 43, no. 1, pp. 111–115, 2000.
- [21] A. P. A. Sarvazyan, O. O. V Rudenko, S. D. Swanson, J. B. Fowlkes, and S. Y. Emelianov, “Shear wave elasticity imaging: a new ultrasonic technology of medical diagnostics,” *Ultrasound Med. Biol.*, vol. 24, no. 9, pp. 1419–1435, 1998.
- [22] N. McDannold and S. E. Maier, “Magnetic resonance acoustic radiation force imaging,” *Med. Phys.*, vol. 35, no. 8, pp. 3748–3758, 2008.
- [23] M. Radicke, A. Engelbertz, B. Habenstein, M. Lewerenz, O. Oehms, P. Trautner, B. Weber, S. Wrede, and K. Maier, “New image contrast method in magnetic resonance imaging via ultrasound,” *Hyperfine Interact.*, vol. 181, no. 1–3, pp. 21–26, 2008.
- [24] H. C. Starritt, C. L. Hoad, F. A. Duck, D. K. Nassiri, I. R. Summers, and W. Vennart, “Measurement of acoustic streaming using magnetic resonance,” *Ultrasound Med. Biol.*, vol. 26, no. 2, pp. 321–333, 2000.
- [25] D. Sinnaeve, “The Stejskal–Tanner equation generalized for any gradient shape—an overview of most pulse sequences measuring free diffusion,” *Concepts Magn. Reson. A.*, vol. 40A, no. 2, pp. 39–65, 2012.
- [26] D. Le Bihan, E. Breton, D. Lallemand, M. L. Aubin, J. Vignaud, and M. Laval-Jeantet,

“Separation of diffusion and perfusion in intravoxel incoherent motion MR imaging,”  
*Radiology*, vol. 168, no. 2, pp. 497–505, 1988.

- [27] J. E. Parsons, C. A. Cain, and J. B. Fowlkes, “Cost-effective assembly of a basic fiber-optic hydrophone for measurement of high-amplitude therapeutic ultrasound fields,”  
*J. Acoust. Soc. Am.*, vol. 119, no. 3, pp. 1432–1440, 2006.

# Chapter 3:

## MR Imaging of Individual Histotripsy Bubble Clouds.

A majority component of this chapter has been published in *Magnetic Resonance in Medicine* © 2015 Wiley Periodicals. Reprinted, with permission, from [1].

### 3.1 Introduction

The previous chapter introduced a novel MR imaging method to visualize the histotripsy bubble cloud. This chapter extends modifies this technique to be more useful for transcostal and transcranial surgeries. In both the transcostal and transcranial surgeries, histotripsy produces predictable, confined lesions with sharp borders, mainly because the size and location of bubble clouds formed by the ultrasonic pulses can be controlled even when the sound field is distorted by bone [2]–[4]. Further, these bubble clouds can be produced using ultrasound pulsing schemes with very low duty cycles, leading to negligible heating in soft tissues and bone [2].

For safety reasons, transcostal and transcranial histotripsy must be coupled with an imaging system capable of localizing histotripsy bubble clouds formed at the onset of therapy, prior to irreversible ablation. This allows the operator to terminate therapy should the bubble cloud be formed in a sensitive structure. Nominally, acoustic cavitation detection achieves this purpose [5]–[7]. However, in the transcostal and transcranial cases, acoustic cavitation detection cannot reconstruct the bubble cloud without making some correction for field aberrations imposed by the overlying bone [5], [8]. To this end, the patient, prior to therapy, submits to computed tomography [9] or ultra-short echo time MR imaging [10] to characterize her bone structure. Then, during therapy, the operator must rely on both these scans and a computational model to correct the cavitation detection signals [11]. The

additional cost, risk, and complexity of this step could be avoided by using an imaging method that can both be sensitized to the bubble cloud and produce accurate anatomical images without needing aberration correction.

Previous developments of MRI-based bubble detection for focused ultrasound surgeries have concentrated on either detecting cavity voids formed during boiling [12], [13] or detecting changes in  $T2^*$  [14]–[17]. These methods are unsuitable for monitoring histotripsy because they require the bubbles to persist through most of the acquisition time. Histotripsy bubble clouds have a lifespan of hundreds of microseconds and collapse too quickly to be directly picked up by even the fastest of MR sequences.

Recently, a magnetic resonance imaging technique has been developed to detect the incoherent water motion caused by inertial cavitation [18], [19]. This can be accomplished by synchronizing the ultrasound pulses with a bipolar, motion-encoding gradient. With the gradients in place, the water flow generated by cavitation disrupts the ability of the second gradient lobe to rewind linear phase imposed by the first gradient lobe. Images produced from these sequences show signal loss localized at the cavitation site. Though this method can easily detect bubble clouds made in free fluid and in tissue that has already been homogenized, it is uncertain if it can be used to detect histotripsy at the onset of therapy, where the intact tissue may inhibit both the expansion of the bubble cloud as well as subsequent water motion.

In the following paper, we assume that, when the distance between phase wraps introduced by the first lobe of the encoding gradient nears the size of the water perturbation made by the bubble cloud, the second gradient lobe is then unable to rewind the phase imposed by the first. This will result in signal loss localized to the cavitation site. Thus, very small bubble clouds can be visualized when the sensitizing gradients extend into regions of  $k$ -space with high spatial frequencies. Sequences where the gradients extend only into low spatial frequency regions will be unable to detect small bubble clouds.

We aim to demonstrate that MR pulse sequences with sensitizing gradients that extend into high  $k$ -space frequencies can capture the first bubble clouds formed inside a tissue target. Sequences that extend only into low frequency  $k$ -space will not be able to capture the first bubbles formed in a tissue target. For this investigation, we develop single-shot, line-scan and EPI imaging sequences that are sensitized to histotripsy. The

contribution of non-cavitation based fluid flow is investigated by using the line-scan sequence to estimate the cavitation pressure threshold in an agar phantom. We then use both sequences to monitor a series of bubble clouds formed in in-vitro porcine liver and brain samples.

## 3.2 Methods

### 3.2.1 Transducer

Our experiments were conducted using a custom-made, MR-compatible transducer placed in the bore of a 7T-310, small animal scanner (Agilent, Walnut Creek, CA) capable of gradients up to  $400 \text{ mT m}^{-1}$ . This transducer was composed of 16 focused elements, each with a center frequency of 500 kHz and arrayed along the surface of a sphere subtended by 1.84 steradians. The array had a focal depth of 56 mm and an aperture diameter of 115 mm. After construction, the transducer was calibrated using a fiber-optic hydrophone [20] using the same methods discussed in [21] and was found to generate peak negative pressures exceeding 28 MPa. The -6dB axial and longitudinal beam widths were found to be 2.1 mm and 7.0 mm. The acoustic pulses were  $4.5 \mu\text{s}$  long and contained roughly two full cycles. The driving system of this transducer was activated by the MR controller console using programmable trigger pulses.

One element in the transducer was wired as a send-receive hydrophone capable of recording acoustic emissions from cavitation activity. The voltage waveforms captured by this element were recorded by an oscilloscope (Pico Technology, Cambridgeshire, UK) and used for passive cavitation detection (PCD). In experiment (A) below, cavitation activity was determined by first subtracting an estimate of the reflections of the acoustic pulse off the transducer cap and then integrating the magnitude of the remaining backscatter signal over a period corresponding to 75 to 90  $\mu\text{s}$  after the acoustic pulse had been fired. This period corresponds to the time it takes for the acoustic pulse to travel to the focus and back. Details for this calculation are given under the section titled Experiment A. In experiment (B), cavitation activity was estimated by integrating the magnitude of the acquired PCD signal over the same period as in experiment (A).



The transducer was connected to a cap such that its cavity could be filled with degassed saline and coupled to a tissue sample placed at the transducer focus. A surface coil was then placed about the sample and centered on the cavitation site. See Fig. (3.1).

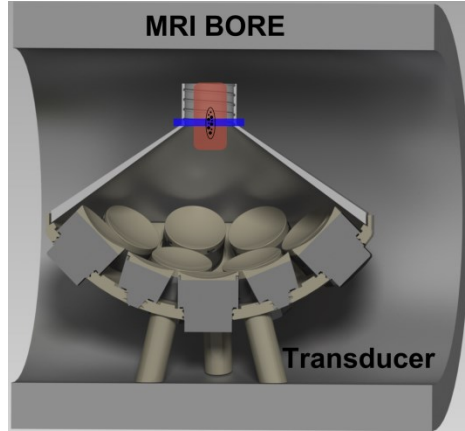


**Figure 3.1: Experimental setup used in this paper. A histotripsy transducer was placed in the bore of an MR scanner. A tissue sample (red, vertical rectangle) was placed at the transducer focus (ellipse). A surface coil was placed about the sample and used to monitor therapy by imaging a plane transecting the focus (blue, horizontal rectangle). The cavity between the elements of the transducer and the cap was filled with degassed saline solution.**

### 3.2.2 MRI Sequence

MR images were acquired using either a modified spin-echo, line-scan [22] sequence or an EPI sequence as shown in Fig. (3.2). In both the line-scan and the EPI sequence, a bipolar gradient was placed about a single ultrasound pulse such that one bubble cloud formed and collapsed between the gradient lobes. The time between the gradient lobes was limited to at most 1 ms. The durations of the acoustic pulse ( $\sim 5 \mu\text{s}$ ) and the lifecycle of the bubble cloud ( $\sim 200 \mu\text{s}$ ) were short enough to thoroughly mix water before the second gradient lobe rewound the phase imposed by the first. Repeating this sequence simultaneously applied consecutive histotripsy pulses to a target and acquired cavitation-sensitive images of each bubble cloud.

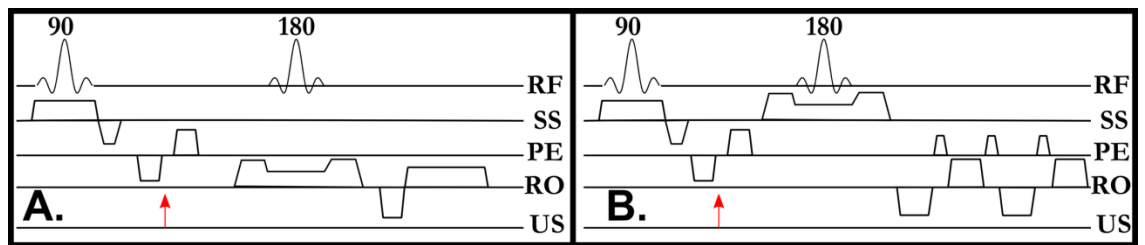


**Figure 3.2: Diagrams of histotripsy sensitized MR pulse sequences used in this study. A) 1-D, spin-echo, line-scan sequence. B) 2-D EPI sequence. Both sequences are sensitized to histotripsy by**

**synchronizing a bipolar gradient waveform with a single, 5  $\mu$ s histotripsy acoustic pulse (red arrow). Experiments were conducted by using these sequences to repeatedly image the transducer focus. Each new instance of the sequence would simultaneously apply and monitor an additional acoustic pulse to the target. Abbreviations: RF: Radio Frequency, SS: Slice Select, PE: Phase Encode, RO: Readout, US: Ultrasound.**

For the spin-echo, line-scan sequence, the slice-select gradient for the refocusing pulse was rotated to play along the phase-encode axis. As a result, the excitation planes intersected in a 1.5 mm rectangular beam that transected the transducer focus, parallel to the readout direction. The phase-encode gradient was also removed. Fourier transforming the resulting spin-echo yielded a single 1-D “image” of a column of tissue. Line-scanning allowed extremely fast sampling of the histotripsy process at the cost of losing spatial information in the phase encode direction.

Fig. (3.3) indicates how the refocusing pulse was ensured to transect the transducer focus. A sacrificial sample was placed in the transducer focus and imaged using a spin-echo sequence (Frame A). Then, a cavitation-sensitized 2D sequence [18] was used to plan the location of the rotated refocusing pulse (Frames B-C). In the resulting 1D images (Frame D), cavitation caused observable signal loss. The parameters used in this figure are TR = 1.2 s, TE = 65 ms, FOV = 25 x 25 mm, matrix = 125 x 125, bandwidth = 30.5 kHz, and NEX = 1. Sensitizing gradient amplitude, separation, and duration are identical to that used in experiment A.

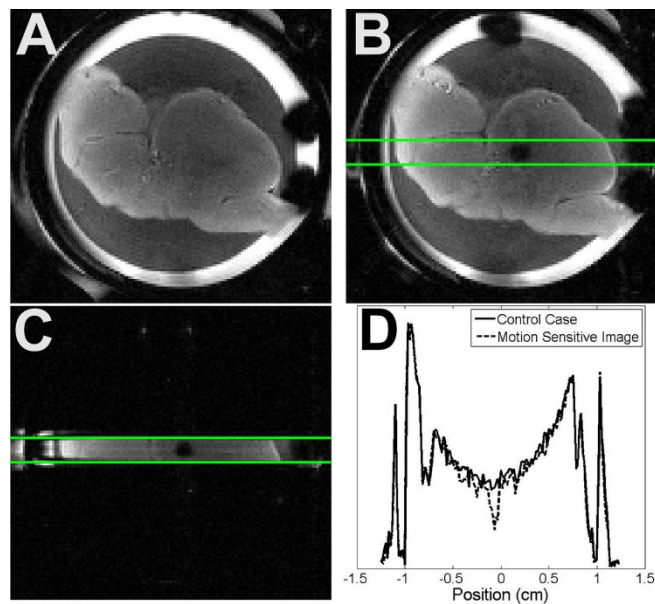


**Figure 3.3: Slice planning for the orthogonal excitation pulse. A) A sacrificial sample is placed in the transducer focus. B) A cavitation-sensitized 2D sequence was used to locate the focus**

**and plan the orthogonal refocusing plane (green lines). C) The refocusing slice is rotated to excited a column that transects the transducer focus. D) Resulting 1D line scans. The histotripsy bubble cloud creates localized signal loss that is easily detected when compared to the control case.**

Throughout the experiments described below, instances of the histotripsy imaging sequence were interleaved with an identical sequence but with the ultrasound system deactivated. For these cases, a bubble cloud did not form between the sensitizing gradients, resulting in images of the tissue target interleaved between every two acoustic pulses. These images were used as a control against which we could compare the signal loss caused by the bubble cloud.

The k-space frequency created by the sensitizing gradients of the MR sequence was controlled by increasing or decreasing the amplitude of the motion encoding gradients while keeping the duration of the lobes and the period between them constant.

For experiment (A), the imaging parameters for the line-scan sequence were TR = 1 s, TE = 41 ms, FOV = 25 x 1.5 x 1.5 mm, matrix = 125 x 1 x 1, bandwidth = 30.5 kHz, and NEX = 1. The sensitizing gradient lobes were each 2 ms long, separated by 1 ms and played at an amplitude of 117.8 mT m<sup>-1</sup>, leading to a b-value of 9.2 s mm<sup>-2</sup> and a k-space frequency of 100 cm<sup>-1</sup>.

For experiment (B), the imaging parameters for the line-scan sequence were: TR = 0.65 s, TE = 35 ms for the liver samples and TE = 50 ms for the brain samples, FOV = 25 x 1.5 x 1.5 mm, matrix = 75 x 1 x 1, bandwidth = 30.5 kHz and NEX = 1. The sensitizing gradient lobes were each 2.5 ms long and separated by 1 ms. While scanning six liver samples and six brain samples, the gradient amplitudes were set to 9 mT m<sup>-1</sup>, leading to a b-value of 0.1 s mm<sup>-2</sup> and a k-space frequency of 10 cm<sup>-1</sup>. While scanning another set of six liver and six brain samples, the amplitude was set to 376 mT m<sup>-1</sup>, leading to a b-value of 171 s mm<sup>-2</sup> and a k-space frequency of 400 cm<sup>-1</sup>.

Imaging parameters for the EPI sequence were TR = 0.7 s, TE = 26 ms, FOV = 25 x 25 x 1 mm, matrix = 64 x 64 x 1, bandwidth = 360 kHz, shots = 2, k-zero = 16, and NEX = 1. The sensitizing gradient lobes were each 4 ms long, separated by 0.5 ms, and played at an amplitude of 176 mT m<sup>-1</sup>, leading to a b-value of 113 s mm<sup>-2</sup> and a k-space frequency of 300 cm<sup>-1</sup>.

### 3.2.3 Experiment A: Determining the Cavitation Threshold

Though the MR sequences were created to observe histotripsy cavitation, it is possible other effects such as streaming and motion caused by the acoustic radiation force may contribute to signal loss at the transducer focus. In the following experiment, we attempted to isolate the contribution of these effects by using both the MR line-scan sequence as well as the PCD system to determine the cavitation threshold pressure in a phantom. If present, both radiation force based water flow and streaming would cause the MR-sequence to detect motion at pressures below the cavitation threshold, leading to a threshold estimate that is lower and less sharp than that determined by the PCD system.

Experiment A was performed by placing a 1.5 cm wide by 2.5 cm long cylinder of 1.25% agar gel (LabScientific, Catalog# AG-SP) into the transducer focus. Agar phantoms at this concentration have acoustic attenuation near that of water [23].

A small liquefied volume was first created within the gel matrix prior to experimentation by applying a pre-treatment of one thousand histotripsy pulses at 35 MPa estimated peak negative pressure such that the physical environment would be consistent throughout the experiment. After pre-treatment, the line-scan imaging sequence was used to apply and image 100 histotripsy pulses all with a common acoustic amplitude. This experiment was repeated 14 times while the acoustic output was ramped from 17 to 35 MPa at 14 discrete points.

The probability of stimulating a bubble cloud using an acoustic pulse with a given peak negative pressure was calculated by counting the fraction of pulses per acoustic amplitude where signal loss greater than a threshold value was observed. Signal loss was determined by dividing the signal at the focus in the histotripsy image by the signal at the focus in the corresponding control image. The baseline was determined by selecting a region of the phantom 2 mm away from the focus, where the signal appeared to remain constant over the entire experiment. The mean histotripsy image signal in this region was divided by the corresponding mean control image signal. A cavitation event was recorded when the signal loss at the focus for a given image fell below the baseline value by more than 5 standard deviations.

Simultaneous to this experiment, the PCD receiver recorded the acoustic emissions at the focus of the transducer. These waveforms were composed mainly of the acoustic

pulse as it reflected off of the various surfaces within the experimental setup and, when present, cavitation emissions and cavitation backscatter. The cavitation threshold was computed by first subtracting the contributions made by reflections from each recorded waveform. These contributions were expected to vary linearly with increasing pressure amplitude. They were estimated by first averaging together the 100 waveforms recorded at 24 MPa and then averaging together the 100 waveforms recorded at 25 MPa and then multiplying the difference between these two averaged waveforms by each pressure level. A cavitation event was recorded when the integral of the magnitude of the signal remaining after subtraction exceeded the average integral value at 25 MPa by more than 5 standard deviations.

### **3.2.4 Experiment B: Tissue Treatment**

The 1-D spin-echo sequence was used to monitor therapy in 12 in-vitro porcine liver and 12 in-vitro porcine brain samples harvested from a nearby slaughterhouse. Within twenty-four hours, the tissues were cut into pieces, immersed in degassed saline and held under -15 mm mercury vacuum for two additional hours. Liver pieces were cut from the edges of each liver lobe where blood vessels were the smallest. Brain pieces were cut from nearly every portion of the brain except for the brain stem. Typical attenuation coefficients for liver and brain range between 0.5 and 0.6 dB cm<sup>-1</sup> MHz<sup>-1</sup> [23]. After being held in vacuum, the samples were placed in 1.5 cm wide by 2.5 cm long cylindrical molds and covered in 2% agar. After gelation, each agar-sample construct was removed from its mold and placed in the transducer focus.

Tissue samples were treated with 800 histotripsy pulses using the line-scan sequence. Six liver and six brain samples were imaged using the high spatial frequency sequence while the other six liver and six brain samples were imaged using the low spatial frequency sequence. The histotripsy pulses had an estimated peak negative pressure of 35 MPa. One additional sample of brain tissue was imaged with the EPI sequence, applying 400 histotripsy cavitation pulses interleaved with 400 control images.

Throughout each experiment, the PCD system collected time-voltage waveforms proportional to the acoustic pressure incident on the receiver.

The signal losses induced by individual bubble clouds were extracted from the histotripsy images by averaging the pixels of each image that lay within a region of interest

(ROI) set about the transducer focus. For comparison across tissue samples, each series of these values was then normalized to the signal level at the transducer focus prior to therapy. We then used the same method to extract any changes in the MR signal of the tissue as observed by the control images.

In order to quantify the observability of the bubble clouds, we estimated the minimum pulse number where the bubble cloud demonstrated at least a 50% chance of being observed. This was calculated by finding the smallest pulse number applied to six samples with a common k-space frequency and tissue type, where at least three of the six samples demonstrated a contrast-to-noise ratio (CNR) above 5. CNR was calculated by subtracting the mean focal signal of the histotripsy image from that of the preceding control image and then dividing by the standard deviation of the signal from a region outside the extent of the tissue sample.

### 3.3 Results

#### 3.3.1 Experiment A: Cavitation Detection in Gel

The pressure-probability results produced by both the PCD and MRI systems as well as sigmoid functions fitted to these results are plotted in Fig. (3.4). The fit to the PCD data indicates a 0.5 cavitation probability threshold at 26.4 MPa peak negative pressure. The fit to the MRI data indicates a threshold at 26.6 MPa peak negative pressure. Pulses with pressures at or above 27 MPa produced significant MR-signal loss at least 90% of the time.

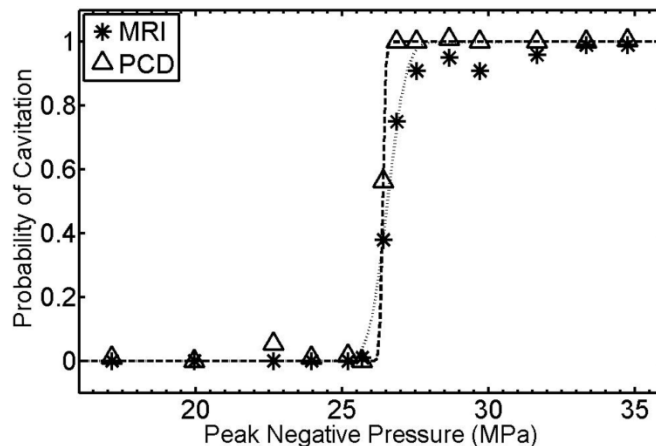


**Figure 3.4: Probability–pressure data and fitted curves obtained using the cavitation sensitized line-scan sequence and the passive cavitation detection (PCD) system. The PCD and MRI based methods show a 0.5 probability cavitation threshold at 26.4 and 26.6 MPa peak negative pressures respectively. These measurements were taken in a gel sample pre-treated with 1000**

**histotripsy pulses. Intact tissues, unlike the gel sample used here, may interfere with water motion and inhibit the performance of the MR sequence.**

### 3.3.2 Experiment B: Tissue Treatment

The mean and standard deviation of the cavitation sensitized signal at the transducer focus for each tissue type and k-space frequency are plotted as a function of pulse number and displayed in Fig. (3.5).

By the end of therapy, all 24 tissue samples displayed cavitation induced signal loss with a CNR of at least 5. However, the point at which cavitation specific contrast became differentiable from the control signal varied with the sensitivity of the imaging sequence. When imaged with a k-space frequency of  $400 \text{ cm}^{-1}$ , the first histotripsy pulses applied in liver generated signal loss greater than 40 %. With each successive pulse, the MR signal continued to decrease until it reached a baseline at about 25% of the control signal, where it remained until completion of therapy. The noise floor across the experiments varied between 3 and 12%. For these tissue samples, 0.5 probability of detection was achieved by the 5<sup>th</sup> pulse.

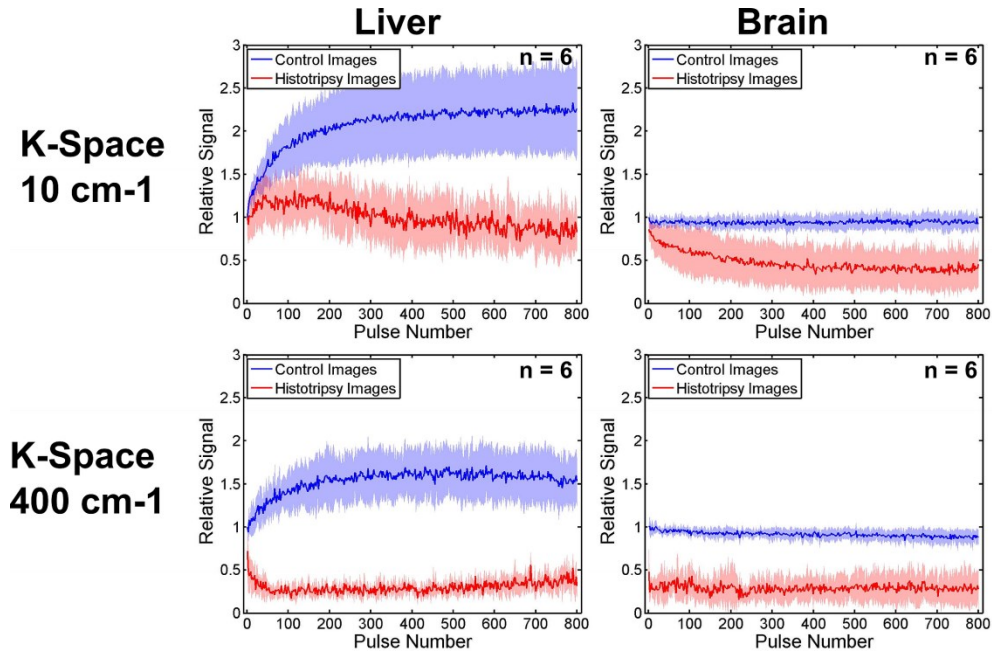


**Figure 3.5: The mean (dark line) and standard deviation (light envelope) of the motion weighted and T2-weighted signal (T2W) at the cavitation site vs the number of acoustic pulses applied to the sample. For images acquired at low spatial frequencies, signal loss caused by cavitation is not immediately differentiable from the T2-weighted signal, where cavitation-based motion is not present. However, this signal does become differentiable after several acoustic pulses are applied to the tissue target. At high spatial frequencies, cavitation specific contrast is immediately apparent and**

**remains differentiable over the course of treatment. The T2-weighted signal in liver increases with treatment pulse number, but remains constant in brain.**

In brain, when imaged with a k-space frequency of  $400 \text{ cm}^{-1}$ , the very first histotripsy pulse attenuated the signal between 60% and 80 % and always produced a CNR above 5. Like the liver case above, the MR signal continued to decrease until it reached a baseline at about 25% of the control signal, where it remained until completion of therapy. For these tissue samples, 0.5 probability of detection was achieved by the 1<sup>st</sup> pulse.

The cavitation sensitized signal in tissue samples imaged with a k-space frequency of  $10 \text{ cm}^{-1}$  did not produce a detectable amount of contrast until several pulses into treatment. The brain tissue samples demonstrated 0.5 probability of detection at the 15<sup>th</sup> pulse while the liver tissue samples demonstrated 0.5 probability of detection at the 63<sup>rd</sup> pulse.

In both brain and liver tissues scanned at low spatial frequency encoding, the cavitation sensitized signal reached a steady state of about 50% of the control signal, as opposed to the 25% signal level of the high spatial frequency encoding case.

By the end of therapy, the control signal in all 12 liver samples was 1.5 to 2.5 times greater than it was at the start of therapy. Further, this difference was at least 10 times larger than the noise floor. The control signal in all 12 brain samples did not demonstrate a significant change over the course of treatment.

The PCD signal displayed consistent levels across all histotripsy pulses in all the tissue experiments.

### **3.3.3 2D Imaging**

The first images taken with the 2D EPI sequence are displayed in Fig. (3.6) and corroborate with the 1D-line-scan results. The sample, imaged at k-space frequency of  $300 \text{ cm}^{-1}$ , displays cavitation specific contrast within the first two acoustic pulses.



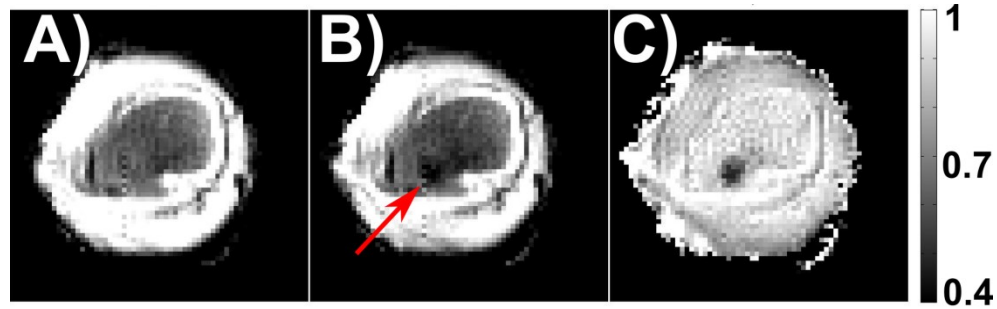


Figure 3.6: Echo-planar images (EPI) of a sample of brain tissue taken (A) prior to therapy, and (B) over the first two acoustic pulses applied to the sample. The sensitizing gradient extends to a  $k$ -space frequency of  $300 \text{ cm}^{-1}$ . The bubble clouds applied in (B) cause localized signal attenuation as indicated by the arrow. Dividing the image in (B) by the image in (A) isolates cavitation specific contrast and the result is shown in (C). The EPI sequence is able to detect and localize the first two histotripsy pulses applied to the tissue sample.

### 3.4 Discussion

#### 3.4.1 Cavitation Detection without a Gel Matrix

The MRI and PCD sequence indicated a 0.5 probability threshold within 0.2 MPa of each other. Further, both threshold values are within one MPa to thresholds reported in the literature [24], [25].

At pressures below 32 MPa, the MR sequence reports about 10% fewer cavitation events than the PCD system. This is possibly because the acoustic pulses at pressures below 32 MPa produced small bubble clouds. Unlike the PCD system, the MR line-scan sequence is subject to partial volume effects. Bubble clouds that cause motion outside the intersection of the two excitation planes, or bubble clouds that cause incoherent motion in a sub-voxel volume, will less effectively generate MR signal loss but will still be detected by acoustic methods.

#### 3.4.2 Detecting the First Bubble Cloud in Tissue

The results shown in Fig. (3.5) confirm our hypothesis that the initial bubble clouds formed in tissues can be detected using MRI sequences. The very first cloud formed in brain tissue is consistently detectable. Meanwhile, in the liver, the bubble cloud is consistently detectable by the 5<sup>th</sup> pulse. Further, the PCD signal remained quite uniform across all pulses in all the tissue experiments, indicating that the cavitation behavior did not change in a systematic manner during treatment.

It is currently unclear if applying 1 histotripsy pulse in the brain or 5 pulses in the liver will cause irreversible damage. Previous studies have indicated that small pulse numbers

of histotripsy in rabbit kidney create scattered foci of hemorrhage and cell debris [26], [27]. But it is unknown if this trend continues in the brain and liver, or if these organs will recover from such damage.

It appears from Fig. (3.5) that, with a k-space frequency of  $400 \text{ cm}^{-1}$ , the first bubble cloud formed in liver causes less signal attenuation than the first cloud formed in brain. This may be due to the liver being a stiffer tissue than the brain, leading the bubble cloud to have more difficulty driving flow. Scans at higher sensitivities or higher resolutions may better observe the first bubble cloud formed in liver.

For therapy in very stiff media such as fibrotic tissue, achieving sufficient resolution and sensitivity to visualize the bubble cloud will likely require trade-offs between imaging time, resolution, and image fidelity. In addition, the waveforms in the high sensitivity cases of this study already have b-values above  $100 \text{ s mm}^{-2}$ , resulting in images moderately sensitive to thermal diffusion. Further increases in cavitation sensitivity will produce images even more sensitive to non-cavitation related sources of motion.

### **3.4.3 Lesion Monitoring Through Cloud Detection**

Images acquired with low sensitivity to cavitation do not immediately produce statistically significant signal loss. However, as successive pulses are applied to the tissue, the bubble cloud becomes more apparent. We suspect this behavior is an indication of disruption of the tissue. As the cellular structure breaks down, there will be less resistance to flow at the focus, leading to more signal attenuation. If this is true, it may be possible to use cavitation sensitized MR sequences to monitor the progression of the histotripsy lesion. One may be able to choose an imaging sensitivity such that contrast is saturated once the lesion reaches a desired state of homogenization.

### **3.4.4 Lesion Monitoring Through T2-Weighted Imaging.**

By the end of treatment, the control signal of each liver sample demonstrates 1.5 to 2.5 times more amplitude at the end of treatment compared to the beginning, with this difference in signal being at least 10 times larger than the noise floor. The majority of the signal increase occurs in the first 200 pulses, with diminishing gains for every pulse after that. This trend of an initial rapid increase in contrast followed by more gentle, asymptotic changes is also found in studies of other measures of histotripsy lesions such as acoustic backscatter reduction in kidney [26], Young's modulus in liver [28], color Doppler

ultrasound [29], and optical measurements [30]. Preliminary studies have found some correlation between T2 elevation and liver tissue homogenization [2], [4], [31]–[34]. It is currently unclear why the T2 weighted contrast in brain does not change in response to homogenization.

### **3.4.5 Real Time 2D Targeting and Monitoring**

The images in Fig. (3.6) suggest that the principles behind 1D MR-based cavitation detection can be extended to 2D imaging. The EPI sequence is able to detect and localize the first two bubble clouds formed in the target.

In a clinical setting, the location of the transducer focus may not be precisely known. It may be more preferable to use 2D and 3D imaging sequences to localize the first histotripsy bubble clouds applied to the target. In addition, many clinical systems do not have the same field strength and gradient capability as the 7T scanner used here. Operating with reduced maximum gradient amplitudes, reduced slew rates, and reduced signal-to-noise ratios may hinder detecting the first bubble clouds formed in tissues. Further adaptations, such as longer gradient times, pulsing to multiple locations during a single acquisition, or modifying the pulsing parameters to maintain longer bursts of cavitation activity, may be necessary to overcome these limitations. It may also be necessary to first use reversible focus finding methods such as thermometry or acoustic radiation force imaging to narrow in on the likely location of the bubble cloud. Once this region is located, the operator can determine the optimal set of tradeoffs to yield the best image of the bubble cloud.

This study reduces the chance of generating an appreciable acoustic radiation force or streaming by using very short pulses with a very low duty cycle. Other pulsing methods with higher duty cycles or longer pulse lengths may successfully generate a radiation force displacement or streaming effect. These motions will introduce both phase and magnitude perturbations to the signal at the focus.

We envision an MR-guided histotripsy protocol that uses sequences that apply both high and low k-space frequencies. At the start of therapy, the operator will use sequences with high k-space frequencies to verify proper placement of the bubble cloud. Then, over the course of treatment, the operator will use sequences with low k-space frequencies to monitor the disruption of the target. As the tissue is disrupted, the negative contrast in the MR images will also increase.

### 3.5 Conclusion

Cavitation-sensitive MR sequences can detect the incoherent, intravoxel water motion introduced by histotripsy bubble clouds formed in biologic tissue. Though, at the onset of treatment, intact tissue structures may inhibit water flow, these sequences can still capture cavitation specific contrast when their gradient waveforms enable a sufficiently high sensitivity. Sequences with very low sensitivity have difficulty observing the first bubble clouds formed in tissues. However, in this case, cavitation specific contrast may become visible as the tissue target is progressively destroyed.

### 3.6 References

- [1] S. P. Allen, L. Hernandez-Garcia, C. A. Cain, and T. L. Hall, "MR-based detection of individual histotripsy bubble clouds formed in tissues and phantoms," *Magn. Reson. Med.*, Nov. 2015.
- [2] Y. Kim, E. Vlasisavljevich, G. E. Owens, S. P. Allen, C. A. Cain, and Z. Xu, "In vivo transcostal histotripsy therapy without aberration correction," *Phys. Med. Biol.*, vol. 59, no. 11, pp. 2553–2568, Jun. 2014.
- [3] Y. Kim, T. Y. Wang, X. Zhen, and C. A. Cain, "Lesion generation through ribs using histotripsy therapy without aberration correction," *IEEE Trans. Ultrason. Ferroelectr. Freq. Control*, vol. 58, no. 11, pp. 2334–2343, 2011.
- [4] E. Vlasisavljevich, Y. Kim, S. P. Allen, G. Owens, S. Pelletier, C. A. Cain, K. Ives, and Z. Xu, "Image-guided non-invasive ultrasound liver ablation using histotripsy: feasibility study in an in vivo porcine model," *Ultrasound Med. Biol.*, vol. 39, no. 8, pp. 1398–1409, 2013.
- [5] C. D. Arvanitis and N. McDannold, "Integrated ultrasound and magnetic resonance imaging for simultaneous temperature and cavitation monitoring during focused ultrasound therapies.," *Med. Phys.*, vol. 40, p. 112901, Nov. 2013.
- [6] T. A. Bigelow, G. Davis, A. Avendano, P. Shrotriya, K. Bergler, J. Xu, T. A. Bigelow, G. Davis, A. Avendano, P. Shrotriya, K. Bergler, and Z. Hu, "Dependence of ablative ability of high-intensity focused ultrasound cavitation-based histotripsy on mechanical properties of agar," *J. Acoust. Soc. Am.*, vol. 136, pp. 3018–3027, Dec. 2014.
- [7] M. Gyöngy and C. C. Coussios, "Passive spatial mapping of inertial cavitation during HIFU exposure," *IEEE Trans. Biomed. Eng.*, vol. 57, no. 1, pp. 48–56, 2010.
- [8] M. A. O'Reilly, R. M. Jones, K. Hynynen, M. O'Reilly, R. M. Jones, and K. Hynynen, "Three-dimensional transcranial ultrasound imaging of microbubble clouds using a sparse hemispherical array.," *IEEE Trans. Biomed. Eng.*, vol. 61, no. 4, pp. 1285–1294, Apr. 2014.
- [9] G. T. Clement and K. Hynynen, "A non-invasive method for focusing ultrasound

- through the human skull.,” *Phys. Med. Biol.*, vol. 47, no. 8, pp. 1219–1236, 2002.
- [10] G. W. Miller, M. Eames, J. Snell, and J.-F. Aubry, “Ultrashort echo-time MRI versus CT for skull aberration correction in MR-guided transcranial focused ultrasound: In vitro comparison on human calvaria,” *Med. Phys.*, vol. 42, no. 5, pp. 2223–2233, 2015.
- [11] C. D. Arvanitis, G. Clement, and N. McDannold, “Transcranial assessment and visualization of acoustic cavitation: modeling and experimental validation,” *IEEE Trans. Med. Imaging*, vol. 34, no. 6, pp. 1270–1281, Dec. 2015.
- [12] T. D. Khokhlova, M. S. Canney, D. Lee, K. I. Marro, L. A. Crum, V. A. Khokhlova, and M. R. Bailey, “Magnetic resonance imaging of boiling induced by high intensity focused ultrasound,” *J. Acoust. Soc. Am.*, vol. 125, no. 4, pp. 2420–2431, Apr. 2009.
- [13] C. Damianou, K. Ioannides, V. Hadjisavvas, N. Mylonas, A. Couppis, D. Iosif, and P. A. Kyriacou, “MRI monitoring of lesions created at temperature below the boiling point and of lesions created above the boiling point using high intensity focused ultrasound,” *J. Biomed. Sci. Eng.*, vol. 03, no. 08, pp. 763–775, Aug. 2010.
- [14] A. L. Alexander, T. T. McCreery, T. R. Barrette, A. F. Gmitro, and E. C. Unger, “Microbubbles as novel pressure-sensitive MR contrast agents,” *Magn. Reson. Med.*, vol. 35, no. 6, pp. 801–806, 1996.
- [15] J. S. Cheung, A. M. Chow, H. Guo, and E. X. Wu, “Microbubbles as a novel contrast agent for brain MRI,” *Neuroimage*, vol. 46, no. 3, pp. 658–664, 2009.
- [16] R. Dharmakumar, D. B. Plewes, and G. A. Wright, “On the parameters affecting the sensitivity of MR measures of pressure with microbubbles,” *Magn. Reson. Med.*, vol. 47, no. 2, pp. 264–273, 2002.
- [17] T. Ueguchi, Y. Tanaka, S. Hamada, R. Kawamoto, Y. Ogata, M. Matsumoto, H. Nakamura, and T. Johkoh, “Air microbubbles as MR susceptibility contrast agent at 1.5 tesla,” *Magn. Reson. Med. Sci.*, vol. 5, no. 3, pp. 147–150, 2006.
- [18] S. P. Allen, T. L. Hall, C. A. Cain, and L. Hernandez-Garcia, “Controlling cavitation-based image contrast in focused ultrasound histotripsy surgery,” *Magn. Reson. Med.*, vol. 73, pp. 204–213, Jan. 2015.
- [19] S. C. Lin, C. W. Chen, C. H. Wu, C. H. Wang, S. T. Kang, C. K. Yeh, W. S. Chen, and H. H. Peng, “Real-time monitoring of inertial cavitation effect on diluted microbubbles by MRI,” in *Proceedings of the 21st Annual Meeting of ISMRM*, 2013, p. 1825.
- [20] J. E. Parsons, C. A. Cain, and J. B. Fowlkes, “Cost-effective assembly of a basic fiber-optic hydrophone for measurement of high-amplitude therapeutic ultrasound fields,” *J. Acoust. Soc. Am.*, vol. 119, no. 3, pp. 1432–1440, 2006.
- [21] K. W. Lin, Y. Kim, A. D. Maxwell, T. Y. Wang, T. L. Hall, Z. Xu, J. B. Fowlkes, and C. A. Cain, “Histotripsy beyond the intrinsic cavitation threshold using very short ultrasound pulses: microtripsy,” *IEEE Trans. Ultrason. Ferroelectr. Freq. Control*, vol. 61, no. 2, pp. 251–265, 2014.

- [22] C. A. Branch, L. Hernandez, M. Yongbi, N. C. Huang, and J. A. Helpem, "Rapid and continuous monitoring of cerebral perfusion by magnetic resonance line scan assessment with arterial spin tagging.," *NMR Biomed.*, vol. 12, no. 1, pp. 15–25, 1999.
- [23] M. O. Culjat, D. Goldenberg, P. Tewari, and R. S. Singh, "A review of tissue substitutes for ultrasound imaging.," *Ultrasound Med. Biol.*, vol. 36, no. 6, pp. 861–73, Jun. 2010.
- [24] E. Vlaisavljevich, K.-W. Lin, A. Maxwell, M. T. Warnez, L. Mancina, R. Singh, A. J. Putnam, B. Fowlkes, E. Johnsen, C. Cain, and Z. Xu, "Effects of ultrasound frequency and tissue stiffness on the histotripsy intrinsic threshold for cavitation.," *Ultrasound Med. Biol.*, vol. 41, no. 6, pp. 1651–1667, Mar. 2015.
- [25] A. D. Maxwell, C. A. Cain, T. L. Hall, J. B. Fowlkes, and Z. Xu, "Probability of cavitation for single ultrasound pulses applied to tissues and tissue-mimicking materials," *Ultrasound Med. Biol.*, vol. 39, no. 3, pp. 449–465, 2013.
- [26] T.-Y. Y. Wang, Z. Xu, F. Winterroth, T. L. Hall, J. B. Fowlkes, E. D. Rothman, W. W. Roberts, and C. A. Cain, "Quantitative ultrasound backscatter for pulsed cavitation ultrasound therapy-histotripsy," *IEEE Trans. Ultrason. Ferroelectr. Freq. Control*, vol. 56, no. 5, pp. 995–1005, May 2009.
- [27] W. W. Roberts, T. L. Hall, K. Ives, J. S. Wolf Jr, J. B. Fowlkes, and C. A. Cain, "Pulsed cavitation ultrasound: a noninvasive technology for controlled tissue ablation (histotripsy) in the rabbit kidney," *J. Urol.*, vol. 175, no. 2, pp. 734–738, 2006.
- [28] T. Y. Wang, T. L. Hall, Z. Xu, J. B. Fowlkes, and C. A. Cain, "Imaging feedback of histotripsy treatments using ultrasound shear wave elastography," *IEEE Trans. Ultrason. Ferroelectr. Freq. Control*, vol. 59, no. 6, pp. 1167–1181, 2012.
- [29] X. Zhang, R. M. Miller, K.-W. Lin, A. M. Levin, G. E. Owens, H. S. Gurm, C. A. Cain, and Z. Xu, "Real-time feedback of histotripsy thrombolysis using bubble-induced color Doppler.," *Ultrasound Med. Biol.*, vol. 41, no. 5, pp. 1386–401, May 2015.
- [30] T. Y. Wang, Z. Xu, T. L. Hall, J. B. Fowlkes, and C. A. Cain, "An efficient treatment strategy for histotripsy by removing cavitation memory," *Ultrasound Med. Biol.*, vol. 38, no. 5, pp. 753–766, 2012.
- [31] Y. Kim, C. G. Fifer, S. K. Gelehrter, G. E. Owens, D. R. Berman, E. Vlaisavljevich, S. P. Allen, M. F. Ladino-Torres, and Z. Xu, "Developmental impact and lesion maturation of histotripsy-mediated non-invasive tissue ablation in a fetal sheep model," *Ultrasound Med. Biol.*, vol. 39, no. 6, pp. 1047–1055, Jun. 2013.
- [32] T. L. Hall, G. R. Lee, L. Hernandez, and C. A. Cain, "Relaxation properties of cavitation induced tissue lesions," in *Proceedings of the 15th Annual Meeting of ISMRM*, 2007, p. 1118.
- [33] S. P. Allen, W. W. Roberts, T. L. Hall, C. A. Cain, and L. Hernandez, "Characterization of in vivo histotripsy lesions using high field MRI," in

*Proceedings of the 20th Annual Meeting of ISMRM*, 2012, p. 1582.

- [34] A. Partanen, N. Farr, W. Kreider, T. Khokhlova, A. Maxwell, Y.-N. Wang, M. Bailey, and V. Khokhlova, “Use of MRI to visualize mechanically fractionated lesions generated by boiling histotripsy in tissue,” in *Abstract Book of 14th International Symposium for Therapeutic Ultrasound*, 2014.

# Chapter 4:

## Response of MR Contrast Parameters to Treatment by Histotripsy in Various Ex Vivo Tissues and Tissue Mimicking Materials

### 4.1 Introduction

The previous two chapters addressed using MRI to visualize histotripsy bubble clouds. In this chapter, we will turn our attention to using MRI to assess the state of tissues ablated by histotripsy. This effort is motivated by the fact that MR images display excellent contrast between different soft tissues. The processes behind MR signal evolution, and thus image contrast, are influenced by behaviors that occur across several orders of magnitude in both size and time. These processes are the longitudinal relaxation process, the transverse relaxation process, and the Brownian motion (thermal diffusion) process, which are characterized by the mathematic constants  $R1$ ,  $R2$ , and the apparent diffusion coefficient ( $ADC$ ), respectively. Meanwhile, histotripsy divides and breaks apart the structure of soft tissues on a cellular level. The hypothesis of this chapter is that fractionation by histotripsy will influence some of the processes that contribute to  $R1$ ,  $R2$ , and the  $ADC$  and ultimately alter their apparent values.

Previous work has suggested that the MR transverse relaxation process and the diffusion process in biologic tissues are both sensitive to mechanical disruption by histotripsy. For example, histotripsy lesions have been shown to display  $R2$  and  $ADC$  weighted contrast in MR images of porcine liver [1], [2] and canine prostate [3]. The morphology of liver lesions in  $R2$  weighted images has displayed a close correlation to their histologic morphology [4]–[6]. The same has been observed in fetal sheep kidney and liver



[7]. In addition, a recent study in mice tumors has shown slight R2-weighted contrast with ablation [8].

Though these results are promising, the studies used to obtain them are non-systematic in their approach to histotripsy delivery and, mostly, merely report image contrast as opposed to quantified R2 or ADC values. They also do not differentiate between changes in MR image contrast caused by bleeding and edema and those caused by the fractionation of cellular tissue. In addition, as of writing this chapter, there have been no published reports addressing the response of R1 to ablation by histotripsy. This chapter presents a systematic survey of these constants as estimated in various ex-vivo tissues and tissue mimicking phantoms after exposure to various amounts of histotripsy. It will then present a small study on how edema and hemorrhage can affect MR images of histotripsy lesions.

## **4.2 Materials and Methods**

This section presents the materials and methods used to conduct a survey of MR contrast parameters in histotripsy lesions in a variety of ex vivo tissues and tissue mimicking phantoms.

### **4.2.1 Transducer Design and Lesion Formation in Ex Vivo Tissues**

Histotripsy lesions were made in tissue targets using a custom built, 30 cm diameter hemi-spherical array composed of 256 circular elements, each with a diameter of 2 cm and a center frequency of 500 kHz. The transducer had a focal depth of 15 cm and -6 dB axial and longitudinal beam widths of 1.5 and 3.5 mm respectively and could produce peak negative pressures exceeding 30 MPa, as described in [9]. Tissue samples were placed on an arm connected to a 3-axis mechanical positioning system and moved into the transducer focus. Uniform lesions with varying amounts of treatment effect were then made by depositing two-cycle acoustic pulses ( $\sim 5 \mu\text{s}$  long) to points on a grid spaced 0.66 mm apart using a randomly generated trajectory and firing at a rate of 10 Hz. Steering during treatment was performed by electronically varying the delay between individual elements. Total lesion size varied from 4 mm to 6 mm along each edge. This pattern was repeated until 1, 3, 10, 30, 100, or 300 pulses, or, in the special case of muscle tissue, 3, 10, 30, 100, 300, or 1000 pulses had been deposited per grid point.

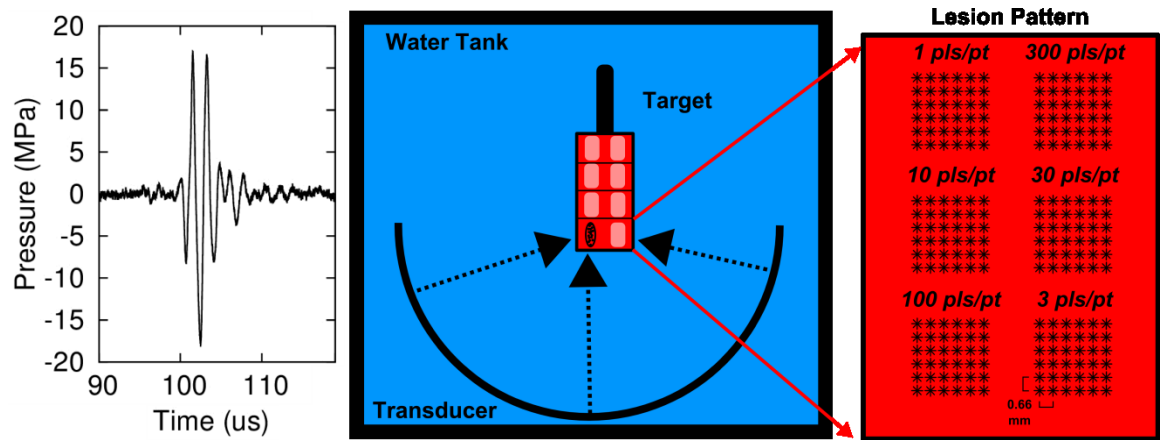


**Figure 4.1: Example acoustic pulse (left), transducer setup (center) and acoustic pulse deposition patterns (right) used to form lesions in ex vivo tissues. Six lesions, each made by depositing different numbers of acoustic pulses per point (pls/pt) are made on a single plane perpendicular to the propagation axis. The target was translated such that 4 planes of lesions were formed in each sample.**

Once a lesion was made, the mechanical arm was translated along the plane transverse to the propagation direction of the ultrasound beam such that a new portion of the sample was placed into the focal zone. This new location was then treated. This was repeated until one lesion of each pulse number was formed in a plane perpendicular to the ultrasound propagation direction. A new plane of lesions was then formed until a total of four lesions for each pulse deposition number were formed in each tissue sample. See Fig (4.1) for a schematic of the setup. Lesions were made in porcine liver, kidney, and muscle, as well as bovine brain. Lesions were also made in clotted bovine blood and formulations of bovine red blood cells (RBC's) suspended in agar gel.

#### **4.2.2 Ex Vivo Tissue and Phantom Preparation**

All tissue samples were acquired from a local slaughterhouse and stored for at most 48 hours before use. Prior to treatment, the samples were first immersed in saline and held under -28 mm Hg pressure for two hours. Most tissue samples were then trimmed and placed within a 4 x 4 x 6.5 cm rectangular prism-shaped holder with four sides comprised of thin plastic tape, one side kept open, and one side made of solid plastic which was attached to the positioning arm. Agar gel (4% w/wt) was then injected into any air gaps between the tissue sample and the holder walls. Additional details specific to each tissue type are described below.

### **Liver**

Liver was acquired from an adult pig no more than 2 years old, and several 8 mm thick slabs of the liver were excised and oriented inside the holder such that the plane of each slab was orthogonal to the direction of ultrasound propagation. Multiple slabs were added into the holder until the volume was filled. During treatment, the transducer focus was placed such that the resulting lesions would be entirely contained within each slab.

### **Brain**

Bovine brain was acquired from an adult cow no more than 3 years in age. After acquisition, and prior to insertion into the holder, the sample was bisected into a hemi-section and the cerebral spinal fluid was drained from the ventricles. The cerebrum was then excised and packed into the holder. The remaining small airgaps in the sulci were filled with gel.

### **Kidney**

Kidney was acquired from the left side of a juvenile pig between 40-60 kg. The kidney sample was prepared nearly identically to the liver sample. However, prior to trimming and insertion, the kidney was cut in half into two hemi sections and the collecting system was removed. The remaining cortex and medulla were then trimmed into 4.5 x 4.5 x 1.5 cm slabs and placed into the holder with the plane of each slab perpendicular to the propagation direction of the acoustic beam. The small air gaps between each slab were then filled with agar gel. During treatment, the transducer focus was placed such that the resulting lesions would be entirely contained within each slab.

### **Muscle**

A 10 x 6 x 1 cm slab of muscle was acquired from the left butt of a juvenile pig between 40-60 kg. To prevent rigor mortis, this sample was treated within 4 hours of harvest with no intervening period of refrigeration. Further, the muscle sample was vacuum-packed instead of being placed in the holder because the gel had difficulty filling all air holes and gaps in the tissue. Since the sample was long and thin, the 4 lesions of each pulse deposition number were made all on the same plane, perpendicular to the ultrasound propagation direction.

### **RBC Phantoms**

Red blood cell suspensions were prepared by first holding citrated bovine blood under vacuum for 30 minutes, then spinning down the blood and mixing the resulting pellet with 4% w/wt agar gel (Lab Scientific, product # AG-SP). The mixture was then poured into the holder and allowed to solidify. Three suspensions were made containing 16%, 6%, and 3% w/volume of red blood cells, respectively. The top portion of the holders were then covered with a 5 mm thick layer of pure 5% agar gel to act as a diffusion barrier between the isotonic red blood cells and the coupling bath.

### **Clot**

Bovine blood clot was formed by first holding 95 mL of citrated bovine blood under -28 mmHg pressure for thirty minutes and then warming the degassed solution in an incubator to 30°C. The blood was then mixed with 190  $\mu$ L of calcium chloride and poured into the rectangular holder. After pouring, the holder was incubated in a water bath at 38°C for three hours and then cooled to 4°C for another 8 hours before treatment. Prior to insertion into the water tank, the top of the clot was covered with a 5 mm thick layer of 5% agar gel to, like in the case of the red blood cell formulations, act as a diffusion barrier.

#### **4.2.3 MRI Imaging**

After treatment, each tissue sample was placed in the bore of a 7T small animal scanner (Agilent, Walnut Creek, CA). Sufficient data to estimate R1, R2, and ADC in each lesion was collected by acquiring multiple inversion-recovery-weighted, echo-time-weighted, and diffusion-weighted multi-slice, spin-echo images of slices orthogonal to the propagation direction of the ultrasound. Slice planning was chosen such that two consecutive slices transected every lesion formed in a tissue sample. For these scans, either the inversion recovery time (TI), the echo time (TE), or the diffusion-weighting value (b) were respectively varied across multiple values. In order to optimize both the image signal to noise ratio and sampling along the respective relaxation and diffusion curves, these and other imaging parameters were varied between tissues samples. These parameters are reported in Table 4.1.

Contrast Parameter	Common Between Acquisitions	T1 Estimate			T2 Estimate			ADC Estimate		
		TR/TE (s/ms)	Averages	TI (s)	TR (s)	Averages	TE (ms)	TR/TE (s/ms)	Averages	b value (s mm <sup>-2</sup> )
MR Parameters	FOV/Bandwidth/Matrix (cm/kHz)									
In Vivo Liver	5 x 7 x 0.2 / 50 / 100 x 140 x 1	5/10	1	(0.7, 1.0, 1.5, 2.1, 3.0)	5	1	(10, 18, 32, 56, 100)	5/24	4	(1, 182, 725, 1631)
Ex Vivo Liver	6 x 5 x 0.1 / 50 / 120 x 110 x 16	4 / 15	1	(0.1, 0.8, 1.5, 2.2, 3.0)	5	1	(16, 21, 28, 38, 50)	4 / 23	4	(4, 181, 713, 1600)
Brain	5.5 x 5 x 0.2 / 50 / 110 x 100 x 16	15 / 20	1	(0.1, 0.6, 1.0, 1.5, 2.0)	15	1	(15, 28, 42, 65, 100)	15 / 27	1	(3, 120, 469, 1053)
Kidney	6 x 5.5 x 0.1 / 50 / 120 x 110 x 16	8 / 15	1	(0.1, 0.8, 1.6, 2.3, 3.0)	8	1	(16, 25, 40, 63, 100)	2 / 27	5	(37, 203, 802, 1800)
Muscle	12 x 6.5 x 0.1 / 50 / 240 x 130 x 2	9 / 17	1	(0.0, 0.8, 1.5, 2.3, 3.0)	9	1	(17, 35, 54, 71, 90)	6 / 29	5	(3, 203, 802, 1800)
Clot	5 x 5 x 0.2 / 100 / 100 x 100 x 16	5.5 / 8	1	(0.1, 0.6, 1.0, 1.5, 2.0)	5.5	1	(8, 12, 20, 31, 50)	2.6 / 18	4	(0, 111, 444, 1000)
16% RBC	5 x 5 x 0.1 / 50 / 100 x 100 x 16	7.5 / 15	1	(0.107, 1.3, 1.9, 2.5)	1.5	1	(15, 24, 33, 41, 50)	3.5 / 21	3	(1, 123, 490, 1100)
6% RBC	5 x 5 x 0.1 / 50 / 100 x 100 x 16	7 / 8	1	(0.1, 0.8, 1.6, 2.3, 3.0)	7	1	(18, 28, 42, 65, 100)	5 / 20	1	(1, 111, 444, 999)
3% RBC	5 x 5 x 1 / 50 / 100 x 100 x 16	10 / 15	1	(0.1, 0.8, 1.6, 2.3, 3.0)	10	1	(15, 22, 34, 48, 70)	2 / 21	1	(1, 84, 333, 750)

Table 4.1: MR acquisition parameters used to acquire R1, R2 and ADC weighted images of histotripsy lesions made in several ex vivo tissues and tissue mimicking phantoms. Abbreviations are FOV = field of view, TR = repetition time, TE = echo time, TI = inversion recovery time, b value = diffusion weighting constant.

The contrast parameters T1, T2, and the ADC were estimated from the resulting magnitude images by drawing a 3.5 mm x 3.5 mm region of interest within each apparent lesion and taking the average of the pixels within the ROI. Four additional regions of tissue with identical dimensions that did not appear to be affected by the histotripsy pulses were selected as untreated control regions. MR contrast parameters for each ROI were estimated by computing least-squares fits to the following equations:

$$M_i = M_o + M_x e^{-TE_i/T2} \quad \text{q: 4.1}$$

$$M_j = M_o + M_x e^{-TI_j/T1} \quad \text{q: 4.2}$$

$$\ln(M_k) = M_o - ADC * b_k \quad \text{q: 4.3}$$

Here,  $TE_i$ ,  $TI_j$ , and  $b_k$  are imaging parameters unique to each scan sequence and  $M_{i,j \text{ or } k}$  are the average magnitude signal found within and ROI when acquired with either  $TE_i$ ,  $TI_j$ , or  $b_k$ . The variables  $M_o$ ,  $M_x$ ,  $T1$ ,  $T2$ , and  $ADC$ , were estimated using a Nelder-Mead simplex algorithm [10] implemented in MATLAB software (MathWorks, Natick, MA, USA). During fitting, both  $M_o$  and  $M_x$  displayed consistency within each sample. Most of the fitted curves matched the acquired data rather well. The squared correlation coefficient ( $R^2$ ) obtained for each fit is displayed in Fig (4.3) along with examples of the signal decay curves and the corresponding fits for the largest and smallest  $R^2$  values found in clot. The poorest fits occurred while imaging clot, where the large  $R^2$  rate of untreated clot significantly reduced the signal-to-noise ratio of the resulting images.

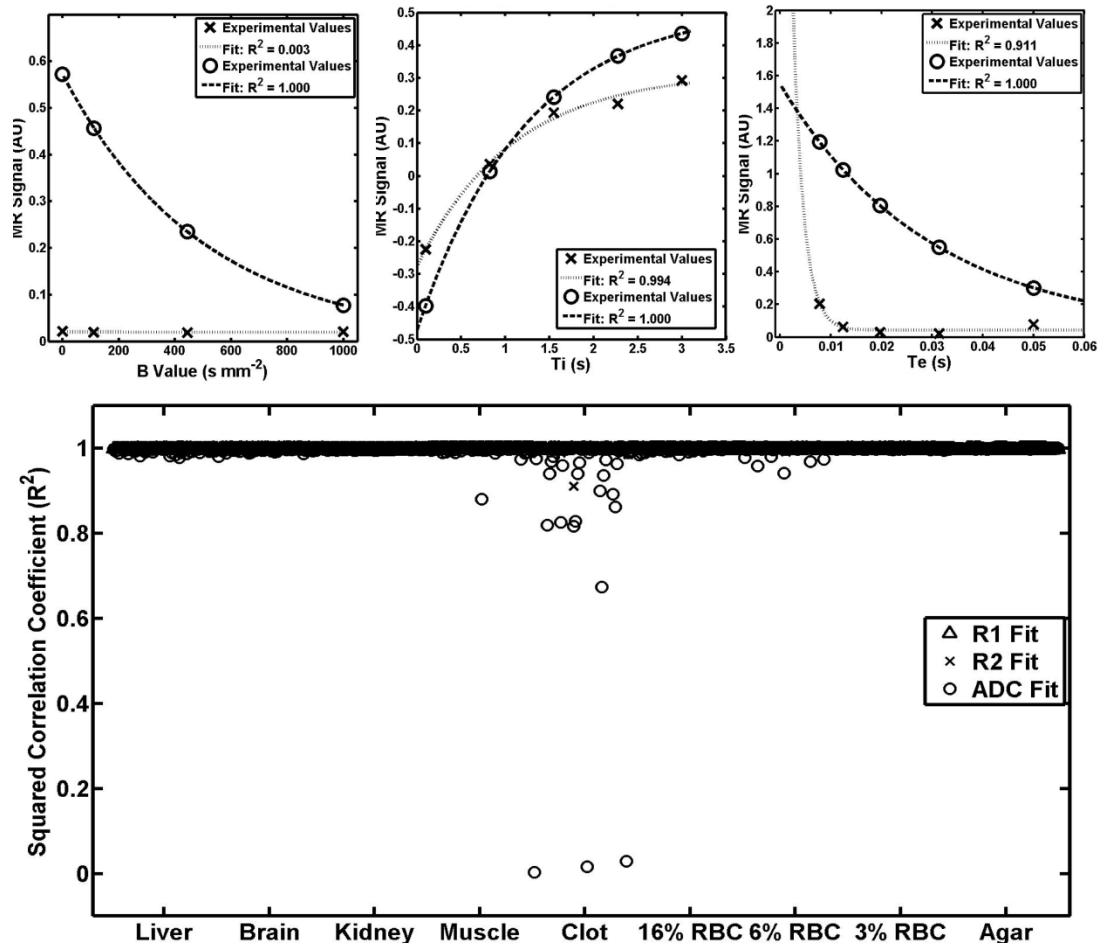


Figure 4.2: Top Row: Examples of the signal decay curves and their least squares fits obtained while computing the ADC (Left), R1 (Center), and R2 (Right) of clot. The fits with the highest and lowest squared correlation coefficient ( $R^2$ ) are both displayed. In these plots, X's correspond to the MR signal of the lesion that produced the lowest  $R^2$  value as a function of either  $b$  value,  $T_i$ , or  $T_e$ . The circles correspond to the signal of the lesion that produced the largest squared correlation coefficient as a function of either  $b$  value,  $t_i$ , or  $t_e$ . Bottom row: The  $R^2$  values for all fits produced in this study. Clot produced the largest number of poor fits due to low image signal in regions where it was not ablated. However, most of the fits performed in this study match the acquired data rather well.

## 4.3 Longitudinal Relaxation (R1)

### 4.3.1 Mechanism

In pure water, the R1 constant characterizes the rate at which a system of magnetic moments returns to thermal equilibrium after an imaging experiment. It is described in detail in reference [11]. In short, R1 is affected by how likely two hydrogen protons in on a water molecule will rotate about the attached oxygen atom at a rate equal to the Larmour frequency. When rotating at the correct rate, the two magnetic moments experience a magnetic field that fluctuates at the Larmour frequency and change magnetic states.

Interaction between rotational motion and magnetic state is the fundamental mechanism of longitudinal relaxation. When many water molecules rotate at or near the Larmour frequency, the R1 rate becomes very large and the system quickly returns to equilibrium. The possible rotation rates water molecules can experience at any given time are largely determined by the temperature of the water, its viscosity, and the size of the water molecules themselves. However, it was soon discovered that the variation in R1 rates between biologic tissues is too large to be attributed just to temperatures and viscosity differences. The prevailing theory is that the observed R1 rate in biologic tissues heavily modified by the introduction of paramagnetic particles and what has been called a fast-exchange, two-state mechanism.

Paramagnetic particles create magnetic field perturbations that exist over a larger volume of space than those created by hydrogen protons. They greatly enhance R1 when the rotational and diffusive motion of the paramagnetic particles and the water molecules conspire to create a magnetic field that fluctuates at the Larmour frequency [12]–[14]. In normal biologic tissues, paramagnetic materials usually appear as iron atoms attached to proteins such as ferritin and hemoglobin. Though, often, the iron attached to ferritin and hemoglobin are both too well sequestered from the surrounding water to strongly affect R1 [15], [16], there are special cases, such as methemoglobin and other blood breakdown products, that do have a strong influence on the R1 rate[17].

The so called fast-exchange, two-state two state mechanism contributes significantly to the observed R1 rate in biologic tissues. It is reviewed nicely by Fullerton et al [18] while an excellent summary of the literature is given in [19]. In short, tissue water can be thought to consist of two populations: free water that exists in the extracellular space and bound water that is attracted to cellular structures through the non-uniform electric polarity of the water molecules. While these two populations may exist in the same cellular volume, their differences in boundedness allow for very different ranges of possible rotational rates and each population returns to equilibrium at distinctly different R1 rates. However, over the course of an MR experiment, these two populations rapidly exchange hydrogen protons via chemical exchange and diffusion. This exchange converts the observed R1 rate into a weighted sum of the two distinct R1 rates of each population. Tissues whose structures



promote different relative fractions of free and bound water display different R1 relaxation rates.

We envision two possible ways by which histotripsy can influence R1. The first is by influencing the fast-exchange, two-state mechanism. The breakup of cellular tissue may change both the volume of water loosely bound to cellular proteins and lipids and the rotation rate of the now broken up subcellular structures. Both of these effects can conspire to increase the R1 rate. This effect would be seen most strongly in tissues that do not contain many paramagnetic substances.

The second means by which histotripsy may influence R1 is by changing the access of water to paramagnetic proteins. For example, during the breakdown of stationary blood, the hemoglobin within a red blood cell turns into methemoglobin. As mentioned above, methemoglobin can greatly enhance the R1 rate of water. However, when bound in the red blood cell, extracellular water must first pass through the cell membrane before undergoing any interaction with the methemoglobin. By breaking apart the red blood cell membrane, histotripsy would allow water molecules to more quickly interact with the magnetic field perturbations created by the methemoglobin, which will result in an enhanced R1 rate.

There are, potentially, other means by which histotripsy can change the R1 rate of tissues. However, these consist of changing the magnetic state of paramagnetic proteins, changing the temperature or viscosity of free water, or changing the size of water molecules. There has, so far, been no evidence that the histotripsy bubble cloud is capable of effecting chemical changes on such small levels.

#### **4.3.2 Results**

The estimated R1 rates from the materials ablated in this study are displayed in Fig (4.4). The R1 rates estimated in liver, kidney, muscle, and brain all remained insensitive to ablation by histotripsy. Meanwhile, the R1 rates estimated in the clot and RBC phantoms all decreased with ablation, with clot showing the largest change in rate.

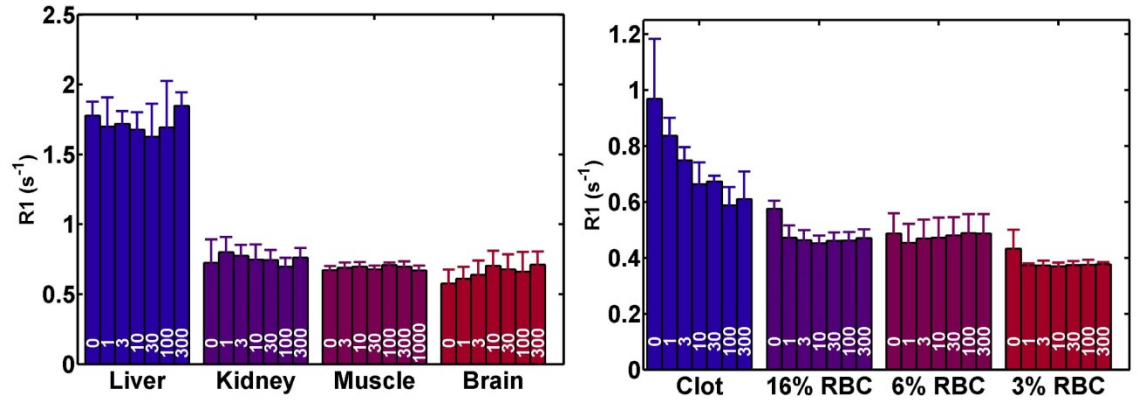


**Figure 4.3: Means and standard deviations of the estimated R1 rates of lesions made in the materials tested in this study. Materials are separated by color and are labeled on the x-axis. The number of acoustic pulses deposited per grid point in each lesion is labeled in white on each bar. The estimated R1 rates of liver, kidney, muscle and brain appear to be invariant to ablation by histotripsy. However, the R1 rates of clot and all three red blood cell phantoms display sensitivity to ablation, possibly because of the release of methemoglobin when the blood cells are lysed.**

### 4.3.3 Discussion

As discussed in section 4.3.1, the fast-exchange, two-state mechanism is thought to play a strong role in the variance of R1 rates between biologic tissues. It is possible for histotripsy to affect this mechanism by breaking up large aggregations of molecules, such as a cell membrane. Broken molecules have a smaller size and likely rotate more quickly which would then affect the rotation rate of the associated bound water molecules. However, the results of our experiments indicate that the R1 rates of tissues do not change with ablation by histotripsy. This suggests that homogenization of cellular tissue does not disrupt the fast-exchange, two state mechanism.

Histotripsy does, however, appear to reduce the R1 rate of blood clots and red blood cell based phantoms. In the literature, similar results were reported in references [20], [21] at 1.5 T, though the magnitude of differences in R1 rate between whole blood and blood lysate were quite small and varied with pH and hematocrit. In contrast, another group has reported R1 to increase with RBC lysis at field strengths of 0.2 to 1.4 T [22], [23]. The absolute differences reported by these references vary widely. We have not found an experiment comparing the R1 of lysed blood to intact blood at higher fields such as 7T.

We are unclear why R1 should decrease for lysed RBC's in gel based phantoms in our study or why lysing RBC's should optionally decrease or increase as reported in the cited literature. Many qualitative [17] and quantitative [16], [24], [25] theories of MR relaxation in

blood attribute changes in R1 to the degradation of hemoglobin to methemoglobin and do not attribute an explicit dependence on cell integrity. However, cell lysis should release the bound proteins into the extracellular space, increasing the rate at which water will interact with the methemoglobin. This should increase the R1 rate of histotripsy lesions--the opposite behavior observed in our experiments.

## **4.4 Transverse Relaxation (R2)**

### **4.4.1 Mechanism**

As mentioned in chapter 1, R2 is the rate at which the observed MR signal decays. This decay occurs as magnetic moments accrue some phase relative to the other moments within the system. Some of this phase is caused by the same fluctuating fields that drive longitudinal relaxation. However, unlike, longitudinal relaxation, transverse relaxation is further enhanced when different magnetic moments experience field fluctuations at frequencies less than the Larmor frequency. Thus, the R2 rate of a tissue is almost always larger than its R1 rate.

Low frequency magnetic field fluctuations can be caused by the motion of nearby magnetic moments [11], [14], [26], the introduction of paramagnetic particles [12], [14], chemical bonding [27], [28], inhomogeneities in the magnetic field that can be either purposefully caused by the user or form by accident, and the diffusion of water through these fields [29], [30]. In addition, the R2 rate of biologic tissues can be influenced by the fast-exchange, two-state mechanism.

Histotripsy can potentially alter the R2 rate of tissues by changing the ratio of free water to bound water, changing the inhomogeneity of the magnetic field by homogenized materials with an inhomogenous distribution of magnetic susceptibility, and by changing the magnetic state of paramagnetic particles.

### **4.4.2 Results**

The estimated R2 rates from the treated materials are displayed in Fig (4.5). With the exception of brain, the R2 rates of all tissues tested here decreased in response to histotripsy treatment. The R2 rate of brain tissue appeared to increase slightly with treatment. Clot demonstrated the most dramatic change with its R2 rate decreasing to about 5% of the nominal rate. It is then followed by liver, the RBC phantoms, kidney, and then muscle.

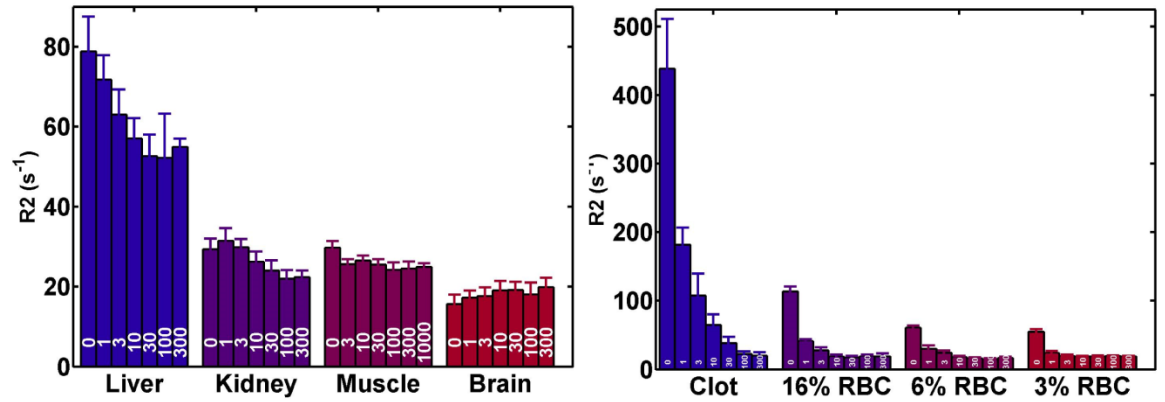


**Figure 4.4: Means and standard deviations of the estimated R2 rates of lesions made in the materials tested in this study. Materials are separated by color and are labeled on the x-axis. The number of acoustic pulses deposited per grid point in each lesion is labeled in white on each bar. With the exception of brain, the estimated R2 rates of all materials tested here decrease with ablation. The magnitude to change in R2 rates varies dramatically between tissue type, with the R2 rate of clot responding particularly strongly. The R2 rate of brain appears to increase, which is likely due to partial volume effects and poor discrimination between white and grey matter.**

#### 4.4.3 Discussion

The R2 rates in all the materials tested here appear to change in response to histotripsy. This response is sensitive to number of pulses that are applied to the target material. Further, for liver, kidney, muscle, clot, and the RBC phantoms, the apparent rate at which R2 changes with pulse number decreases with increasing amounts of ablation. This trend is very similar to other estimates of histotripsy homogenization such as color Doppler imaging [31], ultrasonic backscatter reduction [32], [33], and ultrasonically estimated elastography [34]. R2 weighted imaging may be an excellent method for estimating histotripsy ablation.

The materials tested here also display significant variation in the magnitude at which the R2 rate decreases in response to ablation. These differences may be related to the concentration of iron stored in each tissue. In the RBC phantoms, the degree to which the R2 rate reduces because of ablation scales with the density of the suspended red blood cells. Similarly, the degree to which the R2 rates of liver, kidney, muscle, and brain tissue all change correlates with tissue iron concentration. In Fig. (4.6) we have plotted reported concentrations of iron in porcine liver, kidney, muscle, and human brain cortex [35]–[42] alongside the observed difference in R2 between nominal tissue and the lesions treated with the largest number of acoustic pulses. For liver, kidney and muscle, the total change in R2 caused by histotripsy decreases with decreasing tissue iron concentration.

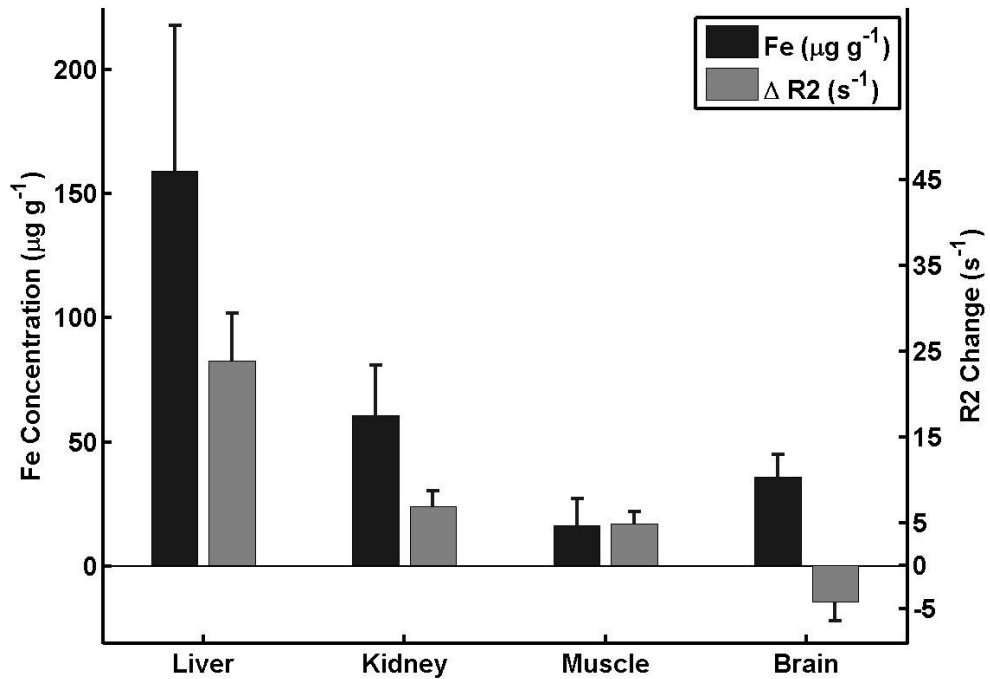


**Figure 4.5: Dark Bars: Mean and standard deviation of iron concentration found in the literature (Refs 35-42) in porcine liver, kidney, muscle. White Bars: Mean and standard deviation of the change in R2 rate between nominal and maximally treated porcine liver, kidney, muscle and brain tissues. There is a correlation between iron content and the magnitude of change in R2 rate that accompnys histotripsy ablation in liver, kidney, and muscle. The poor correlation between the change in R2 rate and iron concentration in brain tissue may be caused by, 1, a bias in iron concentration estimation that represents older, more iron laden brains, and, 2, partial volume effects that have skewed the measured R2 in lesions in brain to include both white and grey matter.**

The apparent increase in R2 rate observed in the brain samples is more difficult to interpret and is likely caused by a mismatch in the iron concentrations reported in the literature and those that actually exist in the samples used here. The concentrations of brain iron reported in references [35],[36],[37] and [42] originate from either 30-40 year old adults [36], [42], humans over 60 years old [35], or an average of concentrations found in humans ranging from 0 to 100 years old [37]--all of which results in an average more heavily weighted by older subjects. Brain iron increases with age [37], [43], which will make the resulting average iron concentration skewed toward larger values. Further, there is considerable variation in reported iron concentrations within the literature [44] due, in part, to differences in the methods used to estimate tissue iron. Meanwhile, the bovine samples tested here are from an animal no more than 3 years old. It is quite possible that the iron levels reported in the literature are larger much than that found the bovine brain tested here.

In addition, these results also do differentiate between grey and white matter, which may have different responses to histotripsy and contain different organizations of iron.

The influence of iron on the R2 rate of histotripsy lesions will be examined in more depth in Chapter 5.

## **4.5 Diffusion (ADC)**

### **4.5.1 Mechanism**

The thermal energy of any mass of water causes the individual molecules within the mass to translate and collide, forming tortuous, random paths throughout the volume. The apparent diffusion coefficient (ADC) characterizes this process and is an estimate of the average squared distance over which individual water molecules will drift during a given span of time. The ADC is heavily influenced by cellular structure. Cell membranes impede the diffusion of water, thus reducing the estimated ADC in tissues compared to values obtained in bulk water. Histotripsy can potentially increase the ADC of a tissue by breaking apart membrane barriers, allowing water to more freely diffuse through the volume.

### **4.5.2 Results**

The estimated ADC values from the treated materials are displayed in Fig (4.6). In every case, the ADC values increased quite significantly in response to histotripsy treatment. For example, the ADC found in liver, kidney, and muscle displayed an increase of nearly 300% when exposed to histotripsy, while the ADC found in clot increased by more than 400% after exposure. Meanwhile, the ADC found in muscle increased by about 50% after exposure to histotripsy. The change in ADC observed in the RBC phantoms was considerably less than that found in the other materials and decreased with decreasing concentration of red blood cells.

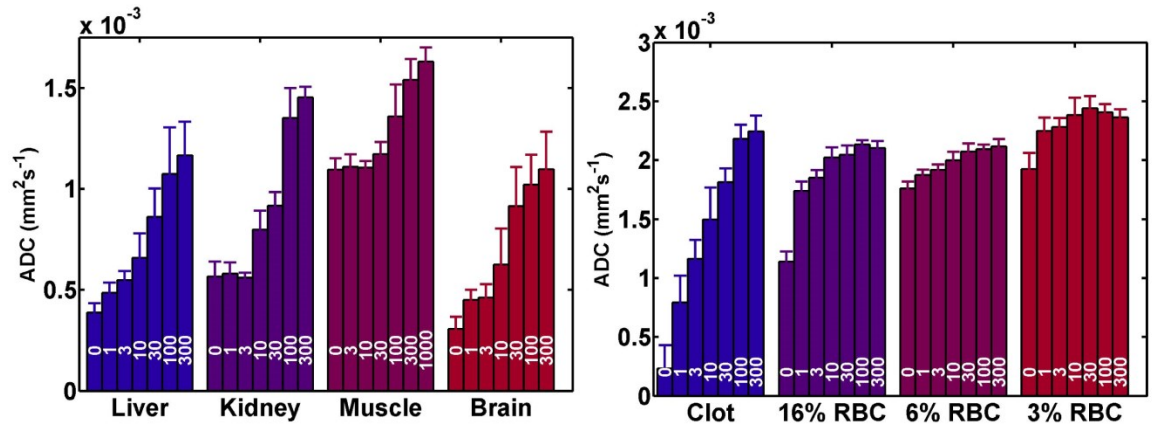


**Figure 4.6: Means and standard deviations of the estimated ADC values of lesions made in the materials tested in this study. Materials are separated by color and are labeled on the x-axis. The number of acoustic pulses deposited per grid point in each lesion is labeled in white on each bar. The ADC value of all materials tested here increase in response to ablation by histotripsy. This is likely because histotripsy breaks apart cellular membranes, allowing water to more freely diffuse through the material.**

### 4.5.3 Discussion

The estimated ADC in many tissues is largely determined by the lipid membranes. Histotripsy is well known for breaking apart cellular membranes [45]. The large increases in diffusivity observed during these experiments indicate how thoroughly histotripsy is able to break apart cellular membranes. In addition, the ADC of treated tissues increases as increasing numbers of pulses are applied to the target material. Like the R2 rates reported here, this increase tapers off and asymptotically approaches a final value.

## 4.6 In Vivo Lesion

### 4.6.1 Introduction

The above studies were made in ex vivo tissues and tissue mimicking phantoms. These materials were not vascularized and, thus, could not mount hemorrhagic and edemic responses to ablation. R1, R2, and ADC weighted MR images are sensitive to both hemorrhage and edema, which can introduce confounding contrast in images of histotripsy lesions. This section reports a small study that examines to what degree hemorrhagic or edemic effects can influence the R1, R2, and ADC of liver tissue that is exposed in vivo to histotripsy.

#### 4.6.2 Methods

In vivo ablation was performed using a porcine liver model. Histotripsy was applied to the liver of 1 healthy mixed breed pig with a weight of ~100 pounds following the previously developed experimental set-up described in [5], [6]. After anesthetization and intubation, the pig was placed in a dorsal recumbent position on the surgical table and the skin over the targeted tissue was treated with a depilatory cream. To ensure ultrasound propagation to the targeted tissue, a degassed water bolus was placed on the chest of the animal. The bowl holding the bolus contained an open cutout to allow the propagation of ultrasound and was lined with an adhesive surgical drape to provide a water-tight seal against the skin of the pig and prevent leakage.

To apply histotripsy to the liver, a 700 kHz histotripsy therapy transducer with an 11 cm focal distance was aligned on the pig chest. A schematic of this setup is shown in Fig. (4.7). An 8 MHz phased array ultrasonic imaging probe (Model S8, used with Sonos 7500 imaging system, Philips Electronics, Andover, MA) was fixed to the histotripsy therapy transducer in order to allow real-time image-guidance. Ultrasound pulses were applied from the transducer outside the chest and focused to the target location in the liver using 5-cycle histotripsy pulses at a pulse repetition frequency (PRF) of 50 Hz and an estimated in situ peak negative pressure of ~16-20 MPa. Histotripsy was applied to the target location for 15 minutes. During treatment, the focus of therapy transducer was mechanically moved to follow a 5×3 mm grid in the directions transverse to acoustic propagation. Each point in the grid was treated for 1 minute (3,000 pulses) before the focus was moved to an adjacent location. After treatment, the pigs were euthanized without recovery and the liver was harvested for MR imaging.



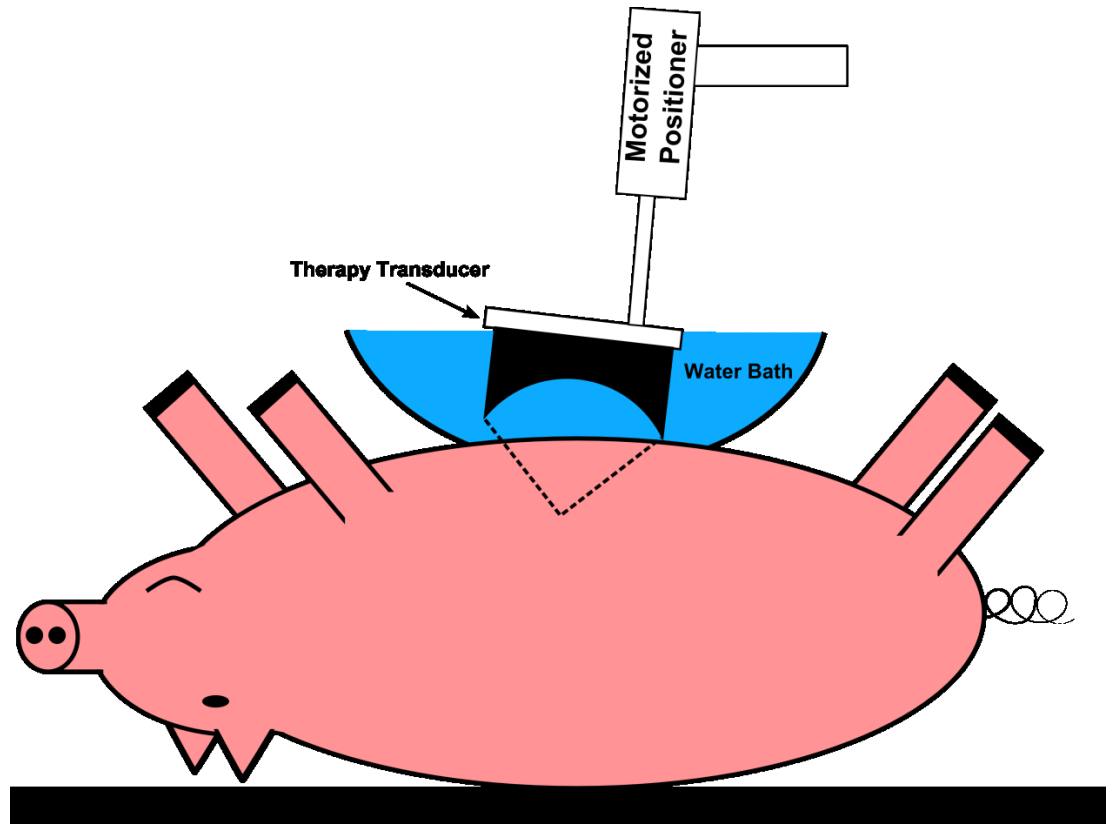


**Figure 4.7: Setup of in vivo ablation of porcine liver. Ultrasound was delivered trans-abdominally for 15 minutes with a PRF of 50 Hz. A water bolus was used to couple the therapy transducer to the target. During treatment the transducer was mechanically scanned through a grid pattern, depositing 3000 pulses per point. After treatment, the liver was excised and imaged.**

MR images were acquired using the same setup as reported in section 4.2.3 and imaging parameters are reported in table 4.1. Estimates of R1, R2, and the ADC of the lesion and the surrounding nominal liver were computed by performing pixel-by-pixel least squares fits to equations 4.1-4.3.

### 4.6.3 Results

An R2-weighted image of the lesion made in in vivo porcine liver is shown in Fig. (4.8) along with R1, R2, and ADC Maps of the same image slice. The homogenate displayed strong R2 contrast and correlated with large changes in R2 and the ADC when compared to the surrounding nominal liver. A thin rim of hemorrhage presenting as a dark R2-weighted boundary was observed to surround the lesion. Outside of this rim was a second, very faint ring of edema. The R1 map indicated some change in R1 within the lesion, though this

pattern did not correlate strongly with the observed lesion morphology in the R2 and ADC maps.

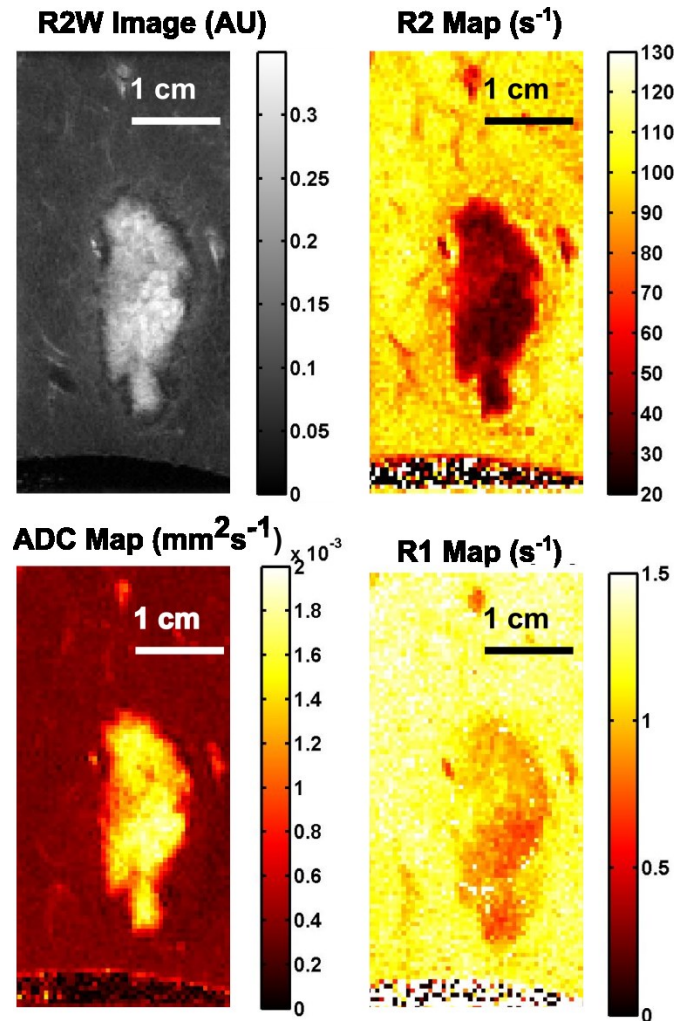


**Figure 4.8:** An R2-weighted image (R2W) and corresponding R2, ADC, and R1 maps of the lesion formed in in vivo porcine liver. The lesion displays a large change in R2 and ADC and a much less well defined change in R1. These features match well to the results in ex vivo tissue displayed above. However, some in vivo effects can be seen in the image: a small rim of hemorrhage can be observed surrounding the lesion, followed by another faint rim of edema, and the R2 and ADC contrast within the lesion is not uniform.

#### 4.6.4 Discussion

The observed R2 and ADC of liver tissue ablated in vivo behave similar to the R2 and ADC of liver ablated ex vivo. The measured ADC of the treated and nominal in vivo liver match well to the measured ex vivo ADC. However, there are some distinct differences between the appearance of the lesions formed in vivo and those formed ex vivo. The R2 of the nominal in vivo liver is larger than that in the ex vivo case while the R2 in the in vivo

lesion is smaller than that in the ex vivo case. Unlike the ex vivo case, the in vivo liver lesion displays hemorrhage and edema surrounding the lesion border and some inhomogeneity within the lesion center. Lastly, the R1 of the in vivo lesion displays some change in response to ablation.

These results suggest that the responses of MR contrast parameters to histotripsy lesions formed in vivo can be expected to generally follow the responses presented in this chapter of lesions formed in ex vivo. However, in vivo effects such as blood flow, edema, and the decay process of hemoglobin can also play a role in the contrast of histotripsy lesions.

## 4.7 Study Limitations

There are many known MR imaging non-idealities that contribute to estimation error when quantifying MR contrast parameters. These include RF inhomogeneities, imperfect slice profiles, inadvertent weighting by another contrast mechanism, partial volume effects, temperature variations, low SNR, and, importantly, poorly sampling the contrast curve by either acquiring too few points or too few points on the part of the curve with the steepest slope [46].

This study has features that minimize many but not all of these effects. Using long TR times prevents the inadvertent formation of steady state signals during experimentation—which can lead to T1 and T2 contamination. Using a single Hahn spin echo for each measurement reduced the sensitivity of the measurement to an imperfect slice profile. The temperature of the sample was moderated by the large air bolus in the room. Lastly, except for the case of untreated clot, the decay curve parameters  $ti$ ,  $te$ , and  $b$  were all chosen to maintain good SNR in the selected ROIs.

However, this study remains susceptible to possible errors caused by partial volume effects and non-ideal sampling of the contrast curves. For example, many tissues exhibit multi-exponential R2 relaxation and multi-compartment diffusion. Multi-exponential R1 relaxation rates are less commonly observed but are still possible [19]. The five echo times and 4 diffusion b-values acquired in this study are too few to extract multiple decay constants. Thus, what might otherwise be truly multi-exponential signal decay is constrained into a single decay curve.

Further, if the R1, R2, and ADC decay curves are not well sampled, Equations 4.1-3 may not reliably converge on the true contrast value given small variations in the acquired observations. This sort of error can be observed in the estimations of R2 rates of untreated clot and liver. In these cases, echo times were chosen to more optimally sample the R2 relaxation curve of the treated lesions, resulting in longer echo times. Thus, while the five acquired images have good SNR for the treated lesions, two to three of the images of the background tissue have very low SNR. The resulting unstable fits lead to the larger width of the error bars for untreated liver and clot in Figs (4.4-4.6). Meanwhile, partial volume effects, for example in the brain where we did not differentiate between grey and white matter, lead to contrast constants that are averaged together. This can mask the true response of each tissue type to histotripsy.

In summation, error contamination in MR parameter estimation is a common difficulty in the reported literature. This study was able to mitigate many of these errors by being more susceptible to error caused by the number and spacing of samples along the relevant signal decay curves. However, the estimation errors that may be present in this study do not detract from its most useful results: R2 and the ADC in a variety of tissues and phantom materials respond to histotripsy ablation. Though exact parameter numbers in this and most other parameter measurement studies are subject to some scrutiny, the response of the parameters to ablation is reliable.

## 4.8 Conclusion

In this study we survey the response of the estimated R1, R2, and ADC parameters in histotripsy lesions made in a variety of tissues and tissue mimicking phantoms. The ADC of these materials increased in all reported materials as the number of deposited acoustic pulses in each lesion was increased. The R2 rate decreased in all reported materials as the number of deposited acoustic pulses increased. However, the degree to which the R2 rate changed correlated with the iron content of the materials. Lastly, the R1 rate did not appear to vary with ablation in liver, kidney, muscle, and brain tissues. However, it did decrease in clot and the RBC phantoms as the number of deposited acoustic pulses increased.

The behavior of R1, R2, and the ADC of a liver lesion formed in an in vivo porcine model matches the behavior of these parameters observed in lesions made in ex vivo porcine liver. However, bleeding and edema did form rings of alternating diminished and enhanced

R2 about the homogenized lesion. These results suggest that the ex vivo behavior of R1, R2, and the ADC can form a basis of understanding for MR guided histotripsy that should help the radiologist separate image features caused by homogenization and those caused by in vivo effects.

## 4.9 References

- [1] A. Partanen, N. Farr, W. Kreider, T. Khokhlova, A. Maxwell, Y.-N. Wang, M. Bailey, and V. Khokhlova, "Use of MRI to visualize mechanically fractionated lesions generated by boiling histotripsy in tissue," in *Abstract Book of 14th International Symposium for Therapeutic Ultrasound*, 2014.
- [2] T. L. Hall, G. R. Lee, L. Hernandez, and C. A. Cain, "Relaxation properties of cavitation induced tissue lesions," in *Proceedings of the 15th Annual Meeting of ISMRM*, 2007, p. 1118.
- [3] S. P. Allen, W. W. Roberts, T. L. Hall, C. A. Cain, and L. Hernandez, "Characterization of in vivo histotripsy lesions using high field MRI," in *Proceedings of the 20th Annual Meeting of ISMRM*, 2012, p. 1582.
- [4] E. Vlaisavljevich, Y. Kim, G. Owens, W. Roberts, C. Cain, and Z. Xu, "Effects of tissue mechanical properties on susceptibility to histotripsy-induced tissue damage.," *Phys. Med. Biol.*, vol. 59, no. 2, pp. 253–70, 2014.
- [5] E. Vlaisavljevich, Y. Kim, S. P. Allen, G. Owens, S. Pelletier, C. A. Cain, K. Ives, and Z. Xu, "Image-guided non-invasive ultrasound liver ablation using histotripsy: feasibility study in an in vivo porcine model," *Ultrasound Med. Biol.*, vol. 39, no. 8, pp. 1398–1409, 2013.
- [6] Y. Kim, E. Vlaisavljevich, G. E. Owens, S. P. Allen, C. A. Cain, and Z. Xu, "In vivo transcostal histotripsy therapy without aberration correction," *Phys. Med. Biol.*, vol. 59, no. 11, pp. 2553–2568, Jun. 2014.
- [7] Y. Kim, C. G. Fifer, S. K. Gelehrter, G. E. Owens, D. R. Berman, E. Vlaisavljevich, S. P. Allen, M. F. Ladino-Torres, and Z. Xu, "Developmental impact and lesion maturation of histotripsy-mediated non-invasive tissue ablation in a fetal sheep model," *Ultrasound Med. Biol.*, vol. 39, no. 6, pp. 1047–1055, Jun. 2013.
- [8] M. Hoogenboom, D. Eikelenboom, M. H. den Brok, A. Veltien, M. Wassink, P. Wesseling, E. Dumont, J. J. Fütterer, G. J. Adema, and A. Heerschap, "In vivo MR guided boiling histotripsy in a mouse tumor model evaluated by MRI and histopathology.," *NMR Biomed.*, no. February, Apr. 2016.
- [9] J. Sukovich, Z. Xu, Y. Kim, H. Cao, T.-S. Nguyen, A. Pandey, T. Hall, and C. Cain, "Targeted Lesion Generation Through the Skull Without Aberration Correction Using Histotripsy," *IEEE Trans. Ultrason. Ferroelectr. Freq. Control*, vol. 3010, no. c, pp. 1–1, 2016.
- [10] J. C. Lagarias, J. A. Reeds, H. Wright, and P. E. Wright, "Convergence properties of the nelder–mead simplex method in low dimensions," *J. Optim.*, vol. 9, no. 1, pp. 112–

- 117, 1998.
- [11] N. Bloembergen, E. M. Purcell, and R. V. Pound, "Relaxation Effects in Nuclear Magnetic Resonance Absorption," *Phys. Rev.*, vol. 73, no. 7, pp. 679–712, Apr. 1948.
  - [12] N. Bloembergen and L. O. Morgan, "Proton Relaxation Times in Paramagnetic Solutions. Effects of Electron Spin Relaxation," *J. Chem. Phys.*, vol. 34, no. 3, p. 842, 1961.
  - [13] M. H. Mendonça-Dias, E. Gaggelli, and P. C. Lauterbur, "Paramagnetic contrast agents in nuclear magnetic resonance medical imaging," *Semin. Nucl. Med.*, vol. 13, no. 4, pp. 364–376, Oct. 1983.
  - [14] I. Solomon, "Relaxation Processes in a System of Two Spins," *Phys. Rev.*, vol. 99, no. 2, pp. 559–565, Jul. 1955.
  - [15] Y. Gossuin, R. N. Muller, and P. Gillis, "Relaxation induced by ferritin: A better understanding for an improved MRI iron quantification," *NMR Biomed.*, vol. 17, no. 7, pp. 427–432, 2004.
  - [16] R. A. Brooks and G. Di Chirio, "Magnetic resonance imaging of stationary blood: A review," *Med. Phys.*, vol. 14, no. 6, p. 903, 1987.
  - [17] W. G. Bradley, "MR appearance of hemorrhage in the brain," *Radiology*, vol. 189, no. 1, pp. 15–26, 1993.
  - [18] G. D. Fullerton, J. L. Potter, and N. C. Dornbluth, "NMR relaxation of protons in tissues and other macromolecular water solutions," *Magn. Reson. Imaging*, vol. 1, no. 4, pp. 209–226, 1982.
  - [19] P. A. Bottomley, T. H. Foster, R. E. Argersinger, and L. M. Pfeifer, "A review of normal tissue hydrogen NMR relaxation times and relaxation mechanisms from 1–100 MHz: Dependence on tissue type, NMR frequency, temperature, species, excision, and age," *Med. Phys.*, vol. 11, no. 4, p. 425, Jul. 1984.
  - [20] J. Bass, H. D. Sostman, O. Boyko, and J. a Koepke, "Effects of cell membrane disruption on the relaxation rates of blood and clot with various methemoglobin concentrations," *Investigative radiology*, vol. 25, no. 11. pp. 1232–7, 1990.
  - [21] P. a. Janick, D. B. Hackney, R. I. Grossman, and T. Asakura, "MR imaging of various oxidation states of intracellular and extracellular hemoglobin," *Am. J. Neuroradiol.*, vol. 12, no. 5, pp. 891–897, 1991.
  - [22] J. M. Gomori, R. I. Grossman, C. Yu-IP, and T. Asakura, "NMR Relaxation Times of Blood: Dependence on Field Strength, Oxidation State, and Cell Integrity," *J. Comput. Assist. Tomogr.*, vol. 11, no. 4, pp. 684–690, 1987.
  - [23] J. M. Gomori and R. I. Grossman, "Mechanisms responsible for the MR appearance and evolution of intracranial hemorrhage," *Radiographics*, vol. 8, no. 3, pp. 427–440, 1988.
  - [24] K. Grgac, P. C. M. van Zijl, and Q. Qin, "Hematocrit and oxygenation dependence of blood (1)H(2)O T(1) at 7 Tesla," *Magn. Reson. Med.*, vol. 70, no. 4, pp. 1153–9, Oct. 2013.
  - [25] W. Li, K. Grgac, A. Huang, N. Yadav, Q. Qin, and P. C. M. M. van Zijl, "Quantitative theory for the longitudinal relaxation time of blood water," *Magn. Reson. Med.*, vol. 00, no. May, p. n/a–n/a, Aug. 2015.

- [26] N. Bloembergen, "Spin Relaxation Processes in a Two-Proton System," *Phys. Rev.*, vol. 104, no. 6, pp. 1542–1547, Dec. 1956.
- [27] Z. Luz and S. Meiboom, "Nuclear Magnetic Resonance Study of the Protolysis of Trimethylammonium Ion in Aqueous Solution—Order of the Reaction with Respect to Solvent," *J. Chem. Phys.*, vol. 39, no. 2, pp. 366–370, 1963.
- [28] A. Allerhand and H. S. Gutowsky, "Spin—Echo NMR Studies of Chemical Exchange. I. Some General Aspects," *J. Chem. Phys.*, vol. 41, no. 7, pp. 2115–2126, 1964.
- [29] J. H. Jensen and R. Chandra, "NMR relaxation in tissues with weak magnetic inhomogeneities.," *Magn. Reson. Med.*, vol. 44, no. 1, pp. 144–56, Jul. 2000.
- [30] H. Y. Carr and E. M. Purcell, "Effects of Diffusion on Free Precession in Nuclear Magnetic Resonance Experiments," *Phys. Rev.*, vol. 94, no. 3, pp. 630–638, May 1954.
- [31] X. Zhang, R. M. Miller, K.-W. Lin, A. M. Levin, G. E. Owens, H. S. Gurm, C. A. Cain, and Z. Xu, "Real-time feedback of histotripsy thrombolysis using bubble-induced color Doppler.," *Ultrasound Med. Biol.*, vol. 41, no. 5, pp. 1386–401, May 2015.
- [32] T. L. Hall, J. B. Fowlkes, and C. A. Cain, "A real-time measure of cavitation induced tissue disruption by ultrasound imaging backscatter reduction," *IEEE Trans. Ultrason. Ferroelectr. Freq. Control*, vol. 54, no. 3, pp. 569–575, Mar. 2007.
- [33] T.-Y. Y. Wang, Z. Xu, F. Winterroth, T. L. Hall, J. B. Fowlkes, E. D. Rothman, W. W. Roberts, and C. A. Cain, "Quantitative ultrasound backscatter for pulsed cavitation ultrasound therapy-histotripsy," *IEEE Trans. Ultrason. Ferroelectr. Freq. Control*, vol. 56, no. 5, pp. 995–1005, May 2009.
- [34] T. Y. Wang, T. L. Hall, Z. Xu, J. B. Fowlkes, and C. A. Cain, "Imaging feedback of histotripsy treatments using ultrasound shear wave elastography," *IEEE Trans. Ultrason. Ferroelectr. Freq. Control*, vol. 59, no. 6, pp. 1167–1181, 2012.
- [35] P. Riederer, E. Sofic, W. D. Rausch, B. Schmidt, G. P. Reynolds, K. Jellinger, and M. B. Youdim, "Transition metals, ferritin, glutathione, and ascorbic acid in parkinsonian brains.," *J. Neurochem.*, vol. 52, no. 2, pp. 515–20, Feb. 1989.
- [36] C. Langkammer, N. Krebs, W. Goessler, E. Scheurer, F. Ebner, K. Yen, F. Fazekas, and S. Ropele, "Quantitative MR Imaging of Brain Iron : A Postmortem Validation Study," *Radiology*, vol. 257, no. 2, pp. 455–462, Nov. 2010.
- [37] B. Hallgren and P. Sourander, "The effect of age on the non-haemin iron in the human brain.," *J. Neurochem.*, vol. 3, no. 1, pp. 41–51, Oct. 1958.
- [38] M. López-Alonso, M. Miranda, C. Castillo, J. Hernández, M. García-Vaquero, and J. L. Benedito, "Toxic and essential metals in liver, kidney and muscle of pigs at slaughter in Galicia, north-west Spain.," *Food Addit. Contam.*, vol. 24, no. 9, pp. 943–54, Sep. 2007.
- [39] J. Falandysz, "Some toxic and essential trace metals in swine from Northern Poland," *Sci. Total Environ.*, vol. 136, no. 1–2, pp. 193–204, Aug. 1993.
- [40] R. Kongkachuichai, P. Napatthalung, and R. Charoensiri, "Heme and nonheme iron content of animal products commonly consumed in Thailand," *J. Food Compos. Anal.*, vol. 15, no. 4, pp. 389–398, Aug. 2002.
- [41] M. E. Coleman, R. S. Elder, P. Basu, and G. P. Koppelaar, "Trace metals in edible

- tissues of livestock and poultry,” *J. AOAC Int.*, vol. 75, no. 4, Jul. 1992.
- [42] D. A. Loeffler, J. R. Connor, P. L. Juneau, B. S. Snyder, L. Kanaley, A. J. DeMaggio, H. Nguyen, C. M. Brickman, and P. A. LeWitt, “Transferrin and Iron in Normal, Alzheimer’s Disease, and Parkinson’s Disease Brain Regions,” *J. Neurochem.*, vol. 65, no. 2, pp. 710–716, Nov. 2002.
- [43] B. Drayer, P. Burger, R. Darwin, S. Riederer, R. Herfkens, and G. A. Johnson, “Magnetic Resonance Imaging of Brain Iron,” *AJNR Am. J. Neuroradiol.*, vol. 7, no. 3, pp. 373–380, May 1986.
- [44] E. M. Haacke, N. Y. C. C. Cheng, M. J. House, Q. Liu, J. Neelavalli, R. J. Ogg, A. Khan, M. Ayaz, W. Kirsch, and A. Obenaus, “Imaging iron stores in the brain using magnetic resonance imaging,” *Magn. Reson. Imaging*, vol. 23, no. 1, pp. 1–25, Jan. 2005.
- [45] V. A. Khokhlova, J. B. Fowlkes, W. W. Roberts, G. R. Schade, Z. Xu, T. D. Khokhlova, T. L. Hall, A. D. Maxwell, Y.-N. Wang, and C. A. Cain, “Histotripsy methods in mechanical disintegration of tissue: Towards clinical applications,” *Int. J. Hyperth.*, vol. 31, no. 2, pp. 145–162, Mar. 2015.
- [46] E. M. Haacke, R. W. Brown, M. R. Thompson, and R. Venkatesan, *Magnetic Resonance Imaging: Physical Principles and Sequence Design*, vol. 1st. 1999.



## Chapter 5:

# On The Origin of T2 Contrast in Histotripsy Lesions

### 5.1 Introduction

Histotripsy is well suited for the ablation of abdominal tissues. Histotripsy bubble clouds form precise lesions in deep abdominal organs [1]–[4] even when the acoustic beam is partially blocked by rib bone [5]. Further, transcostal ablation can rapidly liquefy large volumes of liver tissue while depositing a negligible thermal dose to the overlying rib structure [3]. Lastly, histotripsy ablation spares large vessels in the liver, preventing large scale hemorrhage within the lesion and the formation of ischemia in untreated regions [4].

Image guidance during the application of transabdominal histotripsy can improve therapy outcomes by monitoring the ablative state of the target and the surrounding tissues. Ultrasound based feedback methods include backscatter reduction [6], [7], Doppler imaging [8], and elastography [9]. These methods are relatively inexpensive and have high temporal resolution. However, they also suffer from an inability visualize more than one plane, and have reduced sensitivity when visualizing tissues at depth. MRI based feedback methods include cavitation sensitized imaging [10], [11], diffusion weighted imaging [12], and T2 weighting imaging [4], [13]–[17]. Though MR-based methods suffer from high costs, poor temporal resolution, and motion sensitivity, they do offer excellent image contrast, 3D acquisition, and sensitivity in deep tissues.

Of the MR methods listed above, T2 weighted imaging is well suited for abdominal applications of histotripsy—both because T2 weighted imaging sequences are often less sensitive to respiratory motion and because histotripsy lesions display excellent T2 weighted contrast in abdominal organs. As chapter 4 has shown, the  $1/T_2$  rate of histotripsy lesions in liver, kidney, and muscle all increase with ablation. As a result, a properly designed T2 weighted sequence can lead to useful lesion visualization [4], [16], [17]. However, the

mechanism behind T2 lengthening by histotripsy ablation has not yet been explored. Understanding this mechanism can lead to better imaging sequence design and more efficient feedback. This paper seeks to better understand this mechanism.

There are several possible means by which the T2 time of tissue may lengthen. These include an increase in the ratio of free water to bound water, a shortening of the rotational correlation times of various proteins, decreased water access to paramagnetic particles in the lesion, changes to the paramagnetic state of iron bearing proteins, increased uniformity to the microscopic magnetic field, and increased diffusivity of water through an inhomogeneous magnetic field. Meanwhile, as shown in Chapter 4 and in reference [11], the degree to which T2 changes due to histotripsy ablation varies between tissue types. Tissues that contain larger concentrations of iron also display a larger change in T2 when liquefied by histotripsy. Further, tissue iron is also known to correlate with the observed T2 relaxation in intact brain [18], liver [19], and kidney [20]. In general, greater concentrations of iron in intact tissue result in a greater shortening of the observed T2 time.

These observations lead us to suppose that the T2 lengthening observed in ablated abdominal tissues is caused by histotripsy removing the mechanism behind iron-induced T2 shortening. When iron makes a small contribution to the overall T2 time of a nominal tissue, then ablation by histotripsy produces a proportionally small change to the observed T2 time. In this paper we will first review a few potential mechanisms by which tissue iron can shorten the T2 time of tissues. We then hypothesize how histotripsy can impact these mechanisms and test this hypothesis.

### **5.1.1 Tissue T2 Shortening by Iron**

Iron in tissues generally appears as either heme or non-heme iron. Heme refers to the heme-molecule that attaches iron to oxygenated and deoxygenated hemoglobin, methemoglobin, and myoglobin, among other proteins. The influence of heme iron on T2 is well studied and reviewed in detail in [21]–[23]. Briefly, the T2 of water is greatly shortened by the presence of paramagnetic heme iron such as what is found in deoxygenated hemoglobin and methemoglobin. Oxygenated hemoglobin, which has diamagnetic iron, has a very small impact on the T2 time of tissue and will not be addressed in this paper. Our subsequent references to hemoglobin will exclusively refer to paramagnetic forms of the protein. Methemoglobin shortens the T2 of tissue water through dipole-dipole interactions

between water hydrogen atoms and the paramagnetic iron atoms in its respective heme groups. Deoxygenated hemoglobin cannot take part in this process because its paramagnetic iron atoms are too well sequestered.

In addition to dipole interactions, both deoxyhemoglobin and methemoglobin further shorten T<sub>2</sub> through what is sometimes referred to as the “outer sphere mechanism” [24]. This mechanism relies on the bulk magnetic properties of aggregated hemoglobin to enhance the dephasing of the transverse MR signal. The magnetic susceptibility differences between the interior of red blood cells, which are densely packed with heme-proteins, and extracellular water create extracellular and intracellular magnetic field gradients. Water molecules are present within these gradients and their respective magnetic moments accrue phase relative to each other, leading to more rapid T<sub>2</sub> signal decay. Thermal diffusion of the water molecules—and possibly membrane transport—makes some portion of this decay unrecoverable by spin-echo.

There are three especially salient features of the outer sphere mechanism. First, the outer sphere mechanism will cause the 1/T<sub>2</sub> rate in a given sample to increase quadratically with magnetic field strength [25]–[29]. This behavior has been widely observed in blood and aqueous solutions of red blood cells [28]–[32]. Second, the observed T<sub>2</sub> time will vary strongly with the echo times used to make the observation [27]–[29], [31], [32]. When spin echoes are spaced closely together, there is less time for water to drift across the susceptibility-induced field gradients, which means that the relative phase accrued between different magnetic moments is more effectively reversed by the spin echoes [33]. When imaged with a train of spin echo pulses with short spacing between the echoes, a tissue’s signal will persist for a longer period of time than if it were imaged by a sequence using a longer spacing.

The third feature is that the above two behaviors only occur if the hemoglobin is packed into the red cells. Experimental observations have found that the observed T<sub>2</sub> time of blood lysate appears to be longer than that of its intact counterpart [29], [31], [34], [35]. It also appears to be independent of both field strength [31] and the echo times [29] used to make the measurement. It is thought that when blood cells are lysed, the hemoglobin is dispersed throughout the fluid volume, effectively negating the outer sphere mechanism by removing the field inhomogeneities caused by bulk susceptibility differences [31], [34].

Non-heme iron mainly appears in various forms of ferritin including transferrin and hemosiderin. Unlike hemoglobin, ferritin is simultaneously anti-ferromagnetic and paramagnetic. The observed T2 times of aqueous ferritin solutions increase linearly with magnetic field strength and are insensitive to the echo times used to make the measurement [32], [36]. A proton exchange model has been able to successfully predict these behaviors for aqueous solutions [37] but has difficulty making similar predictions in tissues.

In general, tissues with a given concentration of ferritin display shorter T2 times than equivalent aqueous solutions [38], [39]. In addition, the observed T2 of organs where ferritin is expected to make a large contribution to the transverse relaxation process exhibit a dependence on the echo times used to make the measurements [40], [41]—an effect not seen with aqueous ferritin. Observed echo time dependence and anomalously shortened T2 times in tissues are thought to be caused by the aggregation of ferritin within cells. Susceptibility differences between these aggregations and the surrounding bulk water then create sufficiently large field gradients to drive outer sphere T2 shortening. Indeed, in vitro experiments have shown that solutions of aggregated ferritin exhibit both shorter T2 times than their aqueous counterparts and a dependence on the echo time used to make the measurements [38], [42].

It is important to note that, while heme and non-heme iron have very different magnetic properties, both naturally appear in tissues in clustered form. And, in these clustered forms, both make contributions to T2 relaxation through the outer sphere mechanism. The tell-tale signs of this mechanism are a non-linear dependence of the observed T2 rate on both field strength and the echo times used to make the measurement.

### **5.1.2 Disruption by Histotripsy**

Our hypothesis is that ablation by histotripsy removes the outer sphere mechanism in tissues bearing aggregated ferritin and heme iron. One of the hallmarks of histotripsy is the complete homogenization of intracellular structures. The histotripsy bubble cloud introduces mechanical strains and high water velocities that break apart cell membranes. The water flow then disperses the internal contents throughout the lesions volume, producing a very fine homogenate [43], [44]. In abdominal tissues, it is possible that histotripsy breaks up and disperses aggregates of hemoglobin and ferritin, leaving the proteins themselves unchanged but more evenly distributed throughout the lesion volume. The disruption of

these aggregates would remove the influence of the outer sphere mechanism. With this mechanism removed, the observed T2 time of the ablated tissue should both increase relative to untreated tissue and no longer depend on field strength or echo time.

In this chapter, we test our hypothesis by examining the dependence of the  $1/T_2$  rate in ex vivo porcine tissue after it has been ablated by histotripsy. We then compare these results to those of a control sample.

## 5.2 Methods

### 5.2.1 Sample preparation

Liver was excised from a 50 kg pig and sliced into roughly 6 x 6 x 2 cm sections. These sections were then held for 3 hours under -25 mmHg vacuum while bathed in saline fluid to remove dissolved gasses from the tissue. After degassing, one section was vacuum sealed in a plastic bag (FoodSaver, Sunbeam Corporation, Boca Raton, FL). The bag was then attached to a 3-axes motorized positioning system and immersed in a water tank filled with degassed water along with the therapy transducer. A schematic of this setup is shown in

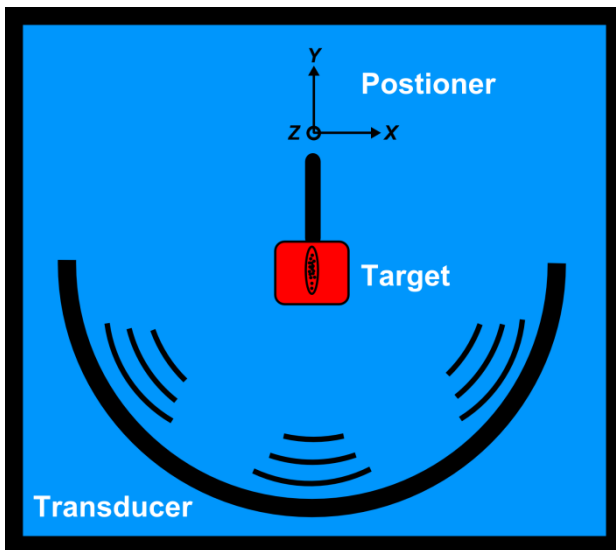


**Figure 5.1: Experimental setup: Histotripsy bubble clouds are formed in vacuum packed liver using a hemispherical, 500 kHz, electronically steered ultrasound array.**

Fig (5.1).

### 5.2.2 Transducer and Ablation

A histotripsy lesion was made in the liver sample using a custom built, 30 cm diameter hemi-spherical array composed of 256 circular elements, each with a diameter of 2 cm and a center frequency of 500 kHz as described in chapter 4. Using a bullet hydrophone,

the transducer was found to have a focal depth of 15 cm and -6 dB axial and longitudinal beam widths of 1.5 and 3.5 mm respectively. The pressure of the acoustic pulses was controlled by varying the voltage supply to the driving amplifier system. Prior to treatment, the supply voltage was increased until the transducer was able to reliably stimulate bubble clouds in water. To overcome any acoustic attenuation and reflection caused by the water-plastic bag interface, ablation was performed after increasing the supply voltage 260% beyond this point, resulting in an estimated in situ peak negative pressure exceeding 30 MPa.

Ablation was made by electronically steering two-cycle acoustic pulses ( $\sim 5 \mu\text{s}$  long) through at 6 x 12 mm grid with individual points spaced 1 x 2 mm apart using a randomly generated trajectory and firing at a rate of 50 Hz. A total of 1500 acoustic pulses were deposited per grid point.

### 5.2.3 MR Measurement and Analysis

After ablation, the vacuum packed liver was placed in the bore of a 7T, small bore, MR scanner (Agilent, Walnut Creek, CA) and imaged using a 2D, slice-selective, multi-echo sequence where MR echoes were recorded a time  $\tau$  after spin echoes that were spaced apart by an inter echo time  $2\tau$ . During acquisition the phase of the excitation pulses and the receiver were alternated 180 degrees along the transverse axis to suppress spurious induction decay signals excited by imperfect spin echo pulses.

The sample was maintained at room temperature during scanning. MR imaging parameters were: repetition time: 5 s; field of view: 6 x 6 cm; slice thickness: 4 mm; matrix size: 120 x 120 x 1; bandwidth: 100 kHz;  $\pi/2$  and  $\pi$  RF pulse widths: 1.0 and 0.8 ms respectively; and butterfly gradient amplitude and duration: 15 G cm<sup>-1</sup> and 1.0 ms respectively. This sequence was repeated while the inter-echo time,  $2\tau$ , was incremented through 5, 6, 8, 10, 12, 15, 20, 24, 30, and 40 ms four times. For each experiment, the number of MR echoes acquired was varied such that the final echo recorded occurred at 120 ms.

In the resulting images, the histotripsy lesion appeared as a bright rectangle with sharp borders surrounded by nominal appearing tissue. The  $1/T_2$  relaxation rate of both untreated liver and the treated homogenate were calculated by first selecting regions of interest in nominal appearing liver and the bright rectangular lesion. The pixels within these regions were averaged and then fit to the equation

$$M_i = M_o + M_x e^{-TE_i/T2} \quad \text{q: 5.1}$$

Using a constrained, least-squares, active-set algorithm in MATLAB (MathWorks, Natick, MA). Here,  $TE_i$  is the time at which the  $i^{th}$  echo occurs,  $M_i$  is the average magnitude of signal within the ROI at time  $TE_i$ , and  $M_x$  and  $M_o$  are terms that account for RF field inhomogeneities and, along with  $1/T2$ , are solved by the minimization algorithm.

Equation 5.1 can be quite unstable [45], especially when the sampled echoes are late compared to the decay time. In this case, the slope of the sampled signal approaches unity and the terms  $M_x$  and  $1/T2$  can both be under estimated. In our study, the  $1/T2$  rates resulting from scans using large values for  $2\tau$ , such as 30 or 40 ms, are subject to this type of fitting error. An example of this is shown in Fig (5.2.A), where the signal decay curve from one of the scans where  $2\tau$  is set to 5 ms is plotted as x's. The solid line is an unconstrained least-squares fit to this entire data set. The dotted line is an unconstrained least squares fit to only the data points at 45, 70, 95, and 120 ms. The unconstrained fit underestimates the initial magnitude of the signal as well as the decay rate.

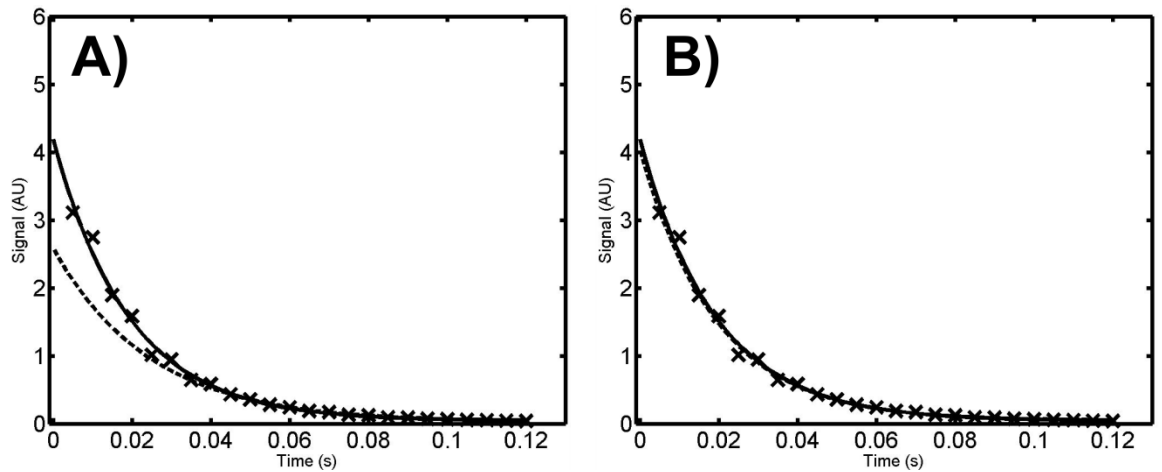


**Figure 5.2: Example T2 signal decay curves from a scan taken with an echo spacing of 5 ms. In (A) unconstrained fits to Eq 5.1 are made the full data set (solid line) and to a subsample of points at 45, 70, 95, and 120 ms (dashed line). The subsampled fit demonstrates the instability of Eq 1 and underestimates the maximum signal amplitude and the T2 time. In (B) the subsampled fit is constrained to have the same initial amplitude as the unconstrained fit using the full data set. This fit converges to the same values and the fully sampled set and corrects for the sub sampling error. Constrained fits were used to correct this error for all echo times used in this study.**

Fortunately, in this study, each signal-decay curve was acquired from the same slice in the same sample, using identical RF excitation pulses. It is thus safe to assume that the initial magnitude of the signal,  $M_x$ , is identical regardless of the inter-echo times or the

subset of the data chosen. As a result, while fitting each decay curve to Eq 5.1,  $M_x$  was constrained to be within 1% of the values obtained from an unconstrained fit when  $2\tau$  was equal to 5 ms. In Figure (5.2.B), the data in Fig (5.2.A) are repeated along with fits to the full and subsampled set. In this case, however, the solid and dashed lines are computed using the constrained minimization algorithm. In this case, the constrained fit to the subsampled data converges to that of the full data set. All reported  $1/T_2$  rates reported in this study were calculated using this constrained minimization technique.

### 5.3 Results

Representative images are displayed in Fig (5.3) and are an excellent example of echo-spacing dependence. Both images were acquired 40 ms after the initial excitation RF pulse. However, the image in frame A was acquired with an echo-spacing,  $2\tau$ , of 5 ms, while the image in frame B was acquired with an echo-spacing of 20 ms. The images are displayed with identical grayscale windows. The liver signal in the 20 ms case is diminished relative to the 5 ms case even though the two images were acquired at identical echo times. The lesion, on the other hand maintains nearly identical signal levels between the two images.

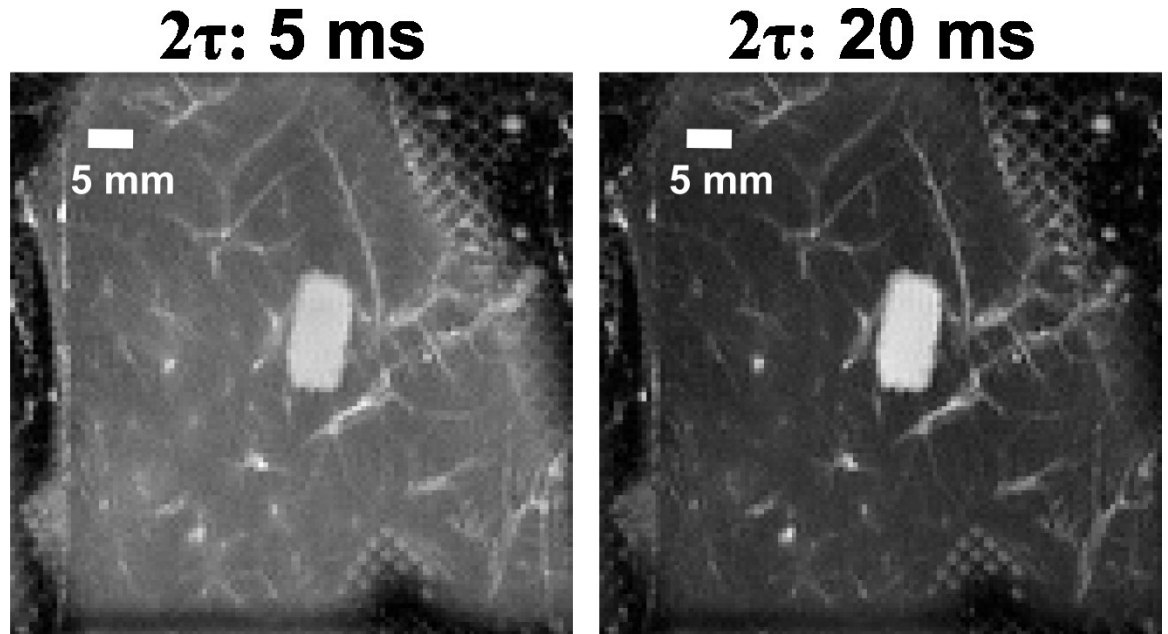


**Figure 5.3: T2 weighted images of the liver sample, each taken at an echo that occurs at 40 ms after the initial excitation pulse. The histotripsy lesion appears as a bright rectangle with sharp borders. The sequence that acquired the left hand image image was taken with an echo spacing,  $2\tau$ , of 5 ms, while the right hand image was taken with an echo spacing of 20 ms. Both images have identical grayscale windows. Though the two images are of identical samples and were taken at the**



same echo time, the right hand image exhibits a shorter T2 time, which results in a darker appearing liver.

The  $1/T_2$  rates estimated from the signal decay curve in each ROI are plotted in Figure (5.4) as a function of echo spacing. The figure shows that the estimated  $1/T_2$  rate of the control ROI increases with the echo-spacing used to make the measurement. However, the  $1/T_2$  rate of the lesion ROI remains invariant to echo spacing, suggesting a lack of the outer sphere mechanism. The dashed and dotted lines are both a least squares fit to two different outer-sphere models. Their implications are discussed below.

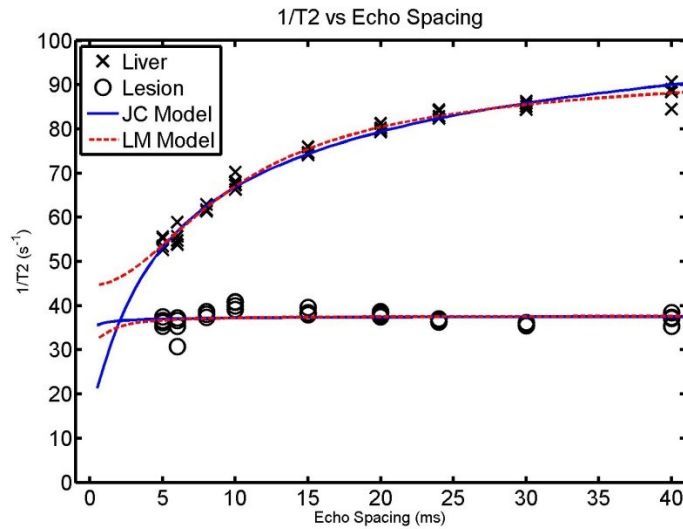


**Figure 5.4: The  $1/T_2$  rate estimated in both nominal liver and the histotripsy lesion as a function of the echo spacing used to acquired the measurement. The  $1/T_2$  rate in nominal liver displays a characteristic dependence on the echo spacing. The  $1/T_2$  rate in the ablated lesion is invariant to the echo spacing used to make the measurement. The solid and dashed lines are least squares fits of the date to the Jensen-Chandra model (solid line) and the Luz-Meiboom model (dashed line). See refs 27, 46, 47. These models suggest that the independence of the  $1/T_2$  rate of the histotripsy lesion stems from the erosion of the paramagnetic nodules that drive the outer sphere mechanism.**

## 5.4 Discussion

### 5.4.1 Removal of the Outer Sphere Mechanism

The results in Figure (5.4) support our hypothesis that histotripsy lengthens the T2 time of ablated tissues by removing the outer sphere mechanism. The T2 time of the ablated region is both longer than that found in the control sample and invariant to changes in  $2\tau$ . If histotripsy were to change T2 by some other mechanism, say by increasing the portion of free water in the lesion or decreasing the correlation times of proteins, the dependence T2 on  $2\tau$  may decrease somewhat, but would remain present.

### 5.4.2 Theoretical Models

While studying T2 relaxation in blood solutions, several researchers found that the dependence of the observed relaxation time on inter echo times could be predicted by the Luz-Meiboom model for chemical exchange between to different magnetic environments [46], [47]. This model can be written as

$$\frac{1}{T2} = \frac{1}{T2_o} + KT \left[ 1 - \frac{T}{\tau} \tanh\left(\frac{\tau}{T}\right) \right] \quad \text{q: 5.2}$$

Where  $\frac{1}{T2_o}$  represents contributions to the relaxation rate of water by mechanisms other than chemical exchange,  $\gamma$  is the gyromagnetic ration of hydrogen,  $K$  is a term that varies with the magnetic properties of the two environments and their corresponding relative populations of protons, and  $T$  is the average time a proton stays in one environment. Though originally derived to address chemical exchange, Eq 5.2 was shown to be quite accurate in the two limits where  $2\tau$  is either much greater than or smaller than  $T$  [48]. However a first-principles derivation has not yet been produced.

Jensen and Chandra later derived a new model from first principles by assuming weak magnetic field perturbations, Gaussian field correlation functions, and unrestricted diffusion of protons through the paramagnetic nodules [27]:

$$\frac{1}{T2} = \frac{1}{T2_o} + G \frac{T}{2} F\left(\frac{2\tau}{T}\right) \quad \text{q: 5.3}$$

Where  $G$  is a term that describes the average magnetic field fluctuations caused by the paramagnetic material and

$$F(x) = \frac{1}{\sqrt{\pi}} \int_0^{\infty} \frac{e^{-y}}{\sqrt{y}} \left[ 1 - \frac{1}{xy} \tanh(xy) \right] dy \quad \text{q: 5.4}$$

This model was shown to be able predict the observed  $1/T2$  rate in blood, human brain, and rat liver as a function of echo spacing, [27], [49].

We have performed a least squares fit of both the Luz-Meiboom (LM) model and the Jensen-Chandra (JC) model to the results found in our study. The resulting fitting parameters are displayed in Table 5.1. The JC and the LM models were both able to predict the echo spacing dependence of  $1/T2$  in the control ROI. They are displayed in Fig. (5.4) as the solid and dashed lines respectively. Least-squares fits to the lesion ROI resulted in, essentially, straight lines.

ROI Type	Model	$1/T2_o$ ( $s^{-1}$ )	K or G ( $Hz^2$ )	T (ms)
Lesion	LM	32	K = 12000	0.4
	JC	33	G = 90000	0.1
Liver	LM	45	K = 17000	3
	JC	18	G = 90000	1.2

**Table 5.1: Estimated fit terms from the Luz-Meiboom (LM) and Jensen-Chandra (JC) models of outer-sphere driven relaxation. The models were fit to the  $1/T2$  rates estimated in both nominal liver and the histotripsy lesion. The term  $1/T2_o$  refers to the base relaxation of the tissue without the outer sphere mechanism. The terms K and G reflect the magnetic properties of the microscopic environment as well as the populations of water molecules in each environment. The term T refers to the average time a water molecule can diffuse along the radius of a paramagnetic protein aggregate.**

### 5.4.3 Histotripsy and the LM and JC Models

Histotripsy plays a role in these models through the term T. In both the LM and the JC models, the estimated  $1/T2$  rate of a tissue becomes invariant to the echo-spacing when the term T becomes very small. This can be shown in Table 1, where the fitted T in the homogenate is ten times smaller than that found in the control sample. A comparison to Eq 8 in Ref [48] and Eqs 50 and 51 in Ref [27] show that  $T = r^2/D$ , where  $r$  is the radius of the paramagnetic material causing the field gradients and  $D$  is the diffusion constant of water. The time T becomes small when either the diffusivity of the water increases or the radius of the perturbing material becomes small.

Histotripsy can potentially reduce T by increasing the diffusivity of tissue water. As shown in Chapter 4, the diffusion coefficient in porcine liver ablated by histotripsy increases by a factor just over 2, which would correspondingly half T. However, this increase, assuming that histotripsy causes a comparable change in the sampled discussed here, is insufficient to completely explain the transition from echo-spacing dependent relaxation in nominal liver to echo-spacing invariant relaxation in treated liver. Such a transition requires a much more dramatic change to T. The alternative explanation is that histotripsy ablation causes the radius of the perturbing materials to decrease. Since T is proportional to the square of the radii of these materials, even small erosions of  $r$  can have a large impact on the observed T2 time.

#### 5.4.4 Future Work

In the above discussion, we have assumed that histotripsy removes the outer sphere contribution to transverse relaxation by eroding and dispersing small nodules of concentrated paramagnetic proteins. However, the same effect could also be wrought by transforming paramagnetic iron into diamagnetic iron. Though this mechanism seems unlikely, the current results are insufficient to disprove the hypothesis. It would be sufficient, though, to repeat the above experiment at two additional magnetic fields. If the ferritin within the homogenized lesions maintains its structure and magnetic properties but is dispersed into an aqueous state, than the observed  $1/T_2$  rate should increase linearly with field strength. If the tissue iron becomes diamagnetic, than the  $1/T_2$  rate should be constant with magnetic field strength.

#### 5.5 Conclusion

Histotripsy ablation in porcine liver removes the mechanism that causes the observed  $1/T_2$  relaxation rate to depend on the echo times used to make the measurement. This dependence is thought to be caused by water diffusing near paramagnetic aggregations of ferritin and hemoglobin. The  $1/T_2$  rate of untreated liver displays a strong dependence on echo spacing and is well predicted by both the Luz-Meiboom and Jensen-Chandra models for relaxation in the presence of paramagnetic corpuscles. Meanwhile, the  $1/T_2$  rate of homogenized liver is invariant with respect to echo spacing. The best explanation for this invariance is that the perturbing paramagnetic aggregations have been diminished by ablation. Accordingly, image contrast in  $T_2$ -weighted scans of abdominal histotripsy lesions should vary with how well the tissue type in question aggregates paramagnetic iron.

#### 5.6 References

- [1] Y. Kim, C. G. Fifer, S. K. Gelehrter, G. E. Owens, D. R. Berman, E. Vlaisavljevich, S. P. Allen, M. F. Ladino-Torres, and Z. Xu, "Developmental impact and lesion maturation of histotripsy-mediated non-invasive tissue ablation in a fetal sheep model," *Ultrasound Med. Biol.*, vol. 39, no. 6, pp. 1047–1055, Jun. 2013.
- [2] G. E. Owens, R. M. Miller, S. T. Owens, S. D. Swanson, K. Ives, G. Ensing, D. Gordon, and Z. Xu, "Intermediate-term effects of intracardiac communications created noninvasively by therapeutic ultrasound (histotripsy) in a porcine model," *Pediatr. Cardiol.*, vol. 33, no. 1, pp. 83–89, 2012.
- [3] Y. Kim, E. Vlaisavljevich, G. E. Owens, S. P. Allen, C. A. Cain, and Z. Xu, "In vivo transcostal histotripsy therapy without aberration correction," *Phys. Med. Biol.*, vol. 59,

- no. 11, pp. 2553–2568, Jun. 2014.
- [4] E. Vlaisavljevich, Y. Kim, S. P. Allen, G. Owens, S. Pelletier, C. A. Cain, K. Ives, and Z. Xu, “Image-guided non-invasive ultrasound liver ablation using histotripsy: feasibility study in an in vivo porcine model,” *Ultrasound Med. Biol.*, vol. 39, no. 8, pp. 1398–1409, 2013.
- [5] Y. Kim, T.-Y. Wang, Z. Xu, and C. A. Cain, “Lesion Generation Through Ribs Using Histotripsy Therapy Without Abberation Correction,” *IEEE Trans. Ultrason. Ferroelectr. Freq. Control*, vol. 58, no. 1997, pp. 696–747, 2011.
- [6] T. L. Hall, J. B. Fowlkes, and C. A. Cain, “A real-time measure of cavitation induced tissue disruption by ultrasound imaging backscatter reduction,” *IEEE Trans. Ultrason. Ferroelectr. Freq. Control*, vol. 54, no. 3, pp. 569–575, Mar. 2007.
- [7] T.-Y. Y. Wang, Z. Xu, F. Winterroth, T. L. Hall, J. B. Fowlkes, E. D. Rothman, W. W. Roberts, and C. A. Cain, “Quantitative ultrasound backscatter for pulsed cavitation ultrasound therapy-histotripsy,” *IEEE Trans. Ultrason. Ferroelectr. Freq. Control*, vol. 56, no. 5, pp. 995–1005, May 2009.
- [8] X. Zhang, R. M. Miller, K.-W. Lin, A. M. Levin, G. E. Owens, H. S. Gurm, C. A. Cain, and Z. Xu, “Real-time feedback of histotripsy thrombolysis using bubble-induced color Doppler,” *Ultrasound Med. Biol.*, vol. 41, no. 5, pp. 1386–401, May 2015.
- [9] T. Y. Wang, T. L. Hall, Z. Xu, J. B. Fowlkes, and C. A. Cain, “Imaging feedback of histotripsy treatments using ultrasound shear wave elastography,” *IEEE Trans. Ultrason. Ferroelectr. Freq. Control*, vol. 59, no. 6, pp. 1167–1181, 2012.
- [10] S. P. Allen, T. L. Hall, C. A. Cain, and L. Hernandez-Garcia, “Controlling cavitation-based image contrast in focused ultrasound histotripsy surgery,” *Magn. Reson. Med.*, vol. 73, pp. 204–213, Jan. 2015.
- [11] S. P. Allen, L. Hernandez-Garcia, C. A. Cain, and T. L. Hall, “MR-based detection of individual histotripsy bubble clouds formed in tissues and phantoms,” *Magn. Reson. Med.*, Nov. 2015.
- [12] S. P. Allen, T. L. Hall, C. A. Cain, and L. Hernandez, “MR-based targeting of histotripsy therapy at 7T,” in *Proceedings of the 21st Annual Meeting of ISMRM*, 2013, p. 1831.
- [13] S. P. Allen, W. W. Roberts, T. L. Hall, C. A. Cain, and L. Hernandez, “Characterization of in vivo histotripsy lesions using high field MRI,” in *Proceedings of the 20th Annual Meeting of ISMRM*, 2012, p. 1582.
- [14] T. L. Hall, “Magnetic Resonance Imaging of Histotripsy Lesions in Porcine Liver,” *Trans. Med. Imaging*, 2007.
- [15] A. Partanen, N. Farr, W. Kreider, T. Khokhlova, A. Maxwell, Y.-N. Wang, M. Bailey, and V. Khokhlova, “Use of MRI to visualize mechanically fractionated lesions generated by boiling histotripsy in tissue,” in *Abstract Book of 14th International Symposium for Therapeutic Ultrasound*, 2014.
- [16] Y. Kim, E. Vlaisavljevich, G. Owens, S. Allen, C. Cain, and Z. Xu, “In-vivo transcostal histotripsy therapy without aberration correction,” in *IEEE International Ultrasonics Symposium, IUS*, 2013, pp. 1817–1820.
- [17] M. Hoogenboom, D. Eikelenboom, M. H. den Brok, A. Veltien, M. Wassink, P.

- Wesseling, E. Dumont, J. J. Fütterer, G. J. Adema, and A. Heerschap, “In vivo MR guided boiling histotripsy in a mouse tumor model evaluated by MRI and histopathology,” *NMR Biomed.*, no. February, Apr. 2016.
- [18] E. M. Haacke, N. Y. C. Cheng, M. J. House, Q. Liu, J. Neelavalli, R. J. Ogg, A. Khan, M. Ayaz, W. Kirsch, and A. Obenaus, “Imaging iron stores in the brain using magnetic resonance imaging,” *Magn. Reson. Imaging*, vol. 23, no. 1, pp. 1–25, Jan. 2005.
- [19] A. Hocq, M. Luhmer, S. Saussez, S. Louryan, P. Gillis, and Y. Gossuin, “Effect of magnetic field and iron content on NMR proton relaxation of liver, spleen and brain tissues,” *Contrast Media Mol. Imaging*, no. January, 2014.
- [20] M. A. Roubidoux, “MR imaging of hemorrhage and iron deposition in the kidney,” *RadioGraphics*, vol. 14, no. 5, pp. 1033–44, Sep. 1994.
- [21] W. G. Bradley, “MR appearance of hemorrhage in the brain,” *Radiology*, vol. 189, no. 1, pp. 15–26, 1993.
- [22] R. A. Brooks and G. Di Chirio, “Magnetic resonance imaging of stationary blood: A review,” *Med. Phys.*, vol. 14, no. 6, p. 903, 1987.
- [23] J. M. Gomori and R. I. Grossman, “Mechanisms responsible for the MR appearance and evolution of intracranial hemorrhage,” *Radiographics*, vol. 8, no. 3, pp. 427–440, 1988.
- [24] Y. Ayant, E. Belorizky, J. Aluzon, and J. Gallice, “Calcul des densités spectrales résultant d’un mouvement aléatoire de translation en relaxation par interaction dipolaire magnétique dans les liquides,” *J. Phys.*, vol. 36, no. 10, pp. 991–1004, 1975.
- [25] P. Gillis and S. H. Koenig, “Transverse relaxation of solvent protons induced by magnetized spheres: application to ferritin, erythrocytes, and magnetite,” *Magn. Reson. Med.*, vol. 5, no. 4, pp. 323–345, Oct. 1987.
- [26] P. Gillis, A. Roch, and R. A. Brooks, “Corrected Equations for Susceptibility-Induced T<sub>2</sub>-Shortening,” *J. Magn. Reson.*, vol. 137, no. 2, pp. 402–407, Apr. 1999.
- [27] J. H. Jensen and R. Chandra, “NMR relaxation in tissues with weak magnetic inhomogeneities,” *Magn. Reson. Med.*, vol. 44, no. 1, pp. 144–56, Jul. 2000.
- [28] F. Q. Ye and P. S. Allen, “Relaxation enhancement of the transverse magnetization of water protons in paramagnetic suspensions of red blood cells,” *Magn. Reson. Med.*, vol. 34, no. 5, pp. 713–20, 1995.
- [29] R. G. Bryant, K. Marill, C. Blackmore, and C. Francis, “Magnetic relaxation in blood and blood clots,” *Magn. Reson. Med.*, vol. 13, no. 1, pp. 133–44, Jan. 1990.
- [30] K. R. Thulborn, J. C. Waterton, P. M. Matthews, and G. K. Radda, “Oxygenation dependence of the transverse relaxation time of water protons in whole blood at high field,” *Biochim. Biophys. Acta*, vol. 714, no. 2, pp. 265–70, Feb. 1982.
- [31] J. M. Gomori, R. I. Grossman, C. Yu-IP, and T. Asakura, “NMR Relaxation Times of Blood: Dependence on Field Strength, Oxidation State, and Cell Integrity,” *J. Comput. Assist. Tomogr.*, vol. 11, no. 4, pp. 684–690, 1987.
- [32] R. A. Brooks, J. Vymazal, J. W. Bulte, C. D. Baumgarner, and V. Tran, “Comparison of T<sub>2</sub> relaxation in blood, brain, and ferritin,” *J. Magn. Reson. Imaging*, vol. 5, no. 4, pp. 446–50, Jul. 1995.
- [33] H. Y. Carr and E. M. Purcell, “Effects of Diffusion on Free Precession in Nuclear

- Magnetic Resonance Experiments,” *Phys. Rev.*, vol. 94, no. 3, pp. 630–638, May 1954.
- [34] J. Bass, H. D. Sostman, O. Boyko, and J. a Koepke, “Effects of cell membrane disruption on the relaxation rates of blood and clot with various methemoglobin concentrations,” *Investigative radiology*, vol. 25, no. 11. pp. 1232–7, 1990.
- [35] P. a. Janick, D. B. Hackney, R. I. Grossman, and T. Asakura, “MR imaging of various oxidation states of intracellular and extracellular hemoglobin,” *Am. J. Neuroradiol.*, vol. 12, no. 5, pp. 891–897, 1991.
- [36] J. Vymazal, R. A. Brooks, O. Zak, C. McRill, C. Shen, and G. Di Chiro, “T1 and T2 of ferritin at different field strengths: Effect on MRI,” *Magn. Reson. Med.*, vol. 27, no. 2, pp. 368–374, 1992.
- [37] Y. Gossuin, A. Roch, R. N. Muller, P. Gillis, and F. Lo Bue, “Anomalous nuclear magnetic relaxation of aqueous solutions of ferritin: An unprecedented first-order mechanism,” *Magn. Reson. Med.*, vol. 48, no. 6, pp. 959–964, 2002.
- [38] Y. Gossuin, P. Gillis, R. N. Muller, and A. Hocq, “Relaxation by clustered ferritin: a model for ferritin-induced relaxation in vivo.,” *NMR Biomed.*, vol. 20, no. 8, pp. 749–56, Dec. 2007.
- [39] Y. Gossuin, R. N. Muller, P. Gillis, and L. Bartel, “Relaxivities of human liver and spleen ferritin,” *Magn. Reson. Imaging*, vol. 23, no. 10, pp. 1001–1004, 2005.
- [40] F. Q. Ye, W. R. Wayne Martin, and P. S. Allen, “Estimation of the iron concentration in excised gray matter by means of proton relaxation measurements.,” *Magn. Reson. Med.*, vol. 35, no. 3, pp. 285–9, 1996.
- [41] Y. Rozenman X. Zou, and H. L. Kantor, “. ‘Signal Loss Induced by Superparamagnetic Iron Oxide Particles in NMR Spin-Echo Images: The Role of Diffusion,’ *Magn. Reson. Med.* 14: 31,,” vol. 39, 1990.
- [42] K. M. Bennett, E. M. Shapiro, C. H. Sotak, and A. P. Koretsky, “Controlled Aggregation of Ferritin to Modulate MRI Relaxivity,” *Biophys. J.*, vol. 95, no. 1, pp. 342–351, 2008.
- [43] Z. Xu, Z. Fan, T. L. Hall, F. Winterroth, J. B. Fowlkes, and C. a. Cain, “Size measurement of tissue debris particles generated from pulsed ultrasound cavitation therapy-histotripsy.,” *Ultrasound Med. Biol.*, vol. 35, no. 2, pp. 245–55, Feb. 2009.
- [44] T. L. Hall, C. R. Hempel, K. Wojno, Z. Xu, C. A. Cain, and W. W. Roberts, “Histotripsy of the prostate: dose effects in a chronic canine model.,” *Urology*, vol. 74, no. 4, p. 932, Oct. 2009.
- [45] C. S. Poon and R. M. Henkelman, “Practical T2 quantitation for clinical applications,” *J. Magn. Reson. Imaging*, vol. 2, no. 5, pp. 541–553, Sep. 1992.
- [46] Z. Luz and S. Meiboom, “Nuclear Magnetic Resonance Study of the Protolysis of Trimethylammonium Ion in Aqueous Solution—Order of the Reaction with Respect to Solvent,” *J. Chem. Phys.*, vol. 39, no. 2, p. 366, Jun. 1963.
- [47] A. Allerhand and H. S. Gutowsky, “Spin—Echo NMR Studies of Chemical Exchange. I. Some General Aspects,” *J. Chem. Phys.*, vol. 41, no. 7, p. 2115, Jul. 1964.
- [48] R. a Brooks, F. Moiny, and P. Gillis, “On T 2 -Shortening by Weakly Magnetized Particles : The Chemical Exchange Model,” vol. 1020, pp. 1014–1020, 2001.
- [49] J. H. Jensen, R. Chandra, and H. Yu, “Quantitative model for the interecho time

dependence of the CPMG relaxation rate in iron-rich gray matter.," *Magn. Reson. Med.*, vol. 46, no. 1, pp. 159–65, Jul. 2001.



# Chapter 6:

## Summary and Future Work

### 6.1 Summary

This work provides general magnetic resonance imaging tools for visualizing and assessing histotripsy therapy. It strives to answer two questions:

1. Where is the histotripsy bubble cloud forming?
2. What effect did the histotripsy bubble cloud have on the target?

Question 1 is addressed in chapters 2 and 3, while question 2 is addressed in chapters 3 through 5.

In chapter 2 we have shown that magnetic resonance imaging can visualize histotripsy bubble clouds. This occurs when the water flow generated by a cavitation event is synchronized with a bipolar motion encoding gradient produced by the MR scanner. Due to the piecewise nature of MR image acquisition, the resulting image displays a localized and confined loss of image magnitude that represents the average water flow generated by many cavitation events. This visualization can be controlled by modifying the relative timing of the cavitation event to the sensitizing gradients. It can also be controlled by the magnitude of these gradients.

Chapter 3 shows that histotripsy sensitized MR sequences can be adapted to detect individual instances of a bubble cloud by employing single shot imaging techniques. We found that the magnitude of signal loss generated by a bubble cloud depends both on the magnitude of the sensitizing gradient and the treatment history. At the start of treatment, while the target tissue is intact, large magnitude gradients can visualize a bubble cloud and small magnitudes cannot. As treatment continues, the bubble cloud breaks apart the tissue structure and the water flow becomes sufficient to be detected by sequences with low

sensitivity. These sequences can be used to observe the bubble cloud behavior throughout treatment.

In addition to cavitation visualization, this dissertation has also identified several MR image contrast mechanisms that are sensitive to the liquefaction of tissue by histotripsy. In chapter 3, for example, we have demonstrated that cavitation imaging sequences at low sensitivity generate image contrast that responds to the number of acoustic pulses that have been deposited in the tissue. In chapter 4 we examined the response of the T1 and T2 relaxation constants and the apparent diffusion coefficient (ADC) to ablation by histotripsy in ex vivo tissues and phantoms. T1 was found to be invariant to the ablation of tissues and to weakly respond to the ablation of blood based phantoms. The ADC responded to ablation in all tissues and phantoms. The response of T2 varied by tissue and phantom type and correlated with the concentration of iron found in each tissue. The relative change in T2 and the ADC with respect to treatment were correlated to features found histologic slides of livers treated with the same therapy parameters. The examination revealed that two measures of cell structure correlated with T2 and the ADC: image variance and the number of intact iron nodules. These results indicate that T2 and the ADC can respond to the dose of histotripsy ablation.

The work in chapter 5 examines the mechanism behind the tissue-selective T2 response to histotripsy found in chapter 4. We show that the observed T2 in nominal liver depends on the echo times used to make the observation. This behavior is a characteristic sign of outer-sphere relaxation, where aggregations of paramagnetic proteins shorten T2 by generating microscopic magnetic field gradients. We then show that ablation by histotripsy removes this echo-time dependence. We attribute this change to the erosion of the features that drive outer-sphere relaxation: the paramagnetic aggregates such as hemosiderin and red blood cells.

The MR contrast parameters addressed in this work—bubble-cloud-sensitized imaging, T2, and the ADC—are all sensitive to different physical processes. Cavitation imaging is sensitive to the bulk mechanical properties of the tissue; T2 is sensitive to the state of aggregated iron proteins; and the ADC is widely believed to be sensitive to the integrity of cellular and intracellular membranes. Each contrast parameter can be used to

assess a different attribute of a histotripsy lesion, providing a comprehensive understanding of the effect of a given therapy.

The mechanisms provided in the work are designed to be adaptable to specific applications. For example, all experiments reported here were performed in ex vivo or in vitro situations. It is highly likely that adaptations such as shortening the image acquisition time or acquiring 3D volumes will be required before these techniques can be efficiently deployed in a clinical application. Further, there are still a few unresolved questions about these basic mechanisms. In this light, we will suggest future work that will extend our understanding of MR-guided histotripsy. Then we will suggest some specific adaptations that will be necessary for clinical applications.

## 6.2 Future Work

### 6.2.1 Cavitation Imaging

We have yet to precisely determine the accuracy of the cavitation imaging method. It is currently unknown how well the region of MR signal loss produced by a bubble cloud indicates the volume of tissue that will be destroyed at the end of therapy. Further, we have yet to establish if this accuracy varies with the sensitivity of the imaging sequence.

To answer this question, we have developed a mathematical model that describes the water displacement caused by the histotripsy bubble cloud as a random process with a well-defined probability distribution whose width is both a function of location relative to the center of the bubble cloud and the details of the sensitizing gradient waveform. If accurate it can also be used to predict the extent of damage to be caused by a bubble cloud.

#### Mathematical Model

Our model is as follows: MRI sequences can be sensitized to histotripsy by synchronizing the acoustic pulses such that the water flow caused by cavitation is bracketed by a balanced, bipolar, motion-encoding gradient. The first lobe of this gradient applies a linear phase across the mixing volume. This phase,  $\theta_r$  for some location within a voxel,  $\vec{r}$ , can be written as

$$\theta_r = 2\pi\vec{S}_g \cdot \vec{r} \tag{q: 6.1}$$

Where  $\vec{S}_g$  is

$$\vec{S}_g = \frac{\gamma}{2\pi} \int \vec{G}(t) dt \quad \text{q: 6.2}$$

has units of  $\text{cm}^{-1}$ , and is the slope of the linear phase introduced by the gradients. Here,  $\gamma$  is the gyromagnetic ratio and  $\vec{G}(t)$  is the waveform of the first gradient lobe.

After this first gradient, the bubble cloud rapidly and incoherently rearranges the water in the cavitation site. The water originally located at  $\vec{r}$  is replaced by water from somewhere else. Then, the second gradient lobe rewinds the phase originally added by the first lobe. The phase at  $\vec{r}$  can then be written as

$$\theta_r = 2\pi \vec{S}_g \cdot (\vec{R}(\vec{r}) - \vec{r}) \quad \text{q: 6.3}$$

Where  $\vec{R}(\vec{r})$  is a random variable whose probability density function (PDF) reflects the possible original locations from which this new bit of water has been transported. Essentially, the PDF of  $\vec{R}(\vec{r})$  contains information on both the extent of the bubble cloud and the likely region of signal loss.

To a first approximation, water at any location in the cavitation site is equally likely to be moved by the bubble cloud to location  $\vec{r}$ . Thus,  $\vec{R}(\vec{r})$  can be thought to have a uniform probability distribution with an interval equal to the width,  $w$ , of the volume over which the bubble cloud is capable of rearranging water molecules.

As a result,  $\theta_r$  also becomes a random variable of uniform distribution with an interval spanning  $-\frac{2\pi\|\vec{S}_g\|(w-2\|\vec{r}\|)}{2}$  to  $\frac{2\pi\|\vec{S}_g\|(w-2\|\vec{r}\|)}{2}$ .

The MR image will lose signal when the ensemble of phases composing the mixing volume sum together in a destructive manner. This is likely to occur if the phase gradient introduced by the sensitizing gradients is such that the bubble cloud can place water with all possible phases into the same voxel. Such conditions occur when the PDF of  $\theta_r$  spans  $2\pi$  radians. Thus, to maximize signal loss, the distance between phase wraps introduced by the gradients must be less than or equal to the size of the mixed volume of water.

$$\|\vec{S}_g\|w \geq 1 \quad \text{q: 6.4}$$

When this criteria is satisfied, every location within the cavitation site has an equal probability of having phase between  $-\pi$  and  $\pi$ . Further, since the number of locations

within the mixing volume is very large, almost every possible ensemble arrangement thoroughly samples the distribution interval and has a summation close to zero.

If the distance between phase wraps is much larger than the volume of mixed water, the bubble cloud will rearrange water with very similar phase. In this case,  $\|\vec{S}_g\|$  is small and the resulting distribution of phase within the volume will span a small interval, resulting in minimal signal attenuation. However, if  $\|\vec{S}_g\|$  is comparable to the size of the volume mixed by the bubble cloud, signal loss will occur.

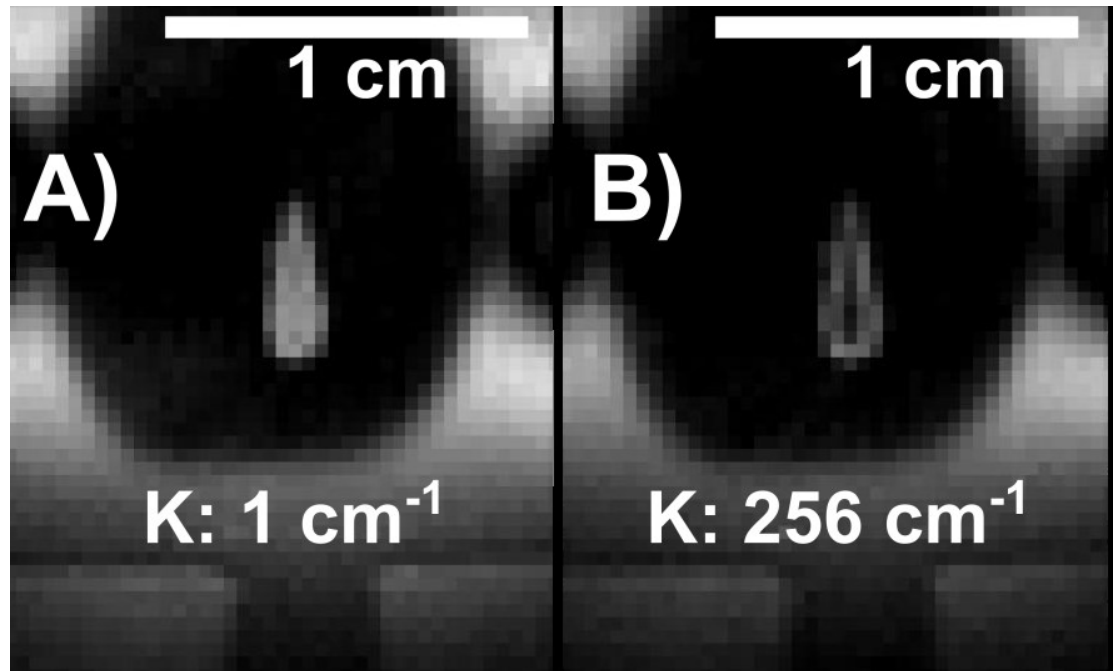


**Figure 6.1: Cavitation sensitized images of a red blood cell phantom that has been treated by depositing thousands of histotripsy pulses to a single location. Lysed red blood cells appear as a bright teardrop shape while surrounding the intact red blood cells are dark. Cavitation sensitized images with a sensitivity of (A) 1 and (B) 256 cm<sup>-1</sup> display varying distributions of motion induced signal loss. The image loss in neither (A) or (B) fully matches the teardrop shape. Future work can investigate the accuracy of MR cavitation imaging at predicting the extent of an ablated volume.**

### Need for Validation

The importance of this model can be shown in Fig. (6.1). Here, we have displayed a red blood cell phantom that has been treated with thousands of histotripsy pulses while simultaneously undergoing MR cavitation imaging. The region of red blood cells that have been lysed appears as a bright tear-drop shape compared to the surrounding intact red blood cells. The region where histotripsy has generated incoherent water flow appears dark within this teardrop shape. It can be seen that, as the sensitizing gradient is increased from 1

to  $256 \text{ cm}^{-1}$ , the region of signal loss generated by the bubble cloud expands but does not completely encompass the bright teardrop shape. This suggests that, in agar gel, the bubble cloud is capable of ablating red blood cells even when it cannot produce enough fluid flow to displace water more than  $250 \mu\text{m}$ . In this case, cavitation imaging cannot directly predict the entire region of ablated cells. However, if the PDF of the variable  $\vec{R}(\vec{r})$  were well understood, we may be able to calculate the entire region of ablation by observing the where the bubble cloud appears in a given cavitation sensitized image.

### **Correlation with Actual Tissue Damage.**

In chapter 3 we show that the signal loss induced by cavitation flow varies as a function of the number of histotripsy pulses that have been applied to the target. We would like to correlate this signal loss with other indicators of tissue ablation. One useful indicator is the elastic modulus of the target. Using MRI elastography [1], [2], it may be possible to measure the elastic modulus of the target tissue as it is ablated. This would allow us to correlate the flow induced signal loss with a measure of the actual state of the lesion.

## **6.2.2 Lesion Feedback Mechanisms**

### **Elastography Weighted Imaging**

MRI elastography may also be an excellent means to answer question 2 presented at the beginning of this chapter. It has been shown that the phase of an MR image can be sensitized to the propagation of shear waves through a medium [1]. It has also been shown that the modulus of histotripsy lesions decreases significantly during ablation, which then reduces the propagation of shear waves through the medium [3], [4]. As shown in reference [3], these changes can be up to 30% of the nominal modulus. This range is well within the clinical sensitivity of MR elastography [5] and may be a promising line of research. In Fig. (6.2) we show an elastography type image from a gel phantom with an inclusion representing a histotripsy lesion, demonstrating that our current system is capable of performing such analysis.

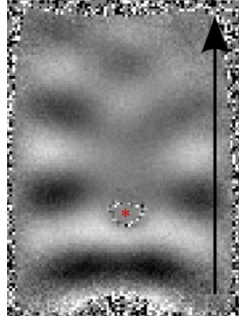


**Figure 6.2: An MR shearwave image of a gel phantom. Shearwaves propagate through the rectangular gel phantom in the direction indicated by the black arrow. A small inclusion was placed in the gel to simulate a histotripsy lesion (asterisk). The inclusion can be identified as the location where the shear waves are disrupted. MR shearwave imaging is part of MR elastography and may be a useful way to identify and measure histotripsy lesions.**

## **T2 Weighted Imaging**

The evidence presented in this dissertation make a strong case for the erosion of paramagnetic protein aggregates as the mechanism that drives T2 contrast in histotripsy lesions. However, as mentioned at the end of chapter 5, we cannot yet eliminate the possibility that histotripsy merely changes the magnetic properties of these molecules without eroding them. Though this hypothesis is unlikely, it can easily be disproven by performing the same experiment at two additional magnetic field strengths. If the  $1/T_2$  rate of the homogenate appears to be linear with field strength, then we will be able to declare that the ferritin within the homogenate has both maintained its magnetic properties and has been dispersed into an aqueous state.

## **6.3 Adaptation for Clinical Applications**

### **6.3.1 In Vivo Contrast**

Perhaps the most urgent work necessary for preparing clinical-ready MR-guided histotripsy is to characterize the response of T2 and ADC weighted image contrast during in vivo ablation. The work presented in chapters 4 and 5 are all in ex vivo tissues. Since the tissues are not vascularized, the image contrast was not contaminated by bleeding or edema. An influx of blood into the histotripsy lesions should present some complications to T2 weighted image contrast. If the blood is deoxygenated, it will reduce the T2 time of the lesion volume through the outer-sphere mechanism [6], [7]. If it remains oxygenated or becomes lysed by some mechanism, it will not reduce the T2 time of the lesion.

We have performed some preliminary experiments ablating tissues in vivo. However, due to the small size of our MR scanner and the difficulty of imaging living animals, these lesions were subsequently examined by MRI ex vivo. The several hour gap between treatment and imaging ensured that any blood within the lesion was deoxygenated.

The resulting images often show regions of dramatic T2 signal loss scattered within the lesion. When and where these regions appear remains inconsistent across the experiments reported in [8]–[10]. Meanwhile a recent paper has reported minimal T2 signal loss in boiling histotripsy lesions that were both treated and imaged in vivo [11], [12]. How blood will infiltrate and influence the appearance of histotripsy lesions in vivo remains an open question.

It is possible that the impact of blood on the T2 contrast can be modulated by the particular mode of therapy taken. Fig (6.3) presents a T2-weighted image of a block M shaped lesion that was formed in a pig brain. While most of the M displays signal loss indicative of hemorrhage and clotting, one leg appears abnormally bright. It turns out that this leg, and only this leg, was retreated several minutes after the initial M shape was ablated. It seems likely that the retreatment lysed the red blood cells that had infiltrated that portion of the lesion, which, by removing the outer-sphere effect, lengthened its T2 time. It also appears that more red blood cells did not re-infiltrate the lesion.

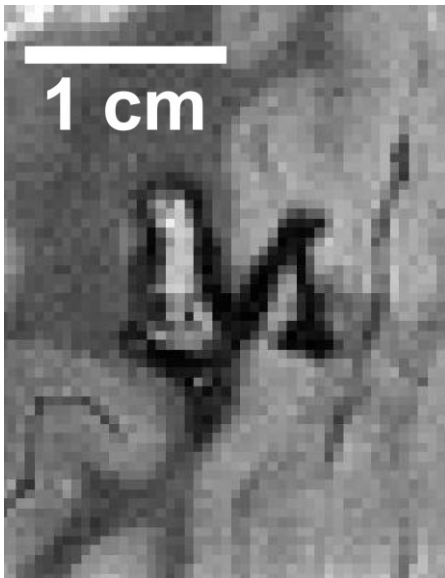


**Figure 6.3: A block M shaped lesion formed an in vivo porcine brain model. Much of the M shaped lesion has been infiltrated by deoxygenated blood, which appears dark in the MR image. However, one leg of the M was retreated several minutes after the original ablation. This leg appears quite bright, likely because the second pass lysed the red blood cells in this region. Future work can investigate the relationships between bleeding, treatment history and the appearance of lesions made in vivo.**

It seems possible that, once an initial wave of blood cells infiltrate a lesion, either the capillaries clot off or the hydrostatic pressure within the lesion prevents the supply of more blood cells. In this case, a retreatment by histotripsy would quickly lyse these red cells, improving the T2-weighted contrast of the lesion.



Lastly, MRI is also an excellent candidate for long term evaluation of chronic lesions. We expect to use MRI to monitor the evolution of the histotripsy lesion as the body recovers from ablation.

### **6.3.2 Non-Destructive Targeting**

Though the MR-cavitation imaging methods discussed in chapters 2 and 3 are capable of observing the first few bubble clouds formed in a tissue target, they cannot predict the location of therapy without causing some initial damage to the tissue. It is possible that in very sensitive structures, such as the brain, even a single mis-applied acoustic pulse cannot be tolerated. Instead, it may be feasible to use MR-acoustic radiation force imaging (MR-ARFI) to predict the location of the bubble cloud. MR-ARFI encodes any mechanical displacement of tissue caused by the acoustic radiation force into the phase of the resulting image [13], [14]. It has shown promise as a focus-finding technique in transcranial thermal ablation [15].

Prior to histotripsy ablation, one can use low-amplitude, high duty cycle acoustic pulses to generate a small acoustic radiation force displacement at the transducer focus. This displacement can then be detected with MRI. The location of peak ARFI displacement will correspond to the location of peak acoustic deposition and peak negative pressure. Thus the location of peak displacement on an MR-ARFI image should correspond to the histotripsy cavitation site. Once this site is determined to be placed correctly, the transducer can then transmit high-amplitude pulses to ablate the target.

## **6.4 Conclusions**

Magnetic resonance imaging is a powerful tool for visualizing the histotripsy bubble cloud and assessing the ablative state of a treated tissue. This dissertation presents general feedback tools that can be adapted to specific clinical needs.

## **6.5 References**

- [1] R. Muthupillai, P. J. Rossman, D. J. Lomas, J. F. Greenleaf, S. J. Riederer, and R. L. Ehman, "Magnetic resonance imaging of transverse acoustic strain waves.," *Magn. Reson. Med.*, vol. 36, no. 2, pp. 266–274, Aug. 1996.
- [2] T. Wu, J. P. Felmlee, J. F. Greenleaf, S. J. Riederer, and R. L. Ehman, "MR imaging of shear waves generated by focused ultrasound," *Magn. Reson. Med.*, vol. 43, no. 1, pp. 111–115, 2000.

- [3] T. Y. Wang, T. L. Hall, Z. Xu, J. B. Fowlkes, and C. A. Cain, "Imaging feedback of histotripsy treatments using ultrasound shear wave elastography," *IEEE Trans. Ultrason. Ferroelectr. Freq. Control*, vol. 59, no. 6, pp. 1167–1181, 2012.
- [4] T. Y. Wang, T. Hall, Z. Xu, J. Fowlkes, and C. Cain, "Imaging feedback for histotripsy by characterizing dynamics of acoustic radiation force impulse (ARFI)-induced shear waves excited in a treated volume," *IEEE Trans. Ultrason. Ferroelectr. Freq. Control*, vol. 61, no. 7, pp. 1137–1151, 2014.
- [5] S. K. Venkatesh, M. Yin, and R. L. Ehman, "Magnetic resonance elastography of liver: technique, analysis, and clinical applications.," *J. Magn. Reson. Imaging*, vol. 37, no. 3, pp. 544–55, 2013.
- [6] W. G. Bradley, "MR appearance of hemorrhage in the brain," *Radiology*, vol. 189, no. 1, pp. 15–26, 1993.
- [7] J. M. Gomori and R. I. Grossman, "Mechanisms responsible for the MR appearance and evolution of intracranial hemorrhage," *Radiographics*, vol. 8, no. 3, pp. 427–440, 1988.
- [8] Y. Kim, C. G. Fifer, S. K. Gelehrter, G. E. Owens, D. R. Berman, E. Vlaisavljevich, S. P. Allen, M. F. Ladino-Torres, and Z. Xu, "Developmental impact and lesion maturation of histotripsy-mediated non-invasive tissue ablation in a fetal sheep model," *Ultrasound Med. Biol.*, vol. 39, no. 6, pp. 1047–1055, Jun. 2013.
- [9] E. Vlaisavljevich, Y. Kim, S. P. Allen, G. Owens, S. Pelletier, C. A. Cain, K. Ives, and Z. Xu, "Image-guided non-invasive ultrasound liver ablation using histotripsy: feasibility study in an in vivo porcine model," *Ultrasound Med. Biol.*, vol. 39, no. 8, pp. 1398–1409, 2013.
- [10] Y. Kim, E. Vlaisavljevich, G. E. Owens, S. P. Allen, C. A. Cain, and Z. Xu, "In vivo transcostal histotripsy therapy without aberration correction," *Phys. Med. Biol.*, vol. 59, no. 11, pp. 2553–2568, Jun. 2014.
- [11] M. Hoogenboom, D. Eikelenboom, M. H. den Brok, A. Veltien, M. Wassink, P. Wesseling, E. Dumont, J. J. Fütterer, G. J. Adema, and A. Heerschap, "In vivo MR guided boiling histotripsy in a mouse tumor model evaluated by MRI and histopathology.," *NMR Biomed.*, no. February, Apr. 2016.
- [12] R. Alkins, Y. Huang, D. Pajek, and K. Hynynen, "Cavitation-based third ventriculostomy using MRI-guided focused ultrasound," *J. Neurosurg.*, vol. 119, no. 6, pp. 1520–1529, Dec. 2013.
- [13] N. McDannold and S. E. Maier, "Magnetic resonance acoustic radiation force imaging," *Med. Phys.*, vol. 35, no. 8, pp. 3748–3758, 2008.
- [14] M. Radicke, A. Engelbertz, B. Habenstein, M. Lewerenz, O. Oehms, P. Trautner, B. Weber, S. Wrede, and K. Maier, "New image contrast method in magnetic resonance imaging via ultrasound," *Hyperfine Interact.*, vol. 181, no. 1–3, pp. 21–26, 2008.
- [15] E. A. Kaye and K. B. Pauly, "Adapting MRI acoustic radiation force imaging for in vivo human brain focused ultrasound applications.," *Magn. Reson. Med.*, vol. 69, no. 3, pp. 724–33, Mar. 2013.

# **Appendix 1:**

## **Programming Code for 7T Agilent Magnetic Resonance Scanner**

### **A1.1 Introduction**

Much of the work done chapters 2 and 3 of this dissertation was performed using modified pulse sequences for a 7 Tesla, small animal scanner (Agilent, Walnut Creek, CA). These sequences are designed and implemented by writing and compiling source code which is then stored in the scanner system. When implemented, these scripts dictate the timing, amplitudes, and many other facets of the operation of the entire imaging system. In most cases it was expedient to take a working sequence compiled by the vendor and modify it to suit our needs. In a few other cases, the code had to undergo major changes to accomplish our needs.

In the following sections, I will introduce the pulse sequences used to produce the data presented in this dissertation. I will explain where it was used and how to recreate it. Often I will not reproduce the entire sequence, which would be too long. Instead, I will include ellipses to indicate preceding or proceeding code that has not been modified and line numbers to show where I made the changes. In cases where I have made extensive changes, I will include the complete file.

### **A1.2 Pulse Sequence Code**

#### **A1.2.1 A 2D, Multi-Shot, Gradient Recalled Echo Sequence to Detect and Visualize Histotripsy Bubble Clouds**

This sequence was used to produce all of the work in Chapter 2 except for Fig. (2.8). It incorporates a bipolar-diffusion weighted gradient into a pre-made 2D, gradient recalled

echo sequence. It then synchronizes these gradients with a single instance of a histotripsy bubble cloud.

### Code:

To create this sequence, insert a trapezoidal gradient into a stock gradient recalled echo sequence (*mems.c*) by inserting the lines

```

...
55 /* Initialize Bubble sensitizing Gradients*/
56 GENERIC_GRADIENT_T    bubblePositive;    //Intialize the positive sensitizing
gradient
57 GENERIC_GRADIENT_T    bubbleNegative;    //Initialize the negative
sensitizing gradient
...
81 initGeneric(&bubblePositive);            //Postive bubble sensitizing
gradient
82 initGeneric(&bubbleNegative);           //Negative bubble sensitizing
gradient

84 /*  Modify the bubble sensitizing gradients maximize it's amplitude.
******/
85 bubblePositive.duration = 0.001;
86 bubblePositive.amp = 0;
87 bubbleNegative.duration = 0.001;
88 bubbleNegative.amp = 0;
89 bubbleNegative.polarity = TRUE; //Make sure gradient is negative
...

108 /* calculate bubble sensitizing gradients. */
109 calcGeneric(&bubblePositive);
110 calcGeneric(&bubbleNegative);
111
112 /* Figure out offsets for ultrasound trigger */
113 if (us_offset <=0){
114     tr_offset = us_offset*-1;
115     us_offset = 0;
116     noFire = 1;  } /* Gradient calculations
******/

...

287     if (!trtype) {
288         delay(tr_delay-tr_offset);           // Relaxation delay
289         if (noFire == 1) {
290             sp2on(); delay(5e-6); sp2off();
291             delay(tr_offset - 5e-6); }
292     }
...

322     /* Phase encode, refocus, and dephase gradient *****/
323     if (sepSliceRephase) {                   // separate slice refocus gradient
324         obl_shapedgradient (ssr_grad.name,ssr_grad.duration,0,0,-
ssr_grad.amp,WAIT);
325         delay(4e-6);                         // delay between slab refocus and pe
326         pe_shapedgradient(pe_grad.name,pe_grad.duration,-ror_grad.amp,0,0,
-pe_grad.increment,vpe_mult,WAIT);
327     } else {
328         pe_shapedgradient (pe_grad.name,pe_grad.duration,-ror_grad.amp,0,-
ssr_grad.amp,
329         -pe_grad.increment,vpe_mult,WAIT);
330

```

```

331     delay(4e-6);                // delay after refocus/pe
332 }
333     delay(te_delay);            // delay after us triggers
334
335     /* Fire bubble cloud */
336     if(noFire ==0 ) {
337         sp2on(); delay(5e-6); sp2off();
338         delay(us_offset - 5e-6);}
339
340     /* Readout gradient and acquisition *****/
341     if (slprofile[0] == 'y')
342
obl_shapedgradient(ro_grad.name,ro_grad.duration,0,0,ro_grad.amp,NOWAIT);
343     else
344
obl_shapedgradient(ro_grad.name,ro_grad.duration,ro_grad.amp,0,0,NOWAIT);
345     delay(ro_grad.atDelayFront);
346     startacq(alfa);
347     acquire(np,1.0/sw);
348     delay(ro_grad.atDelayBack);
349     endacq();
...

```

### A1.2.2 Histotripsy Sensitized Echo-Planer Sequece.

This sequence was used to produce an echo-planar sequence that is sensitized to histotripsy. The code was modified such that histotripsy pulses could be selected to fire either 10 ms before the excitation RF pulse or between the RF excitation pulse and the slice-refocusing gradient. It was used to capture the images within Fig. (2.8).

#### Code:

To create this sequences, insert the following lines into a stock echo planar imaging sequence (*epip.c*):

```

1380     if (EPI) { /* EPI */
1381         if (GE && !DW && !VS) { /* EPI gradient echo, no diffusion, no
vascular suppression */
1382             /* if (image==1) {
1383                 sp2on(); delay(5e-6); sp2off(); // Fire trigger pulse (1)
1384                 delay(200e-6 - 5e-6);
1385                 sp2on(); delay(5e-6); sp2off(); // Fire trigger pulse (2)
1386                 delay(200e-6 - 5e-6);
1387                 sp2on(); delay(5e-6); sp2off(); // Fire trigger pulse (3)
1388                 delay(200e-6 - 5e-6);
1389                 sp2on(); delay(5e-6); sp2off(); // Fire trigger pulse (4)
1390                 delay(200e-6 - 5e-6);
1391                 sp2on(); delay(5e-6); sp2off(); // Fire trigger pulse (5)
1392                 delay(200e-6 - 5e-6);
1393                 sp2on(); delay(5e-6); sp2off(); // Fire trigger pulse (6)
1394                 delay(200e-6 - 5e-6);
1395                 sp2on(); delay(5e-6); sp2off(); // Fire trigger pulse (7)
1396                 delay(200e-6 - 5e-6);
1397                 sp2on(); delay(5e-6); sp2off(); // Fire trigger pulse (8)
1398                 delay(200e-6 - 5e-6);
1399                 sp2on(); delay(5e-6); sp2off(); // Fire trigger pulse (9)
1400                 delay(200e-6 - 5e-6);
1401                 sp2on(); delay(5e-6); sp2off(); // Fire trigger pulse (10)
1402                 delay(200e-6 - 5e-6);
1403                 // }
1404             // else {delay(1000e-6);}
1405             delay(10e-3);

```

```

1406
1407obl_shaped3gradient(epipR.name,epipP.name,epipS.name,epipTime,roramp*sign,epipP.amp,e
pipS.amp,NOWAIT);
1408         delay(ss_grad.rfDelayFront);
1409         if (ASL && RFOV)
1410shapedpulselist(shape90rfov,ss_grad.rfDuration,oph,rof1,rof1,'c',vms_ctr);
1411         else
shapedpulselist(shape90,ss_grad.rfDuration,oph,rof1,rof1,'c',vms_ctr);
1412         if (image==1) {
1413             sp2on(); delay(5e-6); sp2off(); // Fire trigger pulse (1)
1414             delay(200e-6 - 5e-6);
1415             sp2on(); delay(5e-6); sp2off(); // Fire trigger pulse (2)
1416             delay(200e-6 - 5e-6);
1417             sp2on(); delay(5e-6); sp2off(); // Fire trigger pulse (3)
1418             delay(200e-6 - 5e-6);
1419             sp2on(); delay(5e-6); sp2off(); // Fire trigger pulse (4)
1420             delay(200e-6 - 5e-6);
1421             sp2on(); delay(5e-6); sp2off(); // Fire trigger pulse (5)
1422             delay(200e-6-5e-6);
1423             sp2on(); delay(5e-6); sp2off(); // Fire trigger pulse (6)
1424             delay(200e-6 - 5e-6);
1425             sp2on(); delay(5e-6); sp2off(); // Fire trigger pulse (7)
1426             delay(200e-6 - 5e-6);
1427             sp2on(); delay(5e-6); sp2off(); // Fire trigger pulse (8)
1428             delay(200e-6 - 5e-6);
1429             sp2on(); delay(5e-6); sp2off(); // Fire trigger pulse (9)
1430             delay(200e-6 - 5e-6);
1431             sp2on(); delay(5e-6); sp2off(); // Fire trigger pulse (10)
1432             delay(200e-6 - 5e-6
1433             )
1434             else { delay(400e-6);}
1435             delay(delayToAcq-alfa - 1000e-6);
1436             // delay(delayToAcq-alfa);
...

```

### A1.2.3 HistoSems1DBeam2RefsPreRefocus

This sequence was used to produce the figures in Chapter 3. It creates a 1D, line scan, spin echo sequence and then inserts the customary bipolar cavitation sensitizing sequence. The ultrasound pulsing can then be synchronized to occur between the bipolar gradients.

#### Code:

This sequence was modified so heavily that it is reproduced in its entirety here.

```

/*
 * Varian, Inc. All Rights Reserved.
 * This software contains proprietary and confidential
 * information of Varian, Inc. and its contributors.
 * Use, disclosure and reproduction is prohibited without
 * prior consent.
 */

/*****
Spin echo imaging sequence modified to observe signal loss caused by histotripsy
cavitation
using paired diffusion weighting gradients.
*****/

#include <standard.h>
#include "sgl.c"

```

```

/* Phase cycling of 180 degree pulse */
static int ph180[2] = {1,3};

/* Declare cavitaion sensitizing gradients */
GENERIC_GRADIENT_T Diff;

pulsesequenece()
{
/* Internal variable declarations *****/
double freq90[MAXNSLICE],freq180[MAXNSLICE];
double te_delay1,te_delay2,tr_delay,taul,tau2,thk2fact,grosign;
int shape90,shape180,table=0;
double cycPerCm; // K-Space integral of diffusion gradient.
Units:cycles/cm
double diffGap = 1000e-6; // Gap between diffusion gradients.
double waitTime = 1e-4; // Wait after slice select pulse to fire
histotripsy.

/* Used for slice profile */
double sign=1;
char slprofile[MAXSTR];

/* Real-time variables used in this sequence *****/
int vpe_steps = v1;
int vpe_ctr = v2;
int vms_slices = v3;
int vms_ctr = v4;
int vpe_offset = v5;
int vpe_mult = v6;
int vph180 = v7; // Phase of 180 pulse
int vph2 = v8; // alternate phase of 180 on odd transients
int vssc = v9; // Compressed steady-states
int vtrimage = v10; // Counts down from nt, trimage delay when 0
int vacquire = v11; // Argument for setacqvar, to skip steady state
acquires
int vtrigblock = v12; // Number of slices per trigger block
int vWhichLoop = v13; // indicator of which case to use for motion encoding
gradients
int vCavLoop = v14; // Matching criteria for case where both Diff grad and
US fire
int vNoGradLoop = v15; // Matching criteria for case where only Us fires.
int vNoUsLoop = v16; // Matching critera for case where only Diff Grad is
excited.

/* Initialize paramaters *****/
init_mri();
cycPerCm = getval("cycPerCm");
getstrnwarn("slprofile",slprofile);
grosign = copysign(1.0,gro);

/* Check for external PE table *****/
if (strcmp(petable,"n") && strcmp(petable,"N") && strcmp(petable,"")) {
loadtable(petable);
table = 1;
}

/* RF Power & Bandwidth Calculations *****/
shape_rf(&p1_rf,"p1",p1pat,p1,flip1,rof1,rof2);
shape_rf(&p2_rf,"p2",p2pat,p2,flip2,rof1,rof2);
calc_rf(&p1_rf,"tpwr1","tpwr1f");
calc_rf(&p2_rf,"tpwr2","tpwr2f");

thk2fact=p2_rf.bandwidth/p1_rf.bandwidth;
putvalue("thk2fact",thk2fact);
double thk2 = 1.5;
double *thk2Ptr = &thk2; // Hard code in thickness of orthogonal pencil beam
excitaion slice.

/* Hard code in nv to equal 2 */
nv = 3;
putvalue("nv", nv); // make sure vnmrj knows how many fids to expect

```

```

/* Initialize gradient structures *****/
init_slice(&ss_grad,"ss",thk);
init_slice_butterfly(&ss2_grad,"ss2",thk2,gcrush,tcrush);
init_slice_refocus(&ssr_grad,"ssr");
if (FP_GT(tcrushro,0.0))
    init_readout_butterfly(&ro_grad,"ro",lro,np,sw,gcrushro,tcrushro);
else
    init_readout(&ro_grad,"ro",lro,np,sw);
init_readout_refocus(&ror_grad,"ror");
init_phase(&pe_grad,"pe",lpe,nv);
initGeneric(&Diff);

/* Gradient calculations *****/
calc_readout(&ro_grad, WRITE, "gro","sw","at");
ro_grad.m0ref *= grof;
calc_readout_refocus(&ror_grad, &ro_grad, NOWRITE, "gror");
calc_phase(&pe_grad, NOWRITE, "gpe","tpe");
calc_slice(&ss_grad,&p1_rf,WRITE,"gss");
calc_slice(&ss2_grad,&p2_rf,WRITE,"gss2");
if (slprofile[0] == 'y') {
    // Combined slice refocusing and read dephasing, reverse gradient
    // sign if ror > ssr integral
    sign = (ss_grad.m0ref > ro_grad.m0ref) ? 1.0 : -1.0;
    ss_grad.m0ref -= ro_grad.m0ref;
}
calc_slice_refocus(&ssr_grad, &ss_grad, NOWRITE,"gssr");

/* Equalize refocus and PE gradient durations *****/
calc_sim_gradient(&ror_grad, &pe_grad, &ssr_grad,0,WRITE);

/* Calculate motion encoding gradients */
Diff.calcFlag = AMPLITUDE FROM MOMENT DURATION;
Diff.duration = 2.5e-3;
Diff.m0 = cycPerCm/nuc_gamma();
calcGeneric(&Diff);
putvalue("diffAmp",Diff.amp);

/* Create optional prepulse events *****/
if (sat[0] == 'y') create_satbands();
if (fsat[0] == 'y') create_fatsat();
if (mt[0] == 'y') create_mtc();
if (ir[0] == 'y') create_inversion_recovery();

sql_error_check(sglerror);

/* Min TE *****/
tau1 = ss_grad.rfCenterBack + 4e-6 + ssr_grad.duration + waitTime +
2*Diff.duration + diffGap + 4e-6 + ss2_grad.rfCenterFront;
tau2 = ss2_grad.rfCenterBack + pe_grad.duration + 4e-6 + ro_grad.timeToEcho +
alfa;

temin = 2*(MAX(tau1,tau2) + 2*4e-6); /* have at least 4us between gradient
events */
if (minte[0] == 'y') {
    te_delay1 = temin/2 - tau1;
    te_delay2 = temin/2 - tau2;
    putvalue("te",temin);
}
else {
    te_delay1 = te/2 - tau1;
    te_delay2 = te/2 - tau2;
}
if (te < temin)
    abort_message("TE too short, minimum TE = %.2f msec",1000*temin + 0.005);

/* Check nsblock, the number of slices blocked together
(used for triggering and/or inversion recovery) */
check_nsblock();

```



```

/* Min TR *****/
trmin = ss_grad.rfCenterFront + te + ro_grad.timeFromEcho + 8e-6;

/* Increase TR if any options are selected *****/
if (sat[0] == 'y') trmin += satTime;
if (fsat[0] == 'y') trmin += fsatTime;
if (mt[0] == 'y') trmin += mtTime;
if (ticks > 0) trmin += 4e-6;

/* Adjust for all slices *****/
trmin *= ns;

/* Inversion recovery *****/
if (ir[0] == 'y') {
/* tiaddTime is the additional time beyond IR component to be included in ti
*/
/* satTime, fsatTime and mtTime all included as those modules will be after IR
*/
tiaddTime = satTime + fsatTime + mtTime + 4e-6 + ss_grad.rfCenterFront;
/* calc_irTime checks ti and returns the time of all IR components */
trmin += calc_irTime(tiaddTime,trmin,mintr[0],tr,&trtype);
}

if (mintr[0] == 'y') {
tr = trmin;
putvalue("tr",tr);
}
if (FP_LT(tr,trmin)) {
abort_message("TR too short. Minimum TR = %.2fms\n",trmin*1000+0.005);
}

/* Calculate tr delay */
tr delay = granularity((tr-trmin)/ns,GRADIENT RES);

double pss2 = 0.28;
double *pss2Ptr = &pss2; // Hard code in the pencil beam pulse

/* Generate phase-ramped pulses */
offsetlist(pss,ss_grad.ssamp,0,freq90,ns,seqcon[1]);
offsetlist(pss2Ptr,ss2_grad.ssamp,0,freq180,ns,seqcon[1]); // Hard code
in the location of the pencil beam
shape90 =
shapelist(p1_rf.pulseName,ss_grad.rfDuration,freq90,ns,ss_grad.rfFraction,seqcon[1]);
shape180 =
shapelist(p2_rf.pulseName,ss2_grad.rfDuration,freq180,ns,ss2_grad.rfFraction,seqcon[1]);

/* Set pe_steps for profile or full image *****/
pe_steps = prep_profile(profile[0],nv,&pe_grad,&null_grad);
F initval(pe_steps/2.0,vpe offset);

/* Slice profile *****/
if (slprofile[0] == 'y') ror_grad.amp = 0;

/* Shift DDR for pro *****/
roff = -poffset(pro,ro_grad.roamp);

/* Adjust experiment time for VnmrJ *****/
if (ssc<0) {
if (seqcon[2] == 'c') g_setExpTime(trmean*(ntmean*pe_steps*arraydim -
ssc*arraydim));
else g_setExpTime(trmean*(ntmean*pe_steps*arraydim - ssc*pe_steps*arraydim));
}
else g_setExpTime(trmean*ntmean*pe_steps*arraydim + tr*ssc);

/* Return parameters to VnmrJ */
putvalue("rgss",ss_grad.tramp); //90 slice ramp
if (ss2_grad.enableButterfly) { //180 slice ramps
putvalue("rcrush",ss2_grad.crusher1RampToCrusherDuration);
putvalue("rgss2",ss2_grad.crusher1RampToSsDuration);
}
}

```

```

else {
    putvalue("rgss2",ss2_grad.tramp);
}
if (ro_grad.enableButterfly) {
    putvalue("rgro",ro_grad.crusher1RampToSsDuration);
}
else {
    putvalue("rgro",ro_grad.tramp);    //RO ramp
}
putvalue("tror",ror_grad.duration); //ROR duration
putvalue("rgror",ror_grad.tramp);   //ROR ramp
putvalue("gpe",pe_grad.peamp);     //PE max amp
putvalue("gss",ss_grad.ssamp);
putvalue("gro",ro_grad.roamp);

/* Set phase cycle table */
settable(t2,2,ph180);

/* PULSE SEQUENCE *****/
status(A);
rotate();
triggerSelect(trigger); // Select trigger input 1/2/3
obsoffset(resto);
delay(4e-6);
initval(fabs(ssc),vssc); // Compressed steady-state counter
if (seqcon[2]=='s') assign(zero,vssc); // Zero for standard peloop
assign(one,vacquire); // real-time acquire flag
setacqvar(vacquire); // Turn on acquire when vacquire is zero

/* trigger */
if (ticks > 0) F_initval((double)nsblock,vtrigblock);

/* Begin phase-encode loop *****/
peloop(seqcon[2],pe_steps,vpe_steps,vpe_ctr);

    if (trtype) delay(ns*tr_delay); // relaxation delay

    /* Compressed steady-states: 1st array & transient, all arrays if ssc is
negative */
    if ((ix > 1) && (ssc > 0))
        assign(zero,vssc);
    sub(vpe_ctr,vssc,vpe_ctr); // vpe_ctr counts up from -ssc
    assign(zero,vssc);
    if (seqcon[2] == 's')
        assign(zero,vacquire); // Always acquire for non-compressed loop
    else {
        ifzero(vpe_ctr);
        assign(zero,vacquire); // Start acquiring when vpe_ctr reaches zero
        endif(vpe_ctr);
    }

    /* Read external kspace table if set *****/
    if (table)
        getelem(t1,vpe_ctr,vpe_mult);
    else {
        ifzero(vacquire);
        sub(vpe_ctr,vpe_offset,vpe_mult);
        elsenz(vacquire);
        sub(zero,vpe_offset,vpe_mult); // Hold PE mult at initial value for
steady states
        endif(vacquire);
    }

    getelem(t2,vpe_ctr,vph180);
    add(oph,vph180,vph180); // 180 deg pulse phase alternates +/-
90 from receiver
    mod2(ct,vph2);
    dbl(vph2,vph2);
    add(vph180,vph2,vph180); // Alternate phase for 180 on odd
transients

```

```

/* Begin multislice loop *****/
msloop(seqcon[1],ns,vms slices,vms ctr);

    if (!trtype) delay(tr delay);          // Relaxation delay

    if (ticks > 0) {
        modn(vms_ctr,vtrigblock,vtest);
        ifzero(vtest);                    // if the beginning of an trigger
block
            xgate(ticks);
            grad_advance(gpropdelay);
            delay(4e-6);
            elsenz(vtest);
            delay(4e-6);
            endif(vtest);
    }

    splon(); delay(4e-6); sploff();        // Scope trigger

/* Prepulse options *****/
if (ir[0] == 'y') inversion_recovery();
if (sat[0] == 'y') satbands();
if (fsat[0] == 'y') fatsat();
if (mt[0] == 'y') mtc();

/* Slice select RF pulse *****/
obspower(pl_rf.powerCoarse);
obspwrf(pl_rf.powerFine);
delay(4e-6);
obl_shapedgradient(ss_grad.name,ss_grad.duration,0,0,ss_grad.amp,NOWAIT);
delay(ss_grad.rfDelayFront);
shapedpulselist(shape90,ss_grad.rfDuration,oph,rof1,rof2,seqcon[1],vms_ctr);
delay(ss_grad.rfDelayBack);

/* Slice Rewind Gradient */
delay(4e-6);
obl_shapedgradient(ssr_grad.name, ssr_grad.duration, 0.0, 0.0, -
ssr_grad.amp, WAIT);

/* Sensitize to Histotripsy and fire single histotripsy pulse */
delay(waitTime);
/* Logic switching between csg = 0 and csg = cycPerCm case*/
assign(vpe_ctr, vWhichLoop);
sub(vWhichLoop,one, vCavLoop);
sub(vWhichLoop,two, vNoGradLoop);
sub(vWhichLoop,zero, vNoUsLoop);

/* Conditional for case where both Diff Grad and the US pulse are triggered
*/
ifzero(vCavLoop);

obl_shapedgradient(Diff.name, Diff.duration, 0.0, 0.0,Diff.amp,WAIT);
ifzero(vacquire);
sp2on(); delay(5e-6); sp2off();
elsenz(vacquire);
delay(5e-6);
endif(vacquire);
delay(diffGap-5e-6);
obl_shapedgradient(Diff.name, Diff.duration, 0.0,0.0,-Diff.amp,WAIT);

endif(vCavLoop);

/* Conditional for case where only US fires, no Diff grad */
ifzero(vNoGradLoop);

obl_shapedgradient(Diff.name, Diff.duration, 0.0, 0.0, 0.0, WAIT);
ifzero(vacquire);
/* sp2on()*/ delay(5e-6);/* sp2off()*/
elsenz(vacquire);
delay(5e-6);

```

```

        endif(vacquire);
        delay(diffGap-5e-6);
        obl_shapedgradient(Diff.name, Diff.duration, 0.0, 0.0, 0.0, WAIT);

        endif(vNoGradLoop);

        /* Conditional for case where only US fires, no Diff grad */
        ifzero(vNoUsLoop);

        obl_shapedgradient(Diff.name, Diff.duration, 0.0,0.0,Diff.amp,WAIT);
        ifzero(vacquire);
        delay(5e-6);
        elsenz(vacquire);
        delay(5e-6);
        endif(vacquire);
        delay(diffGap-5e-6);
        obl_shapedgradient(Diff.name, Diff.duration, 0.0,0.0,-Diff.amp,WAIT);

        endif(vNoUsLoop);

        delay(te_delay1);

        /* Refocusing RF pulse *****/
        obspower(p2_rf.powerCoarse);
        obspwrf(p2_rf.powerFine);
        delay(4e-6);
        obl_shapedgradient(ss2_grad.name,ss2_grad.duration,0.0,
ss2_grad.amp,0.0,NOWAIT);
        delay(ss2_grad.rfDelayFront);

        shapedpulselist(shapel180,ss2_grad.rfDuration,vph180,rof2,rof2,seqcon[1],vms_ctr);
        delay(ss2_grad.rfDelayBack);

        delay(te_delay2);

        /* Phase encode, refocus, and dephase gradient *****/
        pe_shapedgradient(pe_grad.name,pe_grad.duration,-
1*grosign*ror_grad.amp,0,0.0,
        -pe_grad.increment*0.0,vpe_mult,WAIT);

        /* Readout gradient and acquisition *****/
        if (slprofile[0] == 'y') {
            obl_shapedgradient(ro_grad.name,ro_grad.duration,0,0,ro_grad.amp,NOWAIT);
        } else

        obl_shapedgradient(ro_grad.name,ro_grad.duration,grosign*ro_grad.amp,0,0,NOWAIT);
        delay(ro_grad.atDelayFront);
        startacq(alfa);
        acquire(np,1.0/sw);
        delay(ro_grad.atDelayBack);
        endacq();

        endmsloop(seqcon[1],vms_ctr);

        endpeloop(seqcon[2],vpe_ctr);

        /* Inter-image delay *****/
        sub(ntrt,ct,vtrimage);
        decr(vtrimage);
        ifzero(vtrimage);
            delay(trimage);
        endif(vtrimage);
    }

```

## Appendix 2:

# Spiral Sequences on the Agilent 7T Scanner

### A2.1 Introduction

Though not presented in the main body of this dissertation, I did implement single shot spiral imaging and reconstruction on a 7 Tesla small animal scanner. The imaging sequence required gradient trajectory mapping to properly produce a reconstructed image. In this appendix, I include an installation manual for this sequence as well as the source code used to produce the spirals.

### A2.2 Installation Manual: 2D Spiral Imaging

Vnmrj 3.1 Installation & User Guide. February 2013

### A2.3 Table of Contents

[2D Spiral Imaging](#)

[Table of Contents](#)

[About This Installation](#)

[Overview](#)

[Miscellania](#)

[Feedback:](#)

[Further Help:](#)

[Installation](#)

[File Installation](#)

[File Modification](#)

[Compilation](#)

[Imaging](#)

[Acquiring a Spiral K-Space Trajectory Image](#)

[Acquiring a Spiral K-Space Trajectory Measurement](#)

[Reconstruction](#)

[Support](#)

[Psg files](#)

[calcSpiral](#)

[initSpiral](#)  
[Matlab Files](#)  
[getFid](#)  
[getIdealGrads](#)  
[getTraj](#)  
[matlabRegrid](#)  
[nufftRecon](#)  
[readfid](#)  
[reconExample](#)  
[reconstructGREImageArrayed](#)  
[reconstructGREImage](#)  
[rotclckwise](#)  
[rotTraj](#)  
[setPathRecon](#)  
[spiralTrajectoryMap](#)  
[tryreadprocpa](#)

## **A2.4 About This Installation**

The programs and functions described below implement 2-D single and multi-shot spiral imaging on a Vnmrj 3.1 imaging system (Agilent Inc.). The spiral design follows that discussed in (Glover G. H. 1999. Simple Analytic Spiral K-Space Algorithm. Magn. Reson. Med 42:412:415). Glover's algorithm is slightly modified by adding a ramp at the end to the spiral sequence to bring the gradient amplifier current to zero before completion of the sequence. Additionally, the spiral can be reversed into a spiral-in trajectory for uses such as fMRI.

This guide assumes some familiarity with MRI, spiral imaging, and the vnmrj user interface. The operator should be able acquire a spulse FID, a scout image, and an ordinary GRE image of a subject. See the further help section of this manual for more details.

This implementation also supports a trajectory mapping technique described in (Duyn JG, et al. May 1998. Simple Correction Method for K-Space Trajectory Deviations in MRI. J Magn Reson. 132(1):150:3.). These are useful for 7T imaging systems where B0 inhomogeneity is large.

Image reconstruction, as of February 2013, is not supported in Vnmrj 3.1 and must be done with some other software--typically using MATLAB. Fortunately, UMICH is home to some of the best and brightest minds in the image reconstruction field. Code initially provided by Jeff Fessler of UMICH and Brian Hargreaves of Stanford is included.

See (<http://web.eecs.umich.edu/~fessler/code/index.html>) and (<http://mrsrl.stanford.edu/~brian/gridding/>).

Descriptions of the files and functions used for both image acquisition and reconstruction are presented in the “Support” section.

#### A2.4.1 Overview

Varian Inc (now Agilent) has done a great job making it easy to program and implement new pulse sequences for their Vnmrj system. So long as one inserts the right files into the right folders, one can implement almost anything. This implementation of the 2D spirals is comprised of the following sets of files:

The main pulse sequence control is done in C#.

- *KxMap.c*, *KyMap.c*, and *spiral.c*: These are the main pulse sequence programming functions
- *histosgl.c*, *sglHistoCommon.c*, *sgl*, *spiralsgl.c*, and *spiralsgl.h*: Supporting libraries, header files, and definitions necessary to make the main pulse sequences programs work.

Some supporting functions (called macros) are written in Agilent’s custom MAGICAL language.

- *KxMap*, *KyMap*, and *spiral*: These macros make it easy to call and modify imaging parameters for the main pulse sequence programs without having to recompile the entire sequence
- *getGrads* and *npSet*: These support, respectively, copying the calculated gradient waveforms to the active study folder and resolving a bug with setting the Vnmrj parameter “np”.

Parameter Files and folders:

- *KxMap.par*, *KyMap.par*, and *spiral.par*: These store imaging parameters, making it easy to call up the main pulse sequences without having to re-derive many imaging parameters.

Xml interface folder:

- *spiral*: The contents of this folder make the vnmrj GUI easy to use for spiral imaging. In particular they circumvent the bug associated with setting the parameter “np” correctly.

Matlab files useful for reconstruction after acquisition is complete. These include toolboxes made by Jeffrey Fessler and Brian Hargreaves. Their files and uses are legion.

#### A2.4.2 Miscellania

There are a few important things to know about this particular installation.

1. The function that computes the spiral readout--*spiralsgl.c*--writes the computed files twice. The first file is written for the gradient driving hardware. The relative amplitudes of the wave form are written in “DAQ scaled units.” This file is written to */home/<user>/vnmrsys/shapelib/*. The second file is written for user access. This file is a **binary** file written to */home/<user>/Spiral* with the names *Gx.GRD* and *Gy.GRD*. This second file is in G/cm as opposed to the DAQ units of the first file.

2. *spiralsgl.c* also writes the angle parameter and the first time derivative of the angle parameter under the names *Th.GRD* and *dth.GRD*. These can be useful for checking the designed gradient slew rate.

3. Also, *spiralsgl.c* uses a default maximum slew rate of one half the system maximum.

4. All three main pulse sequences--*spiral.c*, *KyMap.c*, and *KxMap.c*--use a maximum gradient amplitude of one fifth the system maximum amplitude. But this can be modified by changing an input to the command *initSpiral*.

Additionally, any other spiral pulse sequence could be easily implemented by removing the *initspiral* and *calcspiral* functions and replacing them with a program that will calculate a different readout (such as 3D spirals in the future).

#### A2.4.3 Feedback:

This installation is a work in progress and I am always looking for improvements. If you have any problems or suggestions, please contact me at [stevepa@umich.edu](mailto:stevepa@umich.edu).



#### A2.4.4 Further Help:

Agilent has published additional resources for user programming. I find them to be very informative. Check the ctools site for the MR Engin Group under the resources tab or open

[file:///home/vnmrj\\_3.1\\_A/help/html/WebHelp/wwhelp/wwhimpl/js/html/wwhelp.htm#href=Vnmrj3Install/front\\_9100016600.html](file:///home/vnmrj_3.1_A/help/html/WebHelp/wwhelp/wwhimpl/js/html/wwhelp.htm#href=Vnmrj3Install/front_9100016600.html) in Firefox. The html version is searchable and is quickly becoming my weapon of choice.

### A2.5 Installation

Installation of the spiral program consists of three steps: 1. Copying files into your user's local vnmrj libraries. 2. Modifying one .c file and one macro. 3. Compiling the pulse sequence files into an executable command. Future versions of this spiral system will include a bash script to do this for you.

#### A2.5.1 File Installation

1. Login to the desired account on the computer that controls the 7T scanner.
2. copy the file “/home/histo/Spiral/2D\_Spiral.tar” into a directory of your choosing. It does not matter where, so long as you can extract the files and folders within the .tar file.
3. Extract the five folders inside of 2D\_Spiral.tar. These folders are called *layout*, *macros*, *mfiles*, *parfiles*, and *psgfiles*.
4. Copy all the contents within the *layout* folder to `/home/<USERNAME>/vnmrsys/templates/layout/`. From here on out <USERNAME> is your username on the system.
5. Copy all the contents within the *macros* folder to `/home/<USERNAME>/vnmrsys/maclib/`.
6. Copy the contents of *mfiles* to any folder you wish to use for MATLAB based reconstruction.
7. Copy the contents of *parfiles* into the folder `/home/<USERNAME>/vnmrsys/parlib/`.
8. Copy the contents of *psgfiles* into the folder `/home/<USERNAME>/vnmrsys/psglib/`.

### A2.5.2 File Modification

1. Open `/home/<USERNAME?>/psglib/spiralsgl.c` in a text editor.

This is the command that will record the gradient waveforms calculated for each imaging experiment

2. On lines 76-79, Change `"/home/histo/Spiral/<FILENAME>.GRD"`, to a folder of your choosing. Using `"/home/<USERNAME>/Spiral/<FILENAME>.GRD"` will be the most convenient. You can change `<FILENAME>` if you want. But if you do, you will have to account for that change in the matlab reconstruction algorithms.

3. Save changes and exit.

4. Open `/home/<USERNAME>/maclib/getGrads` in a text editor.

This command copies the waveforms calculated by `spiralsgl.c` and pastes them into `/home/<USERNAME>/vnmrsys/data/<CURRENTSTUDY>/Waveforms`, where `<CURRENTSTUDY>` is the name of the active study. IE: `s_2013050301/`.

5. On line 5, change `"shell('cp ~/spiral/*.GRD ./Waveforms/')` to `"shell('cp <FILE> ./Waveforms/')` where `<FILE>` is the path you input into lines 76-79 of `spiralsgl.c`.

6. Save changes and exit.

### A2.5.3 Compilation

Compile the pulse sequences by opening a terminal and entering the following commands

- a `seqgen KyMap.c`
- b `seqgen KxMap.c`
- c `seqgen spiral.c`

Should the compiler fail altogether, it will output a series of errors that should help you find out what has gone wrong.

And you are done! At this point you should be able to open `vnmrj` and acquire a spiral readout.

## A2.6 Imaging

The current installation of spiral imaging only supports images taken along the axial plane. The user can choose between a spiral-out and a spiral-in trajectory.

Image acquisition can be done with or without trajectory mapping. As of right now (February 2013), I highly recommend taking advantage of the trajectory mapping.

However, in either case imaging is broken down into three steps: 1) use the appropriate macro to call up the pulse sequences you need, 2) set the correct parameters—which can be a bit tricky with the `vnmrj` parameter “`np`”—and then 3) acquire data.

### A2.6.1 Acquiring a Spiral K-Space Image

1. Load the sample, tune the rf coil, calibrate the center frequency and 90 degree tip power, and shim the magnetic field.
2. In the `Vnmrj` command line, type in the command “`spiral`.”
3. This activates the “`spiral`” macro which will load in some default parameters and activates the “`spiral GUI`”.
4. Use the GUI to set whatever parameters you require. These may include FOV, matrix size, spectral width, number of interleaves, etc.
5. Choose whether you want a spiral-in or spiral-out trajectory by toggling the button “`spiral-in`.”
6. Make sure that the number next to the field “Number of Points” equals the number next to the button “Set np to this.” If the numbers are unequal, repeatedly push the button “Set np to this” until they are.
7. This button activates the macro `npSet`.
8. The macro calculates how many complex points should be acquired during the length of the spiral and then sets the variable `np` to that number.
9. This button is necessary to prevent `vnmrj` from assuming a cartesian imaging grid and resetting the variable `np` at the moment of acquisition. This would otherwise prevent you from acquiring a full data set.
10. You may have to press this button a few times to get the value `np` to match the number next to the button.
11. When all the variables are as you wish, press “`go`” to acquire.
12. When you do press “`go`”, the value next to the “Set np to this” button may suddenly change to a very small number like 2332. So long as the `vnmrj` variable `np` and this number were equivalent before you pressed `go` and `np` remains unchanged after, the

sudden change should not pose a problem to acquisition. The button was invented to prevent that sudden change happening to np. I do not know the exact nature of this bug, but if you do, let me know so I can stop it!

13. After successful image acquisition, type in “getGrads” into the vnmrj command line.
14. getGrads copies the waveforms calculated by spiralsgl.c and pastes them into `/home/<USERNAME>/vnmrsys/data/<CURRENTSTUDY>/Waveforms`, where `<CURRENTSTUDY>` is the name of the active study. IE: `s_2013050301/`.
15. In the current reconstruction setup, these must then be moved into `<CURRENTSTUDY>/spiral_<currentScan>.fid`. Unfortunately, this must be done manually as MAGICAL programming does not store the name of the last acquired scan.
16. Once the trajectories are copied over into the current study folder, you can reconstruct a preliminary image. However, I recommend you go on to acquire the k-space trajectory as well.

#### **A2.6.2 Acquiring a Spiral K-Space Trajectory Measurement**

1. After acquiring a spiral acquisition, enter the command “KxMap.” into the Vnmrj command line.
2. This command should call up the parameters and interface for the sequence *KxMap*.
3. *KxMap* excites and acquires FID’s from 2 identical slices separated along the  $x$ -direction.
4. The sequence plays out a spiral sequence with the  $y$ -axis gradient turned off. It then repeats the same process both the  $x$  and  $y$  gradients turned off.
5. The difference between the phase of the signals from each slice is proportional to the the Kx trajectory, plus the small baseline reference phase.
6. This baseline reference is recorded by the sequence where all gradient channels are turned off.
7. Once the interface for *KxMap* is called up, set the parameters *lro*, *Mat*, *Nint*, *sm*, and *np* identical to those of the spiral sequence used to acquire an image. However, leave the slice orientation--which should be “sagittal”-- alone.
8. Center the two sagittal slices on regions that have potential for a homogenous field with strong SNR. Make the slices as thin as you can and still get reasonable SNR. Make sure the slices are only separated along the  $x$  direction.

9. Press *GO* to acquire the FID information. The scan will acquire FIDs from each slice. Half of the FIDs will be acquired with only x-axis gradient channel on and half will be acquired with both gradient axes channels off for reference.
10. Once *KxMap* has finished, type in the command “*KyMap*” into the *Vnmrj* command line to set up the interface for the sequence *KyMap*.
11. *KyMap* behaves exactly like *KxMap* except that it selects two slices that are separated along the *y*-direction.
12. Set the parameters *lro*, *Mat*, *Nint*, *sw*, and *np* for *KyMap* to be identical to those used for *KxMap*.
13. Make sure the orientation for *KyMap* is set to “coronal.”
14. Center the two coronal slices on regions that have potential for a homogenous field with strong SNR. Make the slices as thin as you can and still get reasonable SNR. Make sure the slices are only separated along the *y* direction.
15. Note, for this to work, there must be some nonzero distance between the two slices.
16. Press *go* to acquire the FID information.
17. And you are done!

## A2.7 Reconstruction

The current version of *Vnmrj* (3.1) does not support image reconstruction using non-uniform k-space samples. Fortunately, some of the best brains in the reconstruction business are not only closely affiliated with the University of Michigan but provide reconstruction software for free! Included in this installation are reconstruction toolboxes by Jeff Fessler and Brian Hargreaves. For an example of image reconstruction, see *reconExample.m* or examples in the respective toolboxes.

## A2.8 Support

Listed below are different functions, both in *c#* and *matlab*, that are used in this spiral installation.

### A2.8.1 Psg files

The following is a list of the two psg functions that are used for the spiral programming. These are used in *KxMap.c*, *KyMap.c*, and *spiral.c* to compute the spiral waveforms.

#### calcSpiral

Syntax: calcSpiral(SPIRAL\_GRADIENT\_T \*sg);

Description: Calculates a 2D spiral readout gradient using the parameters stored in structure sg. Checks the waveforms against slew rate and amplitude constraints. Adds a ramp to zero after the spiral readout. Prints the gradient waveform to *~/vnmrsys/home/shapelib<Gx, Gy>.GRD* in scaled DAQ units and to *~/<FILE OF YOUR CHOICE>/<Gx, Gy, Th, dth>.GRD* in G/cm.

Inputs: \*sg. Pointer to structure type SPIRAL\_GRADIENT\_T. Structure sg is initialized with

command *initSpiral*.

Outputs: Void

#### initSpiral

Syntax: *initSpiral (SPIRAL\_GRADIENT\_T \*sg, double gamp, double lro, double Mat, int Nint );*

Description: Initialize the the structure sg of type SPIRAL\_GRADIENT\_T with default values.

Inputs: \*sg. Type SPIRAL\_GRADIENT\_T. Pointer to the structure sg. sg stores pertinent parameters necessary to calculate the spiral readout.

gamp. Type double. Maximum gradient amplitude. Absolute value of spiral waveform will not exceed this value. G/cm.

lro. Type double. Vnmrj's variable for the field of view of the desired image. Cm.

Mat. Type double. Matrix size of the desired image.

Nint. Type double. Number of shots for the spiral image. IE. Nint = 1 means single shot spiral imaging.

Outputs: Void.

Comments: *initSpiral* sets up the following defaults for the following structure fields.

Structure Field	Default Value	Comments
Type	GENERIC_GRADIENT_TYP E	I don't know why this is necessary, but it makes things work easier.

Amp	gamp	Maximum spiral gradient amplitude. G/cm
Display	sgldisplay	Future dps support
Fov	lro	Image FOV. cm.
phaseIncrement	0	Legacy option
numInterleaves	Nint	Number of shots per image.
maxGrad	GRAD_MAX	System's maximum gradient amplitude. G/cm
Name	"spiral_	Legacy option
numPoints	0.	Length of waveform in points
Polarity	FALSE	Flag for suddenly changing gradient polarity.
Resolution	GRADIENT_RES	System granularity. 4 microseconds.
Rollout	ROLLOUT	Write to file in uncompressed format.
slewRate	MAX_SLEW_RATE	Maximum system slew rate.
spiralln	FALSE	Future spiral in/out option.
Gamma	nuc_gamma()	Current nucleus gyromagnetic ratio.
writeToDisk	TRUE	Flag to write gradient to disk.
matrixSize	Mat	Desired image matrix size
Duration	0	Duration of spiral waveform plus the ramp to zero at the end. Seconds
spiralDuration	0	Duration of the spiral portion of the waveform. Seconds
moment0	0	Zerth gradient moment. Radians
moment1	0	First gradient moment. Seconds

## A2.8.2 Matlab Files

The following are descriptions of matlab files I have written to ease the preprocessing that is necessary before image reconstruction.

### **getFid**

Function to upload an fid recorded by vnmrj

[Fid, procparr] = getFid(directory)

Inputs: directory: string location of the fid and it's associated parameter file.

Outputs: Fid: Free induction decay. A n x m matrix of complex points that is the free

induction decay recorded by Vnmrj.

procparr: Structure containing Vnmrj acquisition parameters

### **getIdealGrads**

Function for getting the calculated ideal gradients and their respective K-space trajectories. The function then goes on to upsample both to the same time step as the sample acquisition. Gradient waveforms are assumed to be in G/cm

[G, K] = getIdealGrads(fileLocation, fileName, gradTimeStep, sw, spirallength);

Inputs: fileLocation: String. Path to the file containing the gradient waveform.

fileName: String. Name of file which contains the gradient waveform

gradTimeStep: Double. Granularity of gradient waveform in seconds.

sw: Double. Sampling rate (spectral width) of imaging acquisition in Hz.

spirallength: Array of [1:Number of Points] acquired during imaging acquisition or single of length in seconds of array.

Outputs: G: Gradient waveforms upsampled by interpolation to the same grid as

(1:spirallength)/sw

K: Time integral of Gradient waveform. K =

cumsum(G)\*gradTimeStep;

interpolated to the same grid to which G is interpolated.

### **getTraj**

Function to get Measure Kx, Ky trajectories for a particular object.

[KTraj] = getTraj(fileLocation, referenceLocation, dgap, sw)

Inputs: fileLocation: String. Location of the .fid file produced by Vnmrj which contains the FID of the desired scan.



Ex: /Home/<User>/vnmrsys/data/<study>/<scan>.fid.

Trajectories are obtained by subtracting a the phase of the signal from two slices seperated along one dimension. See (Duyn JG, et al. May 1998. Simple Correction Method for K-Space Trajectory Deviations in MRI. J Magn Reson. 132(1):150:3.)

### **matlabRegrid**

Function using matlab's griddata command to regrid spiral data onto a cartesian grid.

`kSpace = matlabRegrid(K,spData,FOV,Mat,gridSize)`

Inputs: K: complex Nx1 or Nx2 vector in the of each sample's K-space location

IE:  $K = [K_x \ K_y]$  or  $K_x + i*K_y$ . Units: cycles/cm.

spData: Nx1 complex points of the estimate of K space at the points in K.

FOV: Field of view of the acquisition Units: cm

Mat: Intended size of the reconstructed image.

gridSize: size of the grid on which to interpolate the reconstructed data.

Outputs: kSpace: Interpolation of spiralData onto a gridSize X gridSize array of complex

points.

Gridsize covers locations `linspace(-Mat/FOV/2,Mat/FOV/2,gridSize)`.

### **nufftRecon**

Function to reconstruct spiral data using Jeff Fessler's IRT programs. Uses the matrix2 formulation for iNUFFT regridding and weighted least squares with roughness penalization.

Installation of IRT is prerequisite before using this program. [\[Is that the name of Jeff's Toolbox?\]](#)

`nufftRecon(studyPath,spiralScanName, KxTrajectory,KyTrajectory);`

Inputs: studyPath: String. Top directory of study folder containing the .fid folders of the

scans in question.

Ex: '/home/<user>/vnmrsys/data/<study name>';

spiralScanName: String. Name of the .fid folder of the scan you wish to reconstruct. Ex: 'spiral\_01.fid';

KxTrajectory: (optional) String. Name of the .fid folder containing Kx encoding

FID data. Ex: 'KxMap\_02.fid';

KyTrajectory: (optional) String. Name of the .fid folder containing Ky encoding

FID data. Ex: 'KyMap\_02.fid';

Outputs: picture: Inverse Fast Fourier Transform of Regridded K-Space data.

### **readfid**

Function that reads in binary .fid file created by Vnmrj.

[dta, fheader, bheader] = readfid(filename,n);

inputs: filename: vnmr fid file to read

n: number of points at the end of fid to use for baseline correction (-1 = no correction)

Outputs: dta: returned fid

fheader: returned fid file header information

bheader: returned fid block header information for the last block that was read.

### **reconExample**

An example of possible ways to use these functions for reconstruction. See the actual file for details.

### **reconstructGREImageArrayed**

Function to Reconstruct Raw data from a multi slice Gems Sequence acquired with an arrayed parameter. For example, acquisitions were made at several echo times or band widths.

This function can only reconstruct images sampled on a Cartesian grid.

[imageMatrix, kSpaceMatrix, procpa] = reconstructGREImageArrayed(fileLocation)

Inputs: fileLocation: String. Location of the .fid file containing the FID file of the acquired

images

Outputs: imageMatrix: NxN complex matrix which is the reconstructed image

kSpaceMatrix: NxN complex matrix which is the cartesian samples of the

object in K-Space.

procpa: Structure containing Vnmrj imageing parameters.

### **reconstructGREImage**

Function to Reconstruct Raw data from a multi slice Gems Sequence.

This function can only reconstruct images sampled on a Cartesian grid.

[imageMatrix, kSpaceMatrix, procpa] = reconstructGREImage(fileLocation)

Inputs: fileLocation: String. Location of the .fid file containing the FID file of the acquired images

Outputs: imageMatrix: NxN complex matrix which is the reconstructed image

kSpaceMatrix: NxN complex matrix which is the cartesian samples of the object in

K-Space.

procpar: Structure containing Vnmrj imaging parameters.

### **rotclockwise**

Function to rotate a vector counter-clockwise with respect to the x,y coordinate frame.

returnVector = rotclockwise(inputVector, angle)

Inputs: inputVector: a nx2 vector in the form [x coords, ycoords].

angle: angle of rotation in radians

Outputs: returnVector = inputVector\*rotationMatrix(angle);

### **rotTraj**

Function to rotate k space trajectories using a simple rotation matrix at angles spaced equally about the unit circle: [0 pi/Nint, 2\*pi/Nint, ..., (Nint-1)\*2\*pi/Nint]

[trajVec, trajMat] = rotTraj(Trajectory, nInt);

Inputs: Trajectory: is a nx2 vector: [xcoords,ycoords];

Nint: The number of interleaves used during imaging

Outputs: trajVec: A (length(phaseAngles)\*n)x2 vector where each rotated trajectory is concatenated onto trajVec

trajMat: A Nint X length(phaseAngles) X 2 matrix containing the rotated trajectories in the columns.

EX: to access xcoords rotated by  $2\pi n/Nint$  radians  
enter xTraj\_n = trajMat(:,n,1);

### **setPathRecon**

File to add the reconstruction toolboxes to the MATLAB search path.

### **spiralTrajectoryMap**

Program which can map out and compare the angle between the designed spiral trajectory and what is measured.

### **tryreadprocpar**

reads Vnmrj produced procpar parameter files into a matlab structure.

procpar = tryreadprocpar(procdir,verbose)

Inputs: directory: String. Location of desired procpar file.

verbose: (optional) 0 is default.

Outputs: procpar: Matlab structure containing procpar variables.

## **A2.9 Source Code of Spiral Sequence**

## A2.9.1 Spiral.c

This is the main spiral imaging sequence

```
/*
 * Varian, Inc. All Rights Reserved.
 * This software contains proprietary and confidential
 * information of Varian, Inc. and its contributors.
 * Use, disclosure and reproduction is prohibited without
 * prior consent.
 */

/*****
 * Spiral Gradient Echo Acquisition
 *****/

#include <standard.h>
#include "histosgl.c"

pulsesequance()
{
    /* Internal variable declarations *****/
    double freqEx[MAXNSLICE];
    double maxgradtime,perTime,temin,trtime,te_delay,tr_delay;
    double Mat, Gamp; //Reconstruced Image matrix size and designed gradient
amplitude
    int table,shapeEx;
    char spoilflag[MAXSTR],mriout[MAXSTR],slprofile[MAXSTR];
    int listid,i,Nint; // Id for phase shift for interleaves, counting iteger,
number of interleaves
    double int_steps, intPhase, phaseStep; //Used to calculate phase rotation of
logical axis during interleaving.
    char spiral_in[MAXSTR]; // Marker if spiral-in trajectory
    int psi_0, phi_0, theta_0; // Place holders for the original rotation
angles of the phase encode ro axes.

    /* Real-time variables used in this sequece *****/
    int vint_steps = v1; // Number of interval steps
    int vintPhase = v2; // Phase of current interval step
    int vms_slices = v3; // Number of slices
    int vms_ctr = v4; // Slice loop counter
    int vpe_offset = v5; // PE/2 for non-table offset
    int vssc = v8; // Compressed steady-states
    int vacquire = v9; // Argument for setacqvar, to skip steady state
acquisitions
    int vrfspoil_ctr = v10; // RF spoil counter
    int vrfspoil = v11; // RF spoil multiplier
    int vtrimage = v12; // Counts down from nt, set trimage delay when 0
    int vtrigblock = v13; // Number of slices per trigger block
    int vNint = v14; // interval loop counter
    int vphaseStep = v15; // step size of phase difference between
intervals.
    int vIdx = v16; // variable to hold the correct index of the
phase rotation

    /* Declare spiral gradients*/
    SPIRAL_GRADIENT_T sp; //Intialize the spiral gradient

    /* Declare rewinder gradients*/
    GENERIC_GRADIENT_T sprGx; // Rewinder for the X direction
    GENERIC_GRADIENT_T sprGy; // Rewinder for the Y direction

    /* Initialize paramaters *****/
    sw = getval("sw");
    init_mri();
    getstr("spoilflag",spoilflag);
    getstrnwarn("mriout",mriout);
    getstrnwarn("slprofile",slprofile);
    Nint = getval("Nint");
}
```

```

Mat = getval("Mat");
Gamp = getval("Gamp");
getstr("spiral_in", spiral_in);

/* Set Rcvr/Xmtr phase increments for RF Spoiling *****/
/* Ref: Zur, Y., Magn. Res. Med., 21, 251, (1991) ****/
if (rfspoil[0] == 'y') {
    rcvrstepsize(rfphase);
    obsstepsize(rfphase);
}

/* Initialize gradient structures *****/
init_rf(&pl_rf,plpat,pl,flipl,rofl,rof2 ); // excitation pulse
init_slice(&ss_grad,"ss",thk); // slice select gradient
init_slice_refocus(&ssr_grad,"ssr"); // slice refocus gradient
initSpiral(&sp, Gamp, lro,Mat, Nint); // Spiral Gradient
initGeneric(&sprGx); // Generic Gradient to rewind
the spirals
initGeneric(&sprGy); // Generic Gradient to rewind the spirals

/* RF Calculations *****/
calc_rf(&pl_rf,"tpwrl1","tpwrlf");

/* Gradient calculations *****/
if (spiral_in[0] == 'y') {
    sp.spiralIn = TRUE;
}
calcSpiral(&sp);
calc_slice(&ss_grad,&pl_rf,WRITE,"gss");
calc_slice_refocus(&ssr_grad,&ss_grad,WRITE,"gssr");

/* Check for errors in the spiral waveform */
if (sp.errorX==TRUE || sp.errorY==TRUE){
    abort_message("Spiral Slew Rate Error");
}

/* Calculate the rewinder gradients */
sprGx.calcFlag = DURATION_FROM_MOMENT_AMPLITUDE; // Make the gradient 0th
moment equal to that of the spiral gradient
sprGy.calcFlag = DURATION_FROM_MOMENT_AMPLITUDE;
sprGx.m0 = sp.GxMoment0;
sprGy.m0 = sp.GyMoment0;
sprGx.amp = sp.amp; //Make the gradient
amplitude equal to that of the spiral gradients
sprGy.amp = sp.amp;
calcGeneric(&sprGx); // Calculate the gradient
waveforms
calcGeneric(&sprGy);
calc_sim_gradient(&sprGx, &sprGy, &null_grad,0,WRITE); // Equalize durations
of sprGx and sprGy.

/* Calculate spectral width and number of points to sample*/
sw = getval("sw");
np = 2*(int)((sp.spiralDuration*sw));
putvalue("npIdeal",np);

/*Export spiral structure parameters to vnmrj pocpar parameters for
reconstruction */
putvalue("spGamp",sp.amp); // Maximum amplitude of the spiral pulse
waveform
putvalue("spNumPoints",sp.numPoints); // Number of points in the spiral
putvalue("spResolution",sp.resolution); // Time resolution of points in the
spiral waveform
putvalue("spSlewRate",sp.slewRate); // Slew Rate of the calculated spiral
waveform
putvalue("spIn",sp.spiralIn); // True if a Spiral-in Spiral, False if
Spiral out.
putvalue("spDuration",sp.duration); // Duration (in seconds) of the spiral
waveform
putvalue("spRampDuration",sp.rampDuration); // Duration (in seconds) of the
ramp down at the end of the spiral

```

```

        putvalue("spSpiralDuration",sp.spiralDuration); // Duration of the spiral
portion of the total gradient waveform
        putvalue("spGxMoment0",sp.GxMoment0); // Zeroth Moment of Gx
        putvalue("spGxMoment1",sp.GxMoment1); // First Moment of Gx
        putvalue("spGyMoment0",sp.GyMoment0); // Zeroth Moment of Gy
        putvalue("spGyMoment1",sp.GyMoment1); // First Moment of Gy

        /* calculate the number of intervals and create the rotation list. */
        psi_0 = psi; // Place holder of the image rotation angles
        phi_0 = phi; // Place holder of the image rotation angles
        theta_0 = theta; // Place holder of the image rotation angles
        printf("psi is %f, phi is %f, theta is %f\n", psi, phi, theta);
        nv = Nint;
interval    phaseStep = 360/Nint; // phase rotation of the gradient waveform in each

        intPhase = 0; // initial phase rotation.
        putvalue("nv",nv);
        double angle_array[Nint+1][3];
        for (i = 0; i<=Nint+1; i++){
            angle_array[i][1] = phi_0 + intPhase; // //phi psi_0; // psi
            angle_array[i][2] = theta_0; // theta
            angle_array[i][3] = psi_0; // phi //phi 0 + intPhase; // phi
            // printf("psi is %f theta is %f phi is %f\n",
angle_array[i][1],angle_array[i][1],angle_array[i][3]);
            intPhase+=phaseStep;
        }
        listid = create_rotation_list("intervalPhase",angle_array, Nint+1);

        /* Check that all Gradient calculations are ok *****/
        sgl_error_check(sglerror);

        /* Min TE *****/
        temin = ss_grad.rfCenterBack + alfa +ssr_grad.duration;
        if (spiral_in[0] == 'y') {
            temin = temin+sp.duration;
        }

        if (minte[0] == 'y') {
            te = temin;
            putvalue("te",te);
        }
        if (te < temin) {
            abort message("TE too short. Minimum TE= %.2fms\n",temin*1000+0.005);
        }
        te_delay = te - temin;

        /* Check nsblock, the number of slices blocked together
        (used for triggering and/or inversion recovery) */
        check_nsblock();

        /* Min TR *****/
        trmin = ss_grad.duration + te_delay + ssr_grad.duration + sp.duration + 2*8e-
6;

        /* Adjust for all slices *****/
        trmin *= ns;

        if (mintr[0] == 'y') {
            tr = trmin;
            putvalue("tr",tr);
        }
        if (FP_LT(tr,trmin)) {
            abort_message("TR too short. Minimum TR = %.2fms\n",trmin*1000+0.005);
        }

        /* Calculate tr delay */
        tr_delay = granularity((tr-trmin)/ns,GRADIENT_RES);

        /* Set up frequency offset pulse sDSPhape list *****/

```

```

offsetlist(pss,ss_grad.ssamp,0,freqEx,ns,seqcon[1]);
shapeEx =
shapelist(plpat,ss_grad.rfDuration,freqEx,ns,ss_grad.rfFraction,seqcon[1]);

/* Set int_steps for profile or full image *****/
int_steps = nv;
F_initval(int_steps/2.0,vpe_offset);

/* Shift DDR for pro *****/
roff = -poffset(pro,ro_grad.roamp);

/* Adjust experiment time for VnmrJ *****/
if (ssc<0) {
    if (seqcon[2] == 'c') g setExpTime(trmean*(ntmean*int_steps*arraydim -
ssc*arraydim));
    else g setExpTime(trmean*(ntmean*int_steps*arraydim -
ssc*int_steps*arraydim));
}
else g_setExpTime(trmean*ntmean*int_steps*arraydim + tr*ssc);

/* PULSE SEQUENCE *****/
status(A);
rotate(); // Initialize default orientation
triggerSelect(trigger); // Select trigger input 1/2/3
obsoffset(resto);
delay(4e-6);
initval(fabs(ssc),vssc); // Compressed steady-state counter
if (seqcon[2]=='s') assign(zero,vssc); // Zero for standard peloop
assign(zero,vrfspoil_ctr); // RF spoil phase counter
assign(zero,vrfspoil); // RF spoil multiplier
assign(one,vacquire); // real-time acquire flag
setacqvar(vacquire); // Turn on acquire when vacquire is zero
assign(zero,vIdx); // Assign variable to keep track of which
rotation angle to use
/* trigger */
if (ticks > 0) F_initval((double)nsblock,vtrigblock);

/* Begin phase-encode loop *****/
peloop(seqcon[2],int_steps,vint_steps,vNint);

if (trtype) delay(ns*tr_delay); // relaxation delay

/* Compressed steady-states: 1st array & transient, all arrays if ssc is
negative */
if ((ix > 1) && (ssc > 0)){
    assign(zero,vssc);
    sub(vNint,vssc,vNint); // vNint counts up from -ssc
    assign(zero,vssc);
    if (seqcon[2] == 's')
        assign(zero,vacquire); // Always acquire for non-compressed loop
    else {
        ifzero(vNint);
        assign(zero,vacquire); // Start acquiring when vNint reaches zero
        endif(vNint);
    }
}

/* Set rcvr/xmtr phase for RF spoiling *****/
if (rfspoil[0] == 'y') {
    incr(vrfspoil_ctr); // vrfspoil_ctr = 1 2 3 4 5 6
    add(vrfspoil,vrfspoil_ctr,vrfspoil); // vrfspoil = 1 3 6 10 15 21
    xmtrphase(vrfspoil);
    rcvrphase(vrfspoil);
}

/* Begin multislice loop *****/
msloop(seqcon[1],ns,vms_slices,vms_ctr);

if (!trtype) delay(tr_delay); // Relaxation delay

if (ticks > 0) {

```

```

        modn(vms_ctr,vtrigblock,vtest);
        ifzero(vtest); // if the beginning of an trigger
block
        xgate(ticks);
        grad_advance(gpropdelay);
        delay(4e-6);
        elsenz(vtest);
        delay(4e-6);
        endif(vtest);
    }

    splon(); delay(4e-6); splloff(); // Scope trigger

    /* Slice select RF pulse *****/
    obspower(pl_rf.powerCoarse);
    obspwrf(pl_rf.powerFine);
    delay(4e-6);
    obl_shapedgradient(ss_grad.name,ss_grad.duration,0,0,ss_grad.amp,NOWAIT);
    delay(ss_grad.rfDelayFront);
    shapedpulselist(shapeEx,ss_grad.rfDuration,oph,rof1,rof2,seqcon[1],vms_ctr);
    delay(ss_grad.rfDelayBack);

    /* refocus gradient *****/
    obl_shapedgradient(ssr_grad.name,ssr_grad.duration,0,0,-ssr_grad.amp,WAIT);

    /* rotate the gradient axis */
    add(one,vNint,vIdx);
    rot_angle_list(listid,'c',vIdx);
    if (sp.spiralIn == TRUE) {
        delay(te_delay-sp.duration- alfa);
    }
    else {
        delay(te_delay-alfa); // delay between rf pulse and acquisition
    }

    /* Some logic control for spiral out or spiral in */
    if (sp.spiralIn==TRUE) {
        obl_shaped3gradient(sprGx.name,
        sprGy.name,"",sprGy.duration,sprGx.amp,sprGy.amp,0,WAIT);
        delay(4e-6);
    }

    /* Readout gradient and acquisition *****/
    startacq(alfa);
    obl_shaped3gradient(sp.nameX,sp.nameY,"",sp.duration,sp.amp,sp.amp,0,NOWAIT);
    if (spiral_in[0] == 'y') {
        delay(granularity(sp.duration-sp.spiralDuration,GRADIENT_RES));
    }
    acquire(np,1.0/sw);
    endacq();
    delay(granularity(sp.duration-sp.spiralDuration, GRADIENT_RES)); // Delay for
ramp down portion of the sequence
    delay(20e-6); // For some reason this delay has to be here. Perhaps because
of sampling granularity

    /* Some logic control for spiral out or spiral in*/
    if (sp.spiralIn==FALSE) {
        obl_shaped3gradient(sprGx.name, sprGy.name,"",sprGy.duration,-sprGx.amp,-
sprGy.amp,0,WAIT);
        delay(4e-6);
    }

    /* Rotate back into the default reference frame to excite the next slice*/
    rotate();

    endmsloop(seqcon[1],vms_ctr);

    /* Optional output control examples *****/
    if (mriout[0]=='b' || mriout[1]=='b')

```



```

        writeMRIUserByte(vNint);
        if (mriout[0]=='g' || mriout[1]=='g')
            setMRIUserGates(vNint);

        /* increase the rotation phase of the spiral gradient by phaseStep */
        endpeloop(seqcon[2],vNint);

        /* Inter-image delay *****/
        sub(ntrt,ct,vtrimage);
        decr(vtrimage);
        ifzero(vtrimage);
        delay(trimage);
        endif(vtrimage);

        calc_grad_duty(tr);
    }

```

## A2.9.2 Spiralsgl.c

This file is a library used by *spiral.c*.

```

/* File contains intialization functions and calculations functions for a spiral
gradient readout.

```

```

Made by Steven Allen, Univeristy of Michigan, 2012*/

```

```

/* Added Spiral out functionality SA March 8 2013 */

```

```

/*****
/*****
/***** S P I R A L P U L S E F U N C T I O N S *****/
/*****
/*****

```

```

/*****
Function Name:   calcSpiral
Example:         calcSpiral(&sg);
Description:     Calculates the wave form of a spiral gradient using an
approximation method in Glover (1999) Simple Analytic Spiral K-Space Algorithm.

```

Input

```

Formal:  *sg - pointer to a spiral gradient structure
Private: none
Public:  GRAD MAX - maximum possible gradient amplitude

```

Output

```

Return:  None
Formal:  *sg - pointer to spiral gradient structure

```

Versions: Nov 29 2012 Slew rate limited spirals only

```

*****/
#include <stdio.h>
#include <math.h>
#include "spiralsgl.h"

```

```

void calcSpiral (SPIRAL_GRADIENT_T *sg)

```

```

{
    /* Calculate a Spiral Out Sequence*/
    calcSpiralOut(sg);

    if (sg->spiralIn==TRUE)
    {
        reverseToSpiralIn(sg);
    }

```

```

    /* check for slew rate errors */

```

```

    sg->errorX = checkSlewRate(sg->Gx, sg->numPoints, sg->Gx[0], GRADIENT_RES);
    sg->errorY = checkSlewRate(sg->Gy, sg->numPoints, sg->Gy[0], GRADIENT_RES);

```

```

    /* Calculate the zeroth and first moment*/
    /*Gx Moment*/
    calculateMoments(sg->Gx, (long) (sg->numPoints), 0,sg->Gx[0], GRADIENT_RES, &sg-
>GxMoment0, &sg->GxMoment1,0,0);
    /*Gy Moment*/
    calculateMoments(sg->Gy, (long) (sg->numPoints), 0,sg->Gy[0], GRADIENT_RES, &sg-
>GyMoment0, &sg->GyMoment1,0,0);

    /* Compute and export the maximum calculated gradient amplitude*/
    sg->amp = findMax(sg->Gx, (long) (sg->numPoints),sg->Gx[0]);

    /* Write to file */
    writeToDisk(sg->Gx, (long) (sg->numPoints), sg->Gx[0], GRADIENT_RES, TRUE, sg-
>nameX);
    writeToDisk(sg->Gy, (long) (sg->numPoints), sg->Gy[0], GRADIENT_RES, TRUE, sg-
>nameY);
}

/*****

function Name:  calcSpiralOut
Example:        calcSpiral(&sg);
Description:    Calculates spiral gradient using an approximation method in
Glover (1999) Simple Analytic Spiral K-Space Algorithm.

Input
    Formal:  *sg - pointer to a spiral gradient structure
    Private: none
    Public:  GRAD MAX - maximum possible gradient amplitude

Output
    Return:  None
    Formal:  *sg - pointer to spiral gradient structure
*****/

void calcSpiralOut(SPIRAL_GRADIENT_T *sg)
{
/* Declare variables used for calculation*/

double  gamma; // Gyromagnetic Ratio (?)

double dt; // Time step (s)
double S0; // Maximum Slew Rate (G/cm/s)
int i, j, n; // place holders for loops
double Ts, ts;
double sp theta = 0;
double dthdt, thetas, x, y, Tta; // time and angle holders
double Amp;
double a2, beta; /*/ terms necessary for calculation of spiral pattern*/
double c, s; // terms for calculating each gradient waveform
double spGmax; // Maximum gradient strength. G/cm
double Sabs; // Absolute Slew rate magnitude
double Gabs; // Actual Gradient magnitude (G/cm)
double q; // slewrate modifying paramater for spiral performance.
double fov; // Field of view (cm)
int Mat,Nint; // Desired Matrix size, Number of interleaves
double t=0;
FILE *gxfh, *gyfh, *thfh, *dthfh;
double Gx[250000], Gy[250000]; // absolute gradient strength and maximum gradient
strength.

/* compute a preliminary constants for the calculation to come*/
q = 5; // This number must be 1 or larger. See the reference paper.
S0 = (sg-> slewRate); // G/cm/s
gamma = sg->gamma; // Hz/G
fov = sg->fov; // cm

```

```

Nint = sg->numInterleaves; // # of Interleaves
Amp = Nint/(2*M_PI*fov); // Amplitude of Spiral K-space trajectory
beta = S0*gamma/Amp; // Gradient amplification factor
a2 = pow((9*beta/4),0.333334); // Useful term to compute
spGmax = sg->amp; // Max gradient G/cm
Mat = sg->matrixSize; // Matrix resolution

/* Useful estimates of the time it takes to acquire the spiral*/
Ts = 0.666667/((double)Nint)*sqrt(pow((double)Mat*M_PI, 3)/(2*M_PI*gamma*fov*S0));
//Time to completion in slew rate limited case
ts = pow(3*gamma*spGmax/(2*Amp*a2*a2),3); // Time to maximum gradient amplitude
achieved

/*Get the file handle for writing.*/
gxfh = fopen("/home/histo/Spiral/Gx.GRD", "w");
gyfh = fopen("/home/histo/Spiral/Gy.GRD", "w");
thfh = fopen("/home/histo/Spiral/Th.GRD", "w");
dthfh = fopen("/home/histo/Spiral/dth.GRD", "w");

/* Slew Rate Limited Spiral Calculation*/
i = 0;
for (sp_theta = 0; sp_theta <= Mat*M_PI/Nint; t+=GRADIENT_RES) {
x = pow(t, 1.333333);
y = q+0.5*beta/a2*x;
sp_theta = 0.5*beta*t*t/y;
dthdt = beta*t*(q+0.166667*beta/a2*x)/(y*y);
c = cos(sp_theta);
s = sin(sp_theta);
sg->Gx[i] = Nint/(fov*gamma*2*M_PI)*dthdt*(c-sp_theta*s);
sg->Gy[i] = Nint/(fov*gamma*2*M_PI)*dthdt*(s+sp_theta*c);

/* write the gradients to a file in an appending sort of way*/
fprintf(gxfh,"%f\n",sg->Gx[i]);
fprintf(gyfh,"%f\n", sg->Gy[i]);
fprintf(thfh,"%f\n", sp_theta);
fprintf(dthfh,"%f\n",dthdt);

/* if statement to ensure that maximum gradient amplitude is not exceeded*/
Gabs = hypot(sg->Gx[i],sg->Gy[i]);
if (Gabs >= spGmax){
if (Gabs > hypot(spGmax/sp_theta,spGmax)) { i++; break;}
}
i++;
} /* end the slew rate limited approximation*/

/* Check to see if spiral sequence is finished. If not use amplitude limited
design*/
thetas = sp_theta; ts = t;
if (thetas < Mat*M_PI/Nint){
Tta= ts+M_PI*Amp/(2*M_PI*gamma)/spGmax*(pow(Mat*M_PI/Nint,2)-(thetas*thetas));

/*Compute the amplitude limited waveform*/
for (t = ts+GRADIENT_RES; sp_theta <= Mat*M_PI/Nint; t+=GRADIENT_RES){
sp_theta = sqrt(thetas*thetas+2*gamma*spGmax/Amp*(t-ts));
dthdt = gamma*spGmax/Amp/sp_theta;
c = cos(sp_theta);
s = sin(sp_theta);
sg->Gx[i] = spGmax*(c/sp_theta-s);
sg->Gy[i] = spGmax*(s/sp_theta+c);
fprintf(gxfh,"%f\n",sg->Gx[i]);
fprintf(gyfh,"%f\n",sg->Gy[i]);
fprintf(thfh,"%f\n",sp_theta);
fprintf(dthfh,"%f\n", dthdt);
i++;
}
} // End Amplitude Limited Design
sg->spiralDuration = t; // Length of Spiral Part of sequence in s

/* Ramp the gradients down to zero in 45 points at 4us each*/
j = i-1;

```

```

for (n = 0; n<=45; n++){
sg->Gx[i] = sg->Gx[j]*(1-(float)(n)/45.0);
sg->Gy[i] = sg->Gy[j]*(1-(float)(n)/45.0);
fprintf(gxfh,"%f\n",sg->Gx[i]);
fprintf(gyfh,"%f\n",sg->Gy[i]);
i++;
t+= GRADIENT_RES; // Keep track of length of spiral.
}
sg-> rampDuration = (n*GRADIENT_RES);

/* Close Files*/
fclose(gxfh);
fclose(gyfh);
fclose(thfh);
fclose(dthfh);

/* Record length of Spiral */
sg->duration = (t+GRADIENT_RES); //length in seconds, add 4e-6 for the i+1th tick
written for Gx, Gy. This i+1th tick is added to ensure that the last data points on both
gradient waveforms have amplitude zero.

/* Record How many points the total gradient sequence has.*/
sg->numPoints = i+1;

}

/*****

function Name: convertSpToGeneric
Example: convertSpToGeneric(&sg, &genRo, &genPe);
Description: Copies the data points from the Pe and Ro (Y and X) parts of a
spiral gradient structure and puts them into two generic gradient structures. This is
done to make sure that spiral waveforms can play nice with Agilent's gradient kernel
implementations.
Input:
Formal: *sg - pointer to a SPIRAL_GRADIENT_T structure
*genRo - pointer to a GENERIC_GRADIENT_T structure. Ro
direction data goes here
*genPe = pointer to a GENERIC_GRADIENT_T structure. Pe
direcitond data goes here
Output
Return: None
Formal: *sg, *genRo, *genPE. Pointers as mentioned above
*****/

/

void convertSpToGeneric(SPIRAL_GRADIENT_T *sg, GENERIC_GRADIENT_T *genRo,
GENERIC_GRADIENT_T *genPe )
{
/* Declare variables that are necessary*/
int i = 0; // Integer to keep track of loops
double *pRo,*pPe; // pointers for the data points in the spiral structure

/* point the pointers
pRo = sg->Gx;
pPe = sg->Gy;
*/
/* Copy Ro data points over*/
// for(i=0;i<=sg->numPoints; i++) {
genRo->dataPoints = sg->Gx;
// }
genRo->duration = sg->duration;
genRo->amp = sg->amp;
genRo->m0 = sg->GxMoment0;
genRo->numPoints = sg->numPoints;

/* Copy Ro data points over*/
// for(i=0;i<=sg->numPoints; i++) {
genPe->dataPoints = sg->Gy;

```

```

    // }
    genPe->duration = sg->duration;
    genPe->amp = sg->amp;
    genPe->m0 = sg->GyMoment0;
    genPe->numPoints = sg->numPoints;

    //writeToDisk(genPe->dataPoints, genPe->numPoints, genPe->dataPoints[0],
GRADIENT RES, TRUE, "TestGenPe");

}

/*****

function Name:  initSpiral
  Example:      initSpiral(&sg);
  Description:  initializes the structure used to calculate a spiral gradient
using an apporiximation method in Glover (1999) Simple Analytic Spiral K-Space Algorithm.

  Input
    Formal:     *sg - pointer to a spiral gradient structure
    Private:    none
    Public:     GRAD_MAX - maximum possible gradient amplitude

  Output
    Return:     None
    Formal:     *sg - pointer to spiral gradient structure
*****/

void initSpiral (SPIRAL_GRADIENT_T *sg, double gamp, double lro, double Mat, int
Nint )
{
    sg-> type          = GENERIC_GRADIENT_TYPE; // I don't know what this is for
    sg-> amp           = gamp; //Set amplitude to that determined by the user.
    sg-> display       = sgldisplay;
    sg-> fov           = lro; // cm
    sg-> phaseIncrement = 0;
    sg-> numInterleaves = Nint;
    sg-> maxGrad       = GRAD_MAX; // G/cm
    strcpy(sg->nameX, "GX");
    strcpy(sg->nameY, "GY");
    sg-> numPoints     = 0;
    sg-> polarity      = FALSE;
    sg-> resolution    = GRADIENT_RES;
    sg-> rollOut       = ROLL_OUT;
    sg-> slewRate      = 0.9*MAX_SLEW_RATE; // G/cm/s
    sg-> spiralIn      = FALSE;
    sg-> gamma         = nuc gamma();
    sg-> writeToDisk   = TRUE;
    sg-> matrixSize    = Mat;
    sg-> duration      = 0; //seconds
    sg-> rampDuration  = 0; // seconds
    sg-> spiralDuration = 0; // seconds
    sg-> GxMoment0     = 0; // G/cm*s
    sg-> GxMoment1     = 0; //seconds
    sg-> GyMoment0     = 0; // G/cm*s
    sg-> GyMoment1     = 0; //seconds
    sg-> errorX        = FALSE; // Any errors in calculation?
    sg-> errorY        = FALSE; // Any errors in calculation?
}
*****/

/*****

function Name:  reverseToSpiralIn
  Example:      reverseToSpiralIn(&sg);

```

Description: Takes the spiral in trajectory of sg and turns it into a spiral out trajectory. This is done by making  $g(t)$  become  $-g(T_0-t)$ , where  $g$  is the gradient waveform and  $T_0$  is the duration of the spiral waveform. The function also pads the end of the waveform with a couple of zeros to make sure the gradient amplitude ramps down to zero.

```

Input
    Formal: *sg - pointer to a spiral gradient structure
    Private: none
    Public: GRAD MAX - maximum possible gradient amplitude

Output
    Return: None
    Formal: *sg - pointer to spiral gradient structure
*****/

void reverseToSpiralIn(SPIRAL GRADIENT T *sg)
{
    /* Declare variables*/
    int n, i;
    double Gx[sg->numPoints], Gy[sg->numPoints];
    FILE *gxfh, *gyfh, *thfh, *dthfh;

    gxfh = fopen("/home/histo/Spiral/Gx.GRD", "w");
    gyfh = fopen("/home/histo/Spiral/Gy.GRD", "w");
    /* Copy the Gradient waveform into a dummy variable*/
    for (n = 0 ; n<= sg->numPoints ; n++)
    {
        Gx[n] = sg->Gx[n];
        Gy[n] = sg->Gy[n];
    }

    /* Recopy the waveform in again, but backwards and multiplied by negative 1
    Remove one of the zero padded entries at the beginning of the waveform and make
    sure that the last point in the trajectory is zero*/
    i = 0;
    for (n = sg->numPoints-1 ; n>=0 ; n--)
    {
        sg->Gx[i] = -1*Gx[n];
        fprintf(gxfh,"%f\n",sg->Gx[i]);
        sg->Gy[i] = -1*Gy[n];
        fprintf(gyfh,"%f\n",sg->Gy[i]);
        i++;
    }
    sg->Gx[i] = 0;
    sg->Gy[i] = 0;
    fclose(gxfh);
    fclose(gyfh);
}

```

### A2.9.3 KxMap.c

A sequence that can be used to map the gradient trajectory of a spiral along the phase-encode direction.

```

/*
 * Varian, Inc. All Rights Reserved.
 * This software contains proprietary and confidential
 * information of Varian, Inc. and its contributors.
 * Use, disclosure and reproduction is prohibited without
 * prior consent.
 */

/*****
Gradient echo imaging sequence
*****/

#include <standard.h>
#include "histosgl.c"

```

```

pulsesequence()
{
    /* Internal variable declarations *****/
    double freqEx[MAXNSLICE];
    double maxgradtime,perTime,tetime,trtime,te_delay,tr_delay;
    double spoilMoment;
    double Mat, Gamp; //Reconstructed image matrix size and designed gradient
amplitude
    int table,shapeEx;
    int sepSliceRephase=1;
    char spoilflag[MAXSTR],mriout[MAXSTR],slprofile[MAXSTR];
    int listid,i,Nint;
    double int_steps, intPhase, phaseStep;
    char spiral_in[MAXSTR];

    /* Real-time variables used in this sequence *****/
    int vint_steps = v1; // Number of interval steps
    int vms_slices = v3; // Number of slices
    int vms_ctr = v4; // Slice loop counter
    int vone = v7; // variable just to store the value 1.
    int vssc = v8; // Compressed steady-states
    int vacquire = v9; // Argument for setacqvar, to skip steady state
acquires
    int vrfspoil_ctr = v10; // RF spoil counter
    int vrfspoil = v11; // RF spoil multiplier
    int vtrimage = v12; // Counts down from nt, trimage delay when 0
    int vtrigblock = v13; // Number of slices per trigger block
    int vNint = v14; // interval loop counter
    int vsp_amp = v15; // variable to remember sp.amp.

    /* Declare spiral gradients*/
    SPIRAL_GRADIENT_T sp; //Intialize the spiral gradient

    /* Declare rewinder gradients */
    GENERIC_GRADIENT_T sprGx; // Rewinder Gradient for X direction
    GENERIC_GRADIENT_T sprGy; // Rewinder Gradient for Y direction

    /* Initialize paramaters *****/
    sw = getval("sw");
    init_mri();
    getstr("spoilflag",spoilflag);
    getstrnwarn("mriout",mriout);
    getstrnwarn("slprofile",slprofile);
    Nint = getval("Nint");
    Mat = getval("Mat");
    Gamp = getval("Gamp");
    getstr("spiral_in",spiral_in);

    /* Set Rcvr/Xmtr phase increments for RF Spoiling *****/
    /* Ref: Zur, Y., Magn. Res. Med., 21, 251, (1991) ****/
    if (rfspoil[0] == 'y') {
        rcvrstepsize(rfphase);
        obsstepsize(rfphase);
    }

    /* Initialize gradient structures *****/
    init_rf(&pl_rf,plpat,p1,flip1,rof1,rof2 ); // excitation pulse
    init_slice(&ss_grad,"ss",thk); // slice select gradient
    init_slice_refocus(&ssr_grad,"ssr"); // slice refocus gradient
    initSpiral(&sp, Gamp, lro,Mat, Nint); // Spiral Gradient
    initGeneric(&sprGx); // Generic Gradient to rewind the
spirals
    initGeneric(&sprGy); // Generic Gradient to rewind the spirals

    /* RF Calculations *****/
    calc_rf(&pl_rf,"tpwr1","tpwr1f");

    /* Gradient calculations *****/
    if (spiral_in[0] == 'y') {

```

```

        sp.spiralIn = TRUE;
    }
    calcSpiral(&sp);
    calc slice(&ss_grad,&pl_rf,WRITE,"gss");
    calc_slice_refocus(&ssr_grad,&ss_grad,WRITE,"gssr");

    /* Calculate the rewinder gradients*/
    sprGx.calcFlag = DURATION FROM MOMENT AMPLITUDE;
    sprGy.calcFlag = DURATION_FROM_MOMENT_AMPLITUDE;
    sprGx.m0 = sp.GxMoment0;
    sprGy.m0 = sp.GyMoment0;
    sprGx.amp = sp.amp;
    sprGy.amp = sp.amp;
    calcGeneric(&sprGx);
    calcGeneric(&sprGy);
    calc sim gradient(&sprGx, &sprGy, &>null_grad,0,WRITE);
// printf("psi, theta, phi are %f, %f, %f\n", psi, theta, phi);

/* Calculate spectral width and number of points to sample*/
sw = getval("sw");
np = 2*(int)((sp.spiralDuration*sw));
putvalue("npIdeal",np);
nv = 2;
putvalue("nv",nv);          // make sure vnmrj knows how many fid's to expect

/* Check that all Gradient calculations are ok *****/
sql error check(sglerror);

/* Min TE *****/
tetime = ss_grad.rfCenterBack + alfa +ssr_grad.duration;

    temin = tetime + 4e-6; /* ensure that te_delay is at least 4us */
    if (minTE[0] == 'y') {
        te = temin;
        putvalue("te",te);
    }
    if (te < temin) {
        abort_message("TE too short. Minimum TE= %.2fms\n",temin*1000+0.005);
    }
    te_delay = te - tetime;

/* Check nsblock, the number of slices blocked together
   (used for triggering and/or inversion recovery) */
check_nsblock();

/* Min TR *****/
trmin = ss_grad.duration + te_delay + ssr_grad.duration + sp.duration;

/* Adjust for all slices *****/
trmin *= ns;

    if (minTR[0] == 'y') {
        tr = trmin;
        putvalue("tr",tr);
    }
    if (FP_LT(tr,trmin)) {
        abort_message("TR too short. Minimum TR = %.2fms\n",trmin*1000+0.005);
    }

/* Calculate tr delay */
tr_delay = granularity((tr-trmin)/ns,GRADIENT_RES);

/* Set up frequency offset pulse shape list *****/
offsetlist(pss,ss_grad.ssamp,0,freqEx,ns,seqcon[1]);
shapeEx =
shapelist(plpat,ss_grad.rfDuration,freqEx,ns,ss_grad.rfFraction,seqcon[1]);

/* Set int steps for profile or full image *****/
int_steps = nv;

/* Shift DDR for pro *****/

```



```

roff = -poffset(pro,ro_grad.roamp);

/* Adjust experiment time for VnmrJ *****/
if (ssc<0) {
    if (seqcon[2] == 'c') g_setExpTime(trmean*(ntmean*int_steps*arraydim -
ssc*arraydim));
    else g_setExpTime(trmean*(ntmean*int_steps*arraydim -
ssc*int_steps*arraydim));
}
else g_setExpTime(trmean*ntmean*int_steps*arraydim + tr*ssc);

/* PULSE SEQUENCE *****/
status(A);
rotate(); // Initialize default orientation
triggerSelect(trigger); // Select trigger input 1/2/3
obsoffset(resto);
delay(4e-6);
initval(fabs(ssc),vssc); // Compressed steady-state counter
if (seqcon[2]=='s') assign(zero,vssc); // Zero for standard peloop
assign(zero,vrfspoil_ctr); // RF spoil phase counter
assign(zero,vrfspoil); // RF spoil multiplier
assign(one,vacquire); // real-time acquire flag
setacqvar(vacquire); // Turn on acquire when vacquire is zero

/* trigger */
if (ticks > 0) F_initval((double)nsblock,vtrigblock);

/* Begin phase-encode loop *****/
peloop(seqcon[2],int_steps,vint_steps,vNint);

    if (trtype) delay(ns*tr_delay); // relaxation delay

/* Compressed steady-states: 1st array & transient, all arrays if ssc is
negative */
if ((ix > 1) && (ssc > 0))
    assign(zero,vssc);
sub(vNint,vssc,vNint); // vNint counts up from -ssc
assign(zero,vssc);
if (seqcon[2] == 's')
    assign(zero,vacquire); // Always acquire for non-compressed loop
else {
    ifzero(vNint);
    assign(zero,vacquire); // Start acquiring when vNint reaches zero
endif(vNint);
}

/* Set rcvr/xmtr phase for RF spoiling *****/
if (rfspoil[0] == 'y') {
    incr(vrfspoil_ctr); // vrfspoil_ctr = 1 2 3 4 5 6
    add(vrfspoil,vrfspoil_ctr,vrfspoil); // vrfspoil = 1 3 6 10 15 21
    xmtrphase(vrfspoil);
    rcvrphase(vrfspoil);
}

/* Begin multislice loop *****/
msloop(seqcon[1],ns,vms_slices,vms_ctr);

    if (!trtype) delay(tr_delay); // Relaxation delay

    if (ticks > 0) {
        modn(vms_ctr,vtrigblock,vtest);
        ifzero(vtest); // if the beginning of an trigger
        block
            xgate(ticks);
            grad_advance(gpropdelay);
            delay(4e-6);
            elsenz(vtest);
            delay(4e-6);
            endif(vtest);
    }

```

```

}

splon(); delay(4e-6); sploff();          // Scope trigger

/* Slice select RF pulse *****/
obspower(pl_rf.powerCoarse);
obspwrf(pl_rf.powerFine);
delay(4e-6);
obl_shapedgradient(ss_grad.name,ss_grad.duration,0,0,ss_grad.amp,NOWAIT);
delay(ss_grad.rfDelayFront);
shapedpulselist(shapeEx,ss_grad.rfDuration,oph,rof1,rof2,seqcon[1],vms_ctr);
delay(ss_grad.rfDelayBack);

/* refocus gradient *****/
obl_shapedgradient(ssr_grad.name,ssr_grad.duration,0,0,-
ssr_grad.amp,WAIT);

/* rotate the gradient axis */
rot_angle(0,0,0);          // Rotate into the axial frame
delay(te_delay-alfa);      // delay between rf puls and acquisition

/* Set Gradient amplitude to be on for the first transient and off for the
second*/
ifzero(vNint);

/* Some logic control for spiral out or spiral in */
if (sp.spiralIn==TRUE){
obl_shaped3gradient(sprGx.name, "", "", sprGx.duration,sprGx.amp,0,0,WAIT);
delay(4e-6);
}

/* Readout gradient and acquisition *****/
startacq(alfa);
obl_shaped3gradient(sp.nameX,sp.nameY,"",sp.duration,sp.amp,0,0,NOWAIT);
if (spiral_in[0] == 'y') {
delay(granularity(sp.duration-sp.spiralDuration,GRADIENT_RES));
}
acquire(np,1.0/sw);
endacq();
delay(granularity(sp.duration-sp.spiralDuration, GRADIENT_RES)); // Delay
length of ramp down.
delay(20e-6); //For some reason this delay has to be here. I don't get it.

/* Some logic control for spiral our or spiral in */
if (sp.spiralIn==FALSE){
obl_shaped3gradient(sprGx.name, "", "", sprGy.duration,-sprGx.amp,0,0,WAIT);
delay(4e-6);
}

elsenz(vNint);
if (sp.spiralIn==TRUE){
obl_shaped3gradient(sprGx.name,"","",sprGx.duration,0,0,0,WAIT);
delay(4e-6);
}

/* Readout gradient and acquisition *****/
startacq(alfa);
obl_shaped3gradient(sp.nameX,sp.nameY,"",sp.duration,0,0,0,NOWAIT);
if (spiral_in[0] == 'y') {
delay(granularity(sp.duration-sp.spiralDuration,GRADIENT_RES));
}
acquire(np,1.0/sw);
endacq();
delay(granularity(sp.duration-sp.spiralDuration,GRADIENT RES)); // Delay
length of ramp down.
delay (20e-6);

/* Some logic control for spiral out or spiral in */
if (sp.spiralIn==FALSE){
obl_shaped3gradient(sprGx.name, "", "", sprGx.duration,0,0,0,WAIT);
delay(4e-6);
}

```

```

    }

endif(vNint);

/* Rotate back into the default reference frame*/
rotate();

endmsloop(seqcon[1],vms_ctr);

/* Optional output control examples *****/
if (mriout[0]=='b' || mriout[1]=='b')
    writeMRIUserByte(vNint);
if (mriout[0]=='g' || mriout[1]=='g')
    setMRIUserGates(vNint);

endpeloop(seqcon[2],vNint);

/* Inter-image delay *****/
sub(ntrt,ct,vtrimage);
decr(vtrimage);
ifzero(vtrimage);
    delay(trimage);
endif(vtrimage);

calc_grad_duty(tr);
}

```

## A2.9.4 KyMap.c

A sequence that can be used to map the gradient trajectory of a spiral along the frequency-encode direction.

```

/*
 * Varian, Inc. All Rights Reserved.
 * This software contains proprietary and confidential
 * information of Varian, Inc. and its contributors.
 * Use, disclosure and reproduction is prohibited without
 * prior consent.
 */

/*****
Gradient echo imaging sequence
*****/

#include <standard.h>
#include "histosgl.c"

pulsesequence()
{
    /* Internal variable declarations *****/
    double freqEx[MAXNSLICE];
    double maxgradtime,perTime,tetime,trtime,te_delay,tr_delay;
    double spoilMoment;
    double Mat, Gamp; //Reconstructed image matrix size and designed gradient
amplitude
    int table,shapeEx;
    int sepSliceRephase=1;
    char spoilflag[MAXSTR],mriout [MAXSTR],slprofile[MAXSTR];
    int listid,i,Nint;
    double int_steps, intPhase, phaseStep;
    char spiral_in[MAXSTR];

    /* Real-time variables used in this sequence *****/
    int vint_steps = v1; // Number of interval steps
    int vms_slices = v3; // Number of slices
    int vms_ctr = v4; // Slice loop counter

```

```

int vone          = v7;          // variable just to store the value 1.
int vssc          = v8;          // Compressed steady-states
int vacquire      = v9;          // Argument for setacqvar, to skip steady state
acquires
int vrfspoil_ctr = v10;         // RF spoil counter
int vrfspoil     = v11;         // RF spoil multiplier
int vtrimage     = v12;         // Counts down from nt, trimage delay when 0
int vtrigblock   = v13;         // Number of slices per trigger block
int vNint        = v14;         // interval loop counter
int vsp_amp      = v15;         // variable to remember sp.amp.

/* Declare spiral gradients*/
SPIRAL_GRADIENT_T sp;          //Initialize the spiral gradient

/* Declare rewinder gradients */
GENERIC_GRADIENT_T sprGx;     // Rewinder Gradient for X direction
GENERIC_GRADIENT_T sprGy;     // Rewinder Gradient for Y direction

/* Initialize paramaters *****/
sw = getval("sw");
init_mri();
getstr("spoilflag",spoilflag);
getstrnwarn("mriout",mriout);
getstrnwarn("slprofile",slprofile);
Nint = getval("Nint");
Mat = getval("Mat");
Gamp = getval("Gamp");
getstr("spiral_in",spiral_in);

/* Set Rcvr/Xmtr phase increments for RF Spoiling *****/
/* Ref: Zur, Y., Magn. Res. Med., 21, 251, (1991) *****/
if (rfspoil[0] == 'y') {
    rcvrstepsize(rfphase);
    obsstepsize(rfphase);
}

/* Initialize gradient structures *****/
init_rf(&pl_rf,plpat,pl,flip1,rof1,rof2 ); // excitation pulse
init_slice(&ss_grad,"ss",thk);           // slice select gradient
init_slice_refocus(&ssr_grad,"ssr");      // slice refocus gradient
initSpiral(&sp, Gamp, lro,Mat, Nint);     // Spiral Gradient
initGeneric(&sprGx);                       // Generic Gradient to rewind the
spirals
initGeneric(&sprGy);                       // Generic Gradient to rewind the spirals

/* RF Calculations *****/
calc_rf(&pl_rf,"tpwrl","tpwrlf");

/* Gradient calculations *****/
if (spiral_in[0] == 'y') {
    sp.spiralIn = TRUE;
}
calcSpiral(&sp);
calc_slice(&ss_grad,&pl_rf,WRITE,"gss");
calc_slice_refocus(&ssr_grad,&ss_grad,WRITE,"gssr");

/* Calculate the rewinder gradients*/
sprGx.calcFlag = DURATION FROM MOMENT AMPLITUDE;
sprGy.calcFlag = DURATION FROM MOMENT AMPLITUDE;
sprGx.m0 = sp.GxMoment0;
sprGy.m0 = sp.GyMoment0;
sprGx.amp = sp.amp;
sprGy.amp = sp.amp;
calcGeneric(&sprGx);
calcGeneric(&sprGy);
calc_sim_gradient(&sprGx, &sprGy, &>null_grad,0,WRITE);

/* Calculate spectral width and number of points to sample*/
sw = getval("sw");
np = 2*(int)((sp.spiralDuration*sw));
putvalue("npIdeal",np);

```

```

nv = 2;
putvalue("nv",nv);          // make sure vnmrj knows how many fid's to expect

/* Check that all Gradient calculations are ok *****/
sgl_error_check(sglerror);

/* Min TE *****/
tetime = ss grad.rfCenterBack + alfa +ssr grad.duration;

    temin = tetime + 4e-6; /* ensure that te delay is at least 4us */
    if (minte[0] == 'y') {
        te = temin;
        putvalue("te",te);
    }
    if (te < temin) {
        abort message("TE too short.  Minimum TE= %.2fms\n",temin*1000+0.005);
    }
    te_delay = te - tetime;

/* Check nsblock, the number of slices blocked together
   (used for triggering and/or inversion recovery) */
check nsblock();

/* Min TR *****/
trmin = ss grad.duration + te delay + ssr grad.duration + sp.duration;

/* Adjust for all slices *****/
trmin *= ns;

if (mintr[0] == 'y') {
    tr = trmin;
    putvalue("tr",tr);
}
if (FP_LT(tr,trmin)) {
    abort_message("TR too short.  Minimum TR = %.2fms\n",trmin*1000+0.005);
}

/* Calculate tr delay */
tr delay = granularity((tr-trmin)/ns,GRADIENT RES);

/* Set up frequency offset pulse shape list *****/
offsetlist(pss,ss_grad.ssamp,0,freqEx,ns,seqcon[1]);
shapeEx =
shapelist(plpat,ss_grad.rfDuration,freqEx,ns,ss_grad.rfFraction,seqcon[1]);

/* Set int_steps for profile or full image *****/
int_steps = nv;

/* Shift DDR for pro *****/
roff = -poffset(pro,ro grad.roamp);

/* Adjust experiment time for VnmrJ *****/
if (ssc<0) {
    if (seqcon[2] == 'c') g_setExpTime(trmean*(ntmean*int_steps*arraydim -
ssc*arraydim));
    else g_setExpTime(trmean*(ntmean*int_steps*arraydim -
ssc*int_steps*arraydim));
}
else g_setExpTime(trmean*ntmean*int_steps*arraydim + tr*ssc);

/* PULSE SEQUENCE *****/
status(A);
rotate(); // Initialize default orientation
triggerSelect(trigger); // Select trigger input 1/2/3
obsoffset(resto);
delay(4e-6);
initval(fabs(ssc),vssc); // Compressed steady-state counter
if (seqcon[2]=='s') assign(zero,vssc); // Zero for standard peloop
assign(zero,vrfspoil_ctr); // RF spoil phase counter
assign(zero,vrfspoil); // RF spoil multiplier
assign(one,vacquire); // real-time acquire flag

```

```

        setacqvar(vacquire);                // Turn on acquire when vacquire is zero

/* trigger */
if (ticks > 0) F initval((double)nsblock,vtrigblock);

/* Begin phase-encode loop *****/
peloop(seqcon[2],int_steps,vint_steps,vNint);

        if (trtype) delay(ns*tr delay); // relaxation delay

/* Compressed steady-states: 1st array & transient, all arrays if ssc is
negative */
if ((ix > 1) && (ssc > 0))
    assign(zero,vssc);
sub(vNint,vssc,vNint); // vNint counts up from -ssc
assign(zero,vssc);
if (seqcon[2] == 's')
    assign(zero,vacquire); // Always acquire for non-compressed loop
else {
    ifzero(vNint);
    assign(zero,vacquire); // Start acquiring when vNint reaches zero
    endif(vNint);
}

/* Set rcvr/xmtr phase for RF spoiling *****/
if (rfspoil[0] == 'y') {
    incr(vrfspoil_ctr); // vrfspoil_ctr = 1 2 3 4 5 6
    add(vrfspoil,vrfspoil_ctr,vrfspoil); // vrfspoil = 1 3 6 10 15 21
    xmtrphase(vrfspoil);
    rcvrphase(vrfspoil);
}

/* Begin multislice loop *****/
msloop(seqcon[1],ns,vms_slices,vms_ctr);

        if (!trtype) delay(tr_delay); // Relaxation delay

        if (ticks > 0) {
            modn(vms_ctr,vtrigblock,vtest);
            ifzero(vtest); // if the beginning of an trigger
                xgate(ticks);
                grad advance(gpropdelay);
                delay(4e-6);
                elsenz(vtest);
                delay(4e-6);
                endif(vtest);
        }

        splon(); delay(4e-6); sploff(); // Scope trigger

/* Slice select RF pulse *****/
obspower(pl_rf.powerCoarse);
obspwrf(pl_rf.powerFine);
delay(4e-6);
obl shapedgradient(ss grad.name,ss grad.duration,0,0,ss grad.amp,NOWAIT);
delay(ss_grad.rfDelayFront);
shapedpulselist(shapeEx,ss_grad.rfDuration,oph,rof1,rof2,seqcon[1],vms_ctr);
delay(ss_grad.rfDelayBack);

/* refocus gradient *****/
obl shapedgradient(ssr grad.name,ssr grad.duration,0,0,-
ssr_grad.amp,WAIT);

/* rotate the gradient axis */
rot angle(0,0,0); // Rotate into the axial frame
delay(te_delay-alfa); // delay between rf puls and acquisition

```

```

second*/
        /* Set Gradient amplitude to be on for the first transient and off for the
ifzero(vNint);

        /* Some logic control for spiral out or spiral in */
if (sp.spiralIn==TRUE){
    obl_shaped3gradient( "",sprGy.name,"", sprGx.duration,0,sprGy.amp,0,WAIT);
    delay(4e-6);
    }

        /* Readout gradient and acquisition *****/
startacq(alfa);
obl_shaped3gradient(sp.nameX,sp.nameY,"", sp.duration,0,sp.amp,0,NOWAIT);
if (spiral_in[0] == 'y') {
    delay(granularity(sp.duration-sp.spiralDuration,GRADIEN_T_RES));
    }
acquire(np,1.0/sw);
endacq();
length of ramp down.
delay(20e-6); //For some reason this delay has to be here. I don't get it.

        /* Some logic control for spiral our or spiral in */
if (sp.spiralIn==FALSE){
    obl_shaped3gradient( "",sprGy.name,"", sprGy.duration,0,-sprGy.amp,0,WAIT);
    delay(4e-6);
    }

elseif(vNint);
if (sp.spiralIn==TRUE){
    obl_shaped3gradient("",sprGy.name, "",sprGy.duration,0,0,0,WAIT);
    delay(4e-6);
    }

        /* Readout gradient and acquisition *****/
startacq(alfa);
obl_shaped3gradient(sp.nameX,sp.nameY,"", sp.duration,0,0,0,NOWAIT);
if (spiral_in[0] == 'y') {
    delay(granularity(sp.duration-sp.spiralDuration,GRADIEN_T_RES));
    }
acquire(np,1.0/sw);
endacq();
length of ramp down.
delay (20e-6);

        /* Some logic control for spiral out or spiral in */
if (sp.spiralIn==FALSE){
    obl_shaped3gradient("",sprGy.name,"", sprGy.duration,0,0,0,WAIT);
    delay(4e-6);
    }

endif(vNint);

        /* Rotate back into the default reference frame*/
rotate();

endmsloop(seqcon[1],vms_ctr);

        /* Optional output control examples *****/
if (mriout[0]=='b' || mriout[1]=='b')
    writeMRIUserByte(vNint);
if (mriout[0]=='g' || mriout[1]=='g')
    setMRIUserGates(vNint);

endpeloop(seqcon[2],vNint);

        /* Inter-image delay *****/
sub(ntrt,ct,vtrimage);
decr(vtrimage);

```

```
ifzero(vtrimage);  
    delay(trimage);  
endif(vtrimage);  
  
calc_grad_duty(tr);  
}
```